UNIVERSITÉ DE STRASBOURG

ÉCOLE DOCTORALE 269 : Mathématiques, Sciences de l'Information et de l'Ingénieur (MSII)

Laboratoire des Sciences de l'Ingénieur, de l'Informatique et de l'Imagerie (ICube UMR7357)

THÈSE présentée par :

Tony HAJJ

soutenue le : **22 Septembre 2023**

pour obtenir le grade de : **Docteur de l'université de Strasbourg**

Discipline/ Spécialité : Photonics / Photonique

High curvature micro-lenses for advanced optical fiber applications

Micro-lentilles à forte courbure pour des applications de fibres optiques avancées

THÈSE dirigée par :

Pr. LECLER Sylvain	Professeur, INSA Strasbourg
Dr. CHABROL Grégoire	Maître de conférences, HDR, Icam Strasbourg, ICube

RAPPORTEURS :

Dr. GROSJEAN Thierry	CNRS, Femto-ST
Pr. BOUWMANS Géraud	Professeur, Université de Lille

AUTRES MEMBRES DU JURY :

Pr. THUAL Monique	Professeur, Université de Rennes
Dr. Assia Guessoum	Maître de conférences, HDR, Université de Sétif 1

MEMBRE INVITÉ :

Pr. Nacer-E. Demagh	Professeur, Université de Sétif 1

Acknowledgements

I would like to express my deepest gratitude to my supervisor, Sylvain Lecler, not only for his guidance and support but also for instilling in me a genuine passion for the fields of optical fibers, high power lasers, electromagnetism and diffractive optical elements. I am also deeply grateful for trusting in my abilities, and granting me the freedom to think independently and be creative throughout my research journey. His dedication and hard work, along with his constant efforts to foster collaborations, have added immense value to my PhD experience. I am profoundly thankful for the collaborations that were made possible through his network, as they not only made my research more interesting but also allowed me to broaden my areas of expertise. Furthermore, I deeply appreciate his recommendations and kind words, which have greatly supported me in my pursuit of post-PhD career opportunities.

I would also like to extend special thanks to my co-supervisor, Grégoire Chabrol, for his unwavering support and valuable insights in publications and presentations. His contributions have been instrumental in shaping the quality and impact of my research work.

Additionally, I am indebted to Pierre Pfeiffer for his extensive knowledge in the field of optical fibers. I am grateful for the enlightening discussions we had regarding his vast professional experience and the multitude of projects he has undertaken. Moreover, I am truly grateful to Pierre Pfeiffer for granting me access to his laboratory equipment, which played a vital role in facilitating my experimental work.

I would like to extend my heartfelt appreciation to Jesse Schiffler and Stéphane Roques for their unwavering assistance during my experiments and measurements. Jesse's invaluable support in developing the mechanical components for my optical setup, as well as his expertise in setting up LabView for device communication and connection, have been instrumental to my research. Similarly, Stéphane's expertise in chemistry has been of immense value, without which the fabrication of fiber micro-lenses would not have been possible. I am also grateful to Jeremy Bartringer for teaching me how to operate the Raman Spectroscope and for his SEM and FT-IR measurements.

I would like to express my gratitude to our collaborators, Professor Nasser-Demagh Ezzedin from the University of Setif - Algeria. His valuable advice has been crucial during the initial stages of the development of the micro-lens fabrication setup. I would also like to thank Professor Laurent Bigot from Lille University - France for providing us with the multi-core fibers and for assisting with their characterization after equipping them with micro-lenses.

I am sincerely grateful to Thierry Grosjean, Géraud Bouwmans, Monique Thual, and Assia Guessoum for agreeing to be the members of the thesis jury.

I would be remiss not to acknowledge the enriching discussions I had with my colleagues and friends, Sébastien Marbach, Stephane Perrin, and Amir Nahass. Their insights into microscopy, along with their expertise in designing and constructing advanced optical setups, have contributed significantly to my academic and personal growth.

I would like to express my heartfelt gratitude to all the individuals I have mentioned, as well as to other friends, namely Djamila Bouaziz, Rayenne Boudoukha, Hishem Hyani, Alireza Morsali, Hugo Maurey, Baptist Deazevedo, Farid Mahfoud, and Noémie Gambaudo. Your friendship and support have made the past three years truly worthwhile. I cherish every moment spent with all of you, and I am grateful for the amazing friends you have been throughout my journey.

Finally, I deeply and sincerely want to express my gratitude above all to my family, who have been, are, and will always be an unwavering source of support and my greatest strength. I would also like to extend my heartfelt thanks to my girlfriend, whose love and encouragement have been a constant source of inspiration and happiness in my life.

Thank you all for your unwavering support, guidance, and companionship.

Contents

General Introduction **1**

1 Optical Fiber micro-Lenses: fabrication techniques and Applications **4**
1.1 Working principle of a fiber micro-lens 4
1.1.1 Light collection and coupling 4
1.1.1.1 Numerical aperture 4
1.1.2 Beam focusing 9
1.1.2.1 Photonic nano-jet 9
1.1.2.2 Analytical (modal) methods 11
1.1.2.3 Numerical methods 12
1.1.2.4 Experimental characterization 13
1.2 Fabrication Techniques for single-core fibers 15
1.2.1 Refractive micro-lenses 16
1.2.1.1 Photopolymerization and photolithography 16
1.2.1.2 Thermal melting 20
1.2.1.3 Electric arc discharge 20
1.2.1.4 CO2 laser melting 24
1.2.1.5 Chemical etching 24
1.2.1.6 Grinding 26
1.2.1.7 Electrostatic pulling 26
1.2.1.8 Other less-implemented noteworthy techniques . . . 27
1.2.2 Diffractive micro-lenses 27
1.2.3 Resonant micro-lenses 29
1.3 Fabrication techniques for Hollow-Core fibers 30
1.3.1 Splicing of solid core fiber and shaping by electric a rc discharge 31
1.3.2 Micro-sphere insertion in hollow-core 32
1.4 Lens fabrication techniques for multi-core fibers 32
1.4.1 Two Photon Lithography/ 3D printing 33
1.4.2 Photopolymerization 33
1.5 Conclusion 35

2 Molded polymer fabrication technique **37**
2.1 On Single-core fibers 37
2.1.1 Mold fabrication and lens shape control 38
2.1.1.1 Controlling the mold depth/lens height 38
2.1.1.2 Controlling mold diameter/lens base 40
2.1.2 Polymer preparation 42

2.1.3 Micro-lens deposition . . . 42
2.1.4 Spacer fabrication . . . 45
2.1.5 Micro-lens quality . . . 46
2.1.5.1 Surface roughness and geometry . . . 46
2.1.5.2 Durability, thermal cycling test . . . 48
2.2 On hollow core and photonic crystal fibers . . . 49
2.3 On multi-core fibers . . . 50
2.3.1 Challenge 1: Mold cavity dimension control . . . 50
2.3.2 Challenge 2: Mold polymer filling . . . 50
2.3.3 Challenge 3: Core Alignment . . . 51
2.4 Conclusion . . . 54

3 Micro-lens modeling and characterization 56
3.1 Numerical study of the micro-lens design . . . 56
3.1.1 Lens Design . . . 56
3.1.1.1 Bézier weight . . . 58
3.1.1.2 Base diameter and height . . . 59
3.1.1.3 Spacer . . . 59
3.1.2 Reflection losses and coating . . . 59
3.1.3 Effect of micro-lens misalignment . . . 61
3.2 Experimental characterization . . . 63
3.2.1 Single-core fiber . . . 63
3.2.2 Multi-core fiber . . . 64
3.2.2.1 Injection in each core individually . . . 64
3.2.2.2 Multi-Core dynamic excitation by beam shaping . . . 65
3.2.2.3 Characterization results of an array of micro-lenses for a 4-core fiber . . . 66
3.2.2.4 Characterization results of an array of micro-lenses for a 37-core fiber . . . 67
3.3 Conclusion . . . 70

4 Applications 73
4.1 Mid-IR laser diode coupling in fluoride fibers . . . 73
4.1.1 Non-silica based fibers - fluoride fibers . . . 74
4.1.2 PDMS and NOA61 transmittance . . . 75
4.1.3 Diode-fiber coupling system description and simulation . . . 75
4.1.4 Fabricated micro-lenses and experimental results . . . 77
4.2 Micro-lens power tolerance and laser micro-processing . . . 79
4.2.1 Thermal simulation study . . . 80
4.2.2 Experimental threshold determination . . . 83
4.2.3 Silicon etching . . . 87
4.3 Conclusion . . . 89

General Conclusion and perspectives 90

A Coating effect on intensity inside the micro-lens 96

B Mid-IR diode laser in non-silica fluoride fiber coupling Zemax simulations 97

References i

Publications and Communications xviii

Abstract - Résumé xx

List of Figures

1.1 a) Representation of curved fiber end with radius r. b) Spherical fiber end half-acceptance-angle as a function of a/r. The considered indexes are those of a typical step index Single-mode (SM) fiber: $n_1 = 1.4522$ and $n_2 = 1.4514$. 6

1.2 Radius of curvature of a parabolic curve. [20] 6

1.3 2D representation electric field amplitude profiles for all the guided modes of a fiber with step index profile. The two colors indicate different signs of electric field values. [21] 7

1.4 Gaussian beam propagation through fiber micro-lens. [23] 8

1.5 (a) Illustration of a photonic jet and its characteristic parameters. (b) 2D Photonic jet power density generated by a cylinder of diameter D = 24 µm and index $n_p = 1.5$, irradiated by an unitary plane wave . . 10

1.6 (a) Simulation of the intensity distribution generated by Multi-mode (MM) fiber with 100 µm core diameter. The fiber base diameter and tip length are 100 and 63 µm, respectively. The refractive indices of core and cladding are of 1.46 and 1.44, respectively. The wavelength is 633 nm and only the fundamental mode is excited. (b) Optical microscope view of a shaped fiber tip. [46] 11

1.7 Imaging system for beam characterization: illustration and photo. OF, optical fiber; MO, microscope objective; RL, relay lens; C, camera. Black-dashed-line box represents a close-up view of the focused beam through the shaped fiber tip. 15

1.8 Beam radius and intensity as a function of fibers tip-to-tip separation in water. Inset 1: 2D Intensity map at beam waist for 808 nm light. Tip-to-tip distance is 24.69 µm. Inset 2: Shaped fiber tip acting as source and tapered fiber probe with a separation of 61 µm as seen by a lateral magnifying optical system. [64] 15

1.9 Three categories of micro-lenses. Diffractive and resonant lenses are also referred to as flat lenses. [65] 16

1.10 High efficiency diode laser-fiber coupling in a stable and compact packaging. [66] 16

1.11 a) Generation of a self-aligned hemi-spherical micro-lens by photpolymerzation. c) Generation of a cylindrical micro-lens by photolithography. b) and d): Scanning electron microscope image of the fabricated micro-lens by the procedures depicted in a) and c), respectively [59]. . 17

1.12 (a) Formed polymer tip over the core of a SM fiber (image dimension: 150 by 118 µm). (b) 0.6 µm radius of curvature tip cured for 2 s. (c) 2.5 µm radius of curvature tip cured for 45 s [67]. (d) LP_{21} mode injected into the fiber and the resulting polymer fiber tip [68]. 18

1.13 (a) A thin layer of UV epoxy corresponding to the final micro-lens height is deposited on the fiber end. (b) The epoxy covering the fiber core is exposed to UV light emerging from a tapered fiber after careful alignment. (c) Unexposed polymer is removed using an air knife. (d) Final UV exposure for complete curing. (e) Resulting micro-lens on SM end [71]. 19

1.14 Fiber (a) High Numerical aperture (NA) lens (b) Beam expander (c) Multi-lens beam expander (All scale bars represent 20 µm) (d) SU8 polymer plano-convex and plano-concave lens combination (radii of curvature are 29.5 and -23.1 µm, respectively). All fabricated by two photon polymerization [73]. 19

1.15 spherical fiber ends formed by thermal melting. Each fiber has a 100 µm diameter, and the end has a 50 µm radius of curvature (a), 75 µm (b), and 125 µm (c) [19] 20

1.16 (a) Arcing setup used to deposit a silica micro-lens on SM fiber core. (b) Scanning electron photomicrograph of micro-lens with 17 µm radius. (c) and (d) Photographs of silica micro-lenses on 190 µm outer diameter fiber. The radius of each is 8.5 and 17.5 µm, respectively. . . 21

1.17 Coreless fiber spliced to a SM fiber. Beam is expanded before focusing to get smaller focused beams[81]. 22

1.18 (a) Spot size and Working distance (WD) as a function of the coreless fiber length. (b) Focus spot characterization of the hemi-spherical vs hyperbolic lenses; hemi-spherical lens suffers from spherical aberrations. (c) Fabrication procedure of hyperbolic micro-lens [81]. 22

1.19 (a) GRIN lens splicing configuration and beam spot size evolution. (b) Distribution of borosilicate rods to create a graded index: NC42 (n=1.56895) and NC34 (n=1.56078). GRIN lens index profile: (c) ideal (theoretical), (d) experimental, and (e) ideal (theoretical) vs experimental [84]. 23

1.20 (a) CO_2 micromachining fabrication setup [85]. (b) and (c) Photographs of asymmetric hyperbolic micro-lenses [78, 79]. 24

1.21 Scanning electron photomicrograph of the first SM fiber micro-lens created by chemical etching [87]. 25

1.22 (a) Schematic representation of the transformation stages of the end of a silica optical fibre dipped in Hydrofluoric acid (HF) acid. (b) Etching process interrupted before final stage at the desired diameter. Fiber is then cleaved and its tip is melted by electric arc. (c) Resulting fiber tip from process in (b). (d) Electric arc applied on a fiber after the final stage of HF etching [91]. 25

1.23 Fiber tip grinder scheme and a resulting elliptic-cone-shaped fiber tip [93]. 26

1.24 (A) Before and (B) after electrostatic pulling of a SU-8 micro-lens [95]. 27

1.25 (a) Scanning electron microscope of a micro-bead attached to etched fiber core. (b) and (c) are the shape of an NOA61 droplet on the end-face of a fiber with and without hydrophobic treatment, respectively [96, 97]. 27
1.26 (a) Mold used for the fabrication of the diffractive lens shown in (b) by NIL. (c) Fresnel lens on SM fiber core. (d) Fresnel zone plate realized by ion beam milling. (e) Fresnel lens (f) Comsol simulation of light focusing through the Fresnel lens shown in (c). (g) and (h) Schematic representation of the working principle of a Fresnel zone plate and its response to different wavelengths [98, 99]. 28
1.27 (a) Photonic crystal few mode optical fiber with 40 nm gold layer where metalens is inscrivbed by FIB. (b) and (c) show the schematic of the meta-lens design. (d) and (e) are SEM images of fabricated meta-lenses designed to obtain focal lengths of 30 µm and 50 µm with NAs of 0.37 and 0.23, respectively, at an operating wavelength of 1550 nm. (f) and (g) are SEM images at different scales of a meta-lens that serves as vortex beam generator for a SM fiber with beam expander/spacer; Resulting vortex beam is shown in (i). (h) beam collimation achieved using a meta-lens inscribed on SM fiber spacer [13, 108]. 30
1.28 (a) silica micro-bead inserted in hollow-core fiber tip (b) and (c) show the difference in beam diameter before and after inserting the micro-bead, respectively [114]. (d) Image of a Hollow-core fiber (HCF) inner structure (e) Capping the fiber with a MM fiber to block the holes and make it possible to use the fiber in immersion applications. (f) Fiber tip curved by electric arcing [115]. 31
1.29 (a) Micro-prisms completely covering the cores, fabricated by two photon lithography. (b) Three dimensional trapping of a red blood cell. [133] 33
1.30 Multi-core fiber (MCF) lenses. (a) 120 micro-lens acting as beam collimator. (b) The fully printed fiber tip. (c) Achieved lateral beam scanning. [136] 34
1.31 Illustration of photopolymerization procedure of MCF micro-lenses and scanning electron image of the resulting MCF tip. [137] 34
1.32 Comparison between refractive, diffractive and resonant micro-lenses[65] 36

2.1 Index profile of a MM graded-index fiber doped with (left) germanium, (right) Fluorine. [145] 38
2.2 Conic molds etched in (a) 50/125 MM, (b)(c) SMF28 and SMF450 [148] step index fibers. 39
2.3 Scheme of fiber HF etching setup. Beaker is made of Teflon and the fiber support has a Teflon protective layer. 39
2.4 Mold depth evolution as a function of chemical etching time. Etching rates are: NMF = 0.37 µm/min ; GIF50C = 0.83 µm/min ; Phlam = 1.87 µm/min ; GIF625 = 20.3 µm/min. 40
2.5 Schematic view of the mold in the fiber core after HF etching. 41
2.6 (a) Fiber melting and drawing setup. (b) 1.80 ± 0.05 mm stretched 50/125 slica fiber. 41

2.7 Schematic of the micro-lens fabrication setup. Fiber 1 is to be equipped with the lens, Fiber 2 holds the mold, and Fiber 3 brings the polymer droplets. Two CCD cameras are used for alignment monitoring. . . . 43
2.8 (a) Fiber 3 with polymer droplets to fill the mold. Top views: Photos of the mold before and after polymer filling by the droplets on fiber 3. (b) and (c) Fiber and mold alignment: pre and post contact. (d) Mold release. Micro-lens successfully deposited on Fiber 1. 44
2.9 (a) Distance between fibers and the 200°C heating source (a soldering iron in our case) for Polydimethylsiloxane (PDMS) micro-lens pre-curing. (b) PDMS pre-curing time as a function of mold etching time for a 50/125 GIF50C un-tapered fiber. Blue and orange curves represent pre-curing times obtained at 21 and 26°C room temperatures. 44
2.10 (a) and (b): High curvature PDMS micro-lenses with around 60 µm base fabricated on two 50/125 MM fibers; (c) and (d) two micro-lenses with around 15 µm base on SMF-28. 45
2.11 (a) Fiber ends separation leading to a 100 µm spacer. (b) Micro-lens deposited on the fabricated spacer. (c) 252 µm spacer made by performing the fabrication procedure twice; in addition to a micro-lens. 46
2.12 Interferometer profilometry measurement of a mold etched in a 50 µm core graded index optical fiber. Information on surface roughness and radius of curvature cannot be deduced. 47
2.13 (a) and (c) are the microscope images of the molds in a nine-mode and mutli-mode fibers, respectively. (b) and (d) are their respective profiles taken along their height cross sections [146]. 47
2.14 SEM image of a Norland Optical Adhesive 61 (NOA61) micro-lens; The lens show a very low surface roughness, and almost no imperfections in its geometry. The ring at the fiber edge is due to the overflow of polymer during the fabrication process. 48
2.15 (a) Temperature evolution during thermal cycling test. (b)(b') and (c)(c') are images of two micro-lenses before and after the thermal cycling test. No deformation or debonding occurred. 48
2.16 (a) On the right, a HCF equipped with one of our NOA61 micro-lenses. The mold etched in HF for 25 minutes is on the left. (b) Structure of a HCF similar to the one employed. The shown HCF has a 15 µm core diameter, while the one we used (HC-1060 from Thorlabs) have a 20 µm core diameter. (c) Anti-resonant HCF equipped with an NOA61 micro-lens. Its mold is etched for 40 minutes. (d) Facet of the employed anti-resonant HCF [130]. 49
2.17 Attempt to fill a 37-core-fiber mold with NOA61. Air bubbles remain trapped underneath the polymer even after 15 minutes. 51
2.18 PDMS filling 37-core-fiber mold while purging air out of the structure in around 30 seconds. 51
2.19 Schematic illustration of micro-lens fabrication setup adapted for MCF. 52
2.20 (a) Image of two MCF facets with matching orientation seen on ShinhoAmerica splicing device shown in (c). (b) Illustration of imaging technique that allows the visualization of fiber facets thanks to a Prism. 53

2.21 PDMS micro-lens array deposited on 4 and 37 cores fibers using: (a) a 4 step index cores fiber etched during 25 minutes (b) a 4 graded index core fiber etched during 10 minutes (c) a 37 graded index cores fiber etched during 10 minutes. The used HF concentration is 24%. The MCFs come from the Phlam laboratory. 53

3.1 Lens base and height are 30 and 25 µm, respectively, and 3 Bézier weights Bézier weight (W): 0.3, 0.6, 1.1. 58

3.2 Beam intensity distribution in space upon interacting with a PDMS micro-lens with a Bézier weight going from 0.1 to 1. Lens base and height are 20 and 15 µm. SMF28 in 2D. Fundamental mode at 1550 nm. 58

3.3 WD and Full width at half maximum (FWHM) evolution of the emerging beam as function of the Bézier weight describing the micro-lens. PDMS Lens base and height are 20 and 15 µm on a SMF28 in 2D. Fundamental mode at 1550 nm. 59

3.4 Intensity distribution simulation with a NOA61 micro-lens with a base diameter, height and W of 25 µm, 18 µm, and 0.47 respectively. The obtained FWHM is 1 µm and the WD is 6 µm. SMF28 in 2D. Fundamental mode at 1070 nm. 60

3.5 Intensity distribution simulation of the SMF28 fiber fundamental mode at 1070 nm interacting with (a) a NOA61 micro-lens with a base diameter, height and Bézier weigh of 50 µm, 31 µm and 0.5, respectively (WD = 21 µm); (b) the same micro-lens but on a 200 µm long NOA61 spacer (WD = 22.5 µm). A more tightly focused beam is obtained 60

3.6 Evaluation of the transmitted, back-scattered, and laterally deflected power as function of the Bézier weight of an (a) uncoated and an (b) AR coated micro-lens. A noticeable 5% improvement is obtained with AR. Lens base and height are 20 and 15 µm. SMF28 in 2D. Fundamental mode at 1070 nm. 61

3.7 Intensity distribution simulation. The direction of propagation is from right to left: a 5 µm diameter Gaussian beam (1070 nm wavelength) from the right coupled into a SMF28 fiber with a PDMS micro-lens (height and base of 15 µm, W= 0.4). This does not represent a good coupling configuration. 62

3.8 (a - d) Intensity distribution simulation at different micro-lens position with respect to an SMF28 core axis. (e) Beam deflection and FWHM as function of the micro-lens's shift. PDMS micro-lens (height of 14 µm, base of 30 µm, W= 0.47). Fundamental mode at 1070 nm. 62

3.9 (a) SMF-28 with NOA61 micro-lens; base diameter, height and W are 25 µm, 18 µm, and 0.47, respectively. (b) Intensity measurement of the beam at the waist for the fundamental mode at 1070 nm. (c) Plot profile of beam waist cross-section. 63

3.10 (a) SMF-28 with NOA61 micro-lens; base diameter, height and W are 47 µm, 14 µm, and 0.42 respectively. (b) 2D simulation of the fundamental mode at ($\lambda = 1070\ nm$) (c) experimental measurement of the evolution of the FWHM along the optical axis (0 on the x-axis represents the position of the beam waist). 64
3.11 Schematic representation of MCF characterization setup of the Phlam lab with light injected in each core individually using: (a) a SMF28; (b) a focused laser beam. For wavelengths $\lambda \geq 1.1\mu m$, they use a camera with an InGaAs sensor [168] instead of a silicon-based one. . . 65
3.12 Schematic representation of MCF characterization using an Spatial light modulator (SLM). [174]. Phase mask to generate 4 spots having a 4 µm diameter, equivalent to the Mode field diameter (MFD) of the fiber cores. 66
3.13 4-SM-core fiber's output beam characterization at 1070 nm (fiber 4.1): (a) without lens (inset: distal face) ; (b) with an array of 4 micro-lenses (figure 2.21 (b)) (inset: array of the 4 parabolic micro-lenses). . 67
3.14 Simulated intensity of the fundamental mode of a 4 µm core with a micro-lens. Micro-lens base, height and Bézier weight W are 12 µm, 18.5 µm and 0.914 respectively. (a) For $\lambda = 1070$ nm: FWHM = 0.97 µm and WD = 3.7 µm. (b) For $\lambda = 1550$ nm FWHM = 1.1 µm and WD = 2.8 µm. 68
3.15 4-core fiber characterization at 1550 nm of lensed fiber from figure 2.21 (b) 68
3.16 (a) Top view of the 37 core fiber facet. (b) Output beam without lens at 1550nm. MFD = 7.5 ± 0.1 µm. 69
3.17 (a) Simulated intensity distribution for the fundamental mode of a 10 µm core at 1550 nm with a micro-lens. The lens base, height and Bézier weight W are 12 µm, 18.5 µm and 0.914, respectively. . FWHM = 0.84 µm. (b) Experimental characterization of the focused spot from one core with a micro-lens: FWHM = 0.85 ± 0.1 µm. . . . 69
3.18 (a) Simulated intensity distribution for the fundamental mode of a 4 µm core at 1070 nm with a micro-lens. The lens is as in figure 3.17. FWHM = 0.94 µm. (b) Experimental characterization of the focused spot from one core with a micro-lens: FWHM = 1 ± 0.1 µm. 70
3.19 Output intensity measurement from the 37 core fiber by global injection at 633 nm: (a) with, versus (b) without micro-lens array. Fiber 37.1. 70

4.1 Quantum well laser diode. The active layer thickness is usually around 1 µm, hence the emission surface is about $1\mu m\times$ (4 to 5) µm. The beam divergence along the vertical axis is superior to that of the horizontal one, which explains why, the ellipse's major axis switches from being along the horizontal axis in the near field to the vertical axis in the far field. [4] 74
4.2 Fourier-transform infrared spectroscopy (FT-IR) spectral transmittance of 20 µm PDMS and NOA61 layers sandwiched between two CaF_2 substrates. 75

4.3 ICL direct coupling into fluoride fiber (IFG) configuration. Measurements have been performed with and without the molded micro-lenses. The positioning adjustment of the fiber was performed using a 3D mechanical transation stage. 76

4.4 Simulated Inter-band Cascade Laser (ICL)-fiber coupling efficiency vs PDMS hemispherical micro-lens radius using Zemax. The plotted values are those registered at ICL-fiber distances that lead to maximum coupling for each micro-lens radius. (a) 9.5/125 fluoride fiber. (b) 30/125 fluoride fiber . Fresnel reflections are not taken into account. 76

4.5 Molded micro-lenses on fluoride fiber core with dimensions and curvature close to the optimal values obtained numerically. Fibers are SM (9.5/125) in (a) and (b), and MM (30/125) in (c) and (d). 77

4.6 Experimental evaluation of the ICL-fiber couplings. The black line represents the coupling without micro-lens (bare fiber). The colored lines represent coupling in several lensed fibers. Top: 9.5/125 fibers with micro-lens shown in figure 4.5 (a-b). Bottom: 30/125 fibers all with the micro-lens shown in figure 4.5 (c-d). 78

4.7 Temperature distribution simulation in the fiber/micro-lens/air system for the fundamental mode (CW) at 1070 nm. Left: 50/125 MM fiber. Right; 9.5/125 SM fiber. Incident power has been adapted to reach 110°C. Micro-lens has a 51.5 µm base diameter, 22 µm height and an W = 0.35. 81

4.8 Maximum temperature variation as function of the PDMS micro-lens's: (a) height, with base fixed at 10.5 µm; (b) base diameter, with height fixed at 15 µm. The W is 0.5 and the mean power is 2.5 W in both cases. The fiber is a SM fiber with a 9.5 µm core diameter. . . 82

4.9 Simulation of the evolution of the maximum temperature as a function of the laser power for two PDMS micro-lens heights 22 µm and 31 µm. Base diameter = 50 µm. Fiber SMF28. 83

4.10 (a) Schematic representation of the optical setup used to monitor the micro-lens submitted to a high power laser. (b) Experimental characterization of the beam arriving at the micro-lens tip (focal plane of the microscope objective). (c) Cross section of the beam in (b) showing a FWHM of 7.8 µm. 84

4.11 Lateral images of the NOA61 micro-lens' state (a) pre and (b) post laser power threshold crossing (5.95W). Top view of the micro-lens tip (a) before and (b) after destroying the micro-lens. 1070 nm, 100 ns, 100 kHz pulse laser focused on the lens with a FWHM of 7.8 µm. 85

4.12 Lateral view of the PDMS micro-lens' at: (a) low laser power (200 mW), (b) after destruction at high laser power (3.85 W), (c) after destruction with laser off. 1070 nm, 100 ns, 100 kHz pulse laser focused on the lens with a FWHM of 7.8 µm. 85

4.13 Fiber coupling equipped with a PDMS micro-lens at the entrance as a function of incident laser power. The coupling drops dramatically at 3.85 W due to the micro-lens damage. 1070 nm, 100 ns, 100 kHz pulse laser focused on the lens with a FWHM of 7.8 µm. 86

4.14 Scanning electron microscope (SEM) image of the punctured PDMS lens at 4 W laser power at 1070 nm (100 ns, 100 kHz pulse laser focused on the lens with a FWHM of 7.8 µm). 87
4.15 (a) SMF28 with micro-lens L2 in front to the silicon surface (a mirror image of the fiber is visible). (b) and (c) are etched dots and lines on silicon using 100 ns, 35 kHz, laser pulses at 1070 nm. 88
4.16 (a) Micro-lens (L3) with 200 µm spacer in NOA61. The focus spot profile and cross-sectional plot are represented in (b) and (c). (d) Micro-lens in front to the silicon surface (a mirror image of the fiber is visible). (e) Etched line at 10.2 mW and $400\mu m/s$. (f) Etched dots (1 ms) with laser power from 7.7 to 15.2 mW. 100 ns, 35 kHz, laser pulses at 1070 nm. 89

A.1 Beam intensity distribution in space upon interacting with a AR coated PDMS micro-lens with a Bézier weight going from 0.1 to 1. . . 96

B.1 Ray tracing of light generated by an ICL source, and its trajectory along: (a) plane, (b) lensed SM fiber and (c) plane, (d) lensed MM fiber. Both fibers' NA is 0.3 and the source's wavelength is 4.5 µm. . 97
B.2 Normalized coupling efficiency into SM fiber (9.5/125): (a) without lens as function of source to fiber distance, (b) with lens as function of source to fiber distance, (c) with lens as function of hemi-spherical lens' radius. 98
B.3 Normalized coupling efficiency into MM fiber (30/125): (a) without lens as function of source to fiber distance, (b) with lens as function of source to fiber distance, (c) with lens as function of hemi-spherical lens' radius. 98

List of Tables

1.1 Comparison of modeling methods to solve electromagnetic problems. 14
1.2 **Refractive micro-lens fabrication techniques with their respective limitations. (* indicates: incompatible with mid-IR fibers)** . . . 35

2.1 **Main differences between used polymers** . . . 42
2.2 **MCF characteristics and mold etching times.** . . . 54
2.3 **MCF Mold etching times and PDMS pre-curing time.** . . . 54

4.1 **Indexes and NA at $\lambda = 4.53$ and 5.26 µm of the fluoride SM and MM fibers. The SM 9.5/125 fiber has a 9.5 µm core diameter, while the MM 30/125 fiber has a 30 µm core diameter (125 represents the cladding diameter in µm).** . . . 75
4.2 Summary of measured average coupling efficiencies for the lensed-fibers shown in figure 4.5. . . . 79
4.3 Parameters used in the COMSOL heat transfer model. A silica fiber is considered. . . . 80

B.1 **coupling efficiency into SM fiber (9.5/125) equipped with an aspheric micro-lens.** . . . 99
B.2 **coupling efficiency into MM fiber (30/125) equipped with an aspheric micro-lens.** . . . 99

List of Acronyms

ω_0 Beam waist.

AR Anti-reflective.

FDTD Finite difference time domain.

FEM Finite element method.

FMM Modal Fourier method.

FT-IR Fourier-transform infrared spectroscopy.

FWHM Full width at half maximum.

HCF Hollow-core fiber.

HF Hydrofluoric acid.

ICL Inter-band Cascade Laser.

IR Infra-red.

LMA Large mode area.

MCF Multi-core fiber.

MFD Mode field diameter.

MIR Mid-IR.

MM Multi-mode.

NA Numerical aperture.

NOA61 Norland Optical Adhesive 61.

PDMS Polydimethylsiloxane.

PJ Photonic nano-jet.

QCL Quantum cascade Laser.

SEM Scanning electron microscope.

SLM Spatial light modulator.

SM Single-mode.

W Bézier weight.

WD Working distance.

General Introduction

Optical fibers have played a transformative role in the field of communication by revolutionizing data transmission capabilities. One of the key advantages of optical fibers is their ability to carry large amounts of information over long distances with minimal loss of signal quality. This high-speed data transmission capability has significantly improved communication networks, enabling faster and more reliable connections for various applications such as internet, telecommunication, and data centers [1].

The integration of optical fibers has revolutionized the design of optical systems, making them more compact, lightweight, and high-performing. By replacing traditional optical elements with fiber-based alternatives, such as fiber couplers, doped and inscribed optical fibers, fiber circulators, and shaped fiber tips, the overall size and complexity of optical systems can be significantly reduced.

The miniaturization enabled by optical fibers has numerous advantages. Firstly, it allows for the development of highly portable and handheld optical devices, making optical technologies more accessible and convenient for various applications. For example, fiber-based medical devices can be made compact and easily maneuverable, enabling minimally invasive procedures and improving patient comfort [2].

Compact fiber-based systems also offer enhanced performance and stability. The reduced size and integration of components minimize the risk of misalignments and improve overall system reliability. Moreover, the miniaturization of optical systems through the use of optical fibers enables the realization of high-density optical circuits and systems. By incorporating multiple fibers or multi-core fibers within a compact footprint, it becomes possible to increase the capacity and efficiency of optical networks, allowing for simultaneous transmission of multiple signals or data channels.

This thesis focuses on the crucial role of fiber micro-lenses in optimizing the performance of fiber optics by enabling efficient light coupling and focusing. The ability to design, fabricate, and characterize micro-lenses tailored to specific fiber types and applications is of great importance in advancing the capabilities of fiber-based systems. In addition, this thesis explores the working principles of fiber micro-lenses, their applications, and the various fabrication techniques. A major focus is then given on introducing a novel technique, developed by our group at ICube in collaboration with the Sétif University, that enables the molding of polymer micro-lenses on different types of optical fibers, specifically non-silica-based, micro-structured, and multi-core fibers. The technique allows the control of the lens shape and for example the fabrication of high curvature micro-lenses that can be deposited just on the fiber core. These micro-lenses open up new avenues for advanced applications. The particular ones that I have considered in my PhD work are light coupling of

inter-band cascade lasers (ICL)s into fluoride-based fibers, laser micro-processing and micro-structured fiber lensing.

This thesis's work, realized between October 2020 and July 2023, is presented in this manuscript under four chapters:

In chapter 1, the state of the art of fiber micro-lenses is explored, categorizing fabrication techniques based on their operating principles: refraction, diffraction, and resonance. While refractive micro-lenses are widely used, diffractive and resonant micro-lenses offer additional degrees of freedom and the capability to shape vector beams, enabling the generation of previously unattainable beam profiles. However, these advanced techniques are still new and lack sufficient development and refinement for practical implementation.
The chapter provides an overview of the various fabrication techniques for refractive micro-lenses, highlighting their advantages, limitations, and suitability for different applications and fiber types. Importantly, the thesis addresses the lack of solutions for non-silica-based fibers, such as fluoride-based fibers, which possess different properties and greater fragility compared to silica fibers. Existing techniques relying on grinding, heating, splicing, and laser machining are generally not be compatible with these fibers.

Chapter 2 details the fabrication procedure of micro-lenses on single-core fibers using the newly developed and proposed polymer molding technique. The quality of the fabricated micro-lenses is evaluated through surface roughness and geometry analysis, demonstrating high quality and stability. Additionally, a method for fabricating fiber spacers compatible with Mid-IR fibers is introduced, enabling precise control over the beam expansion length before interacting with the micro-lens. Challenges in fabricating micro-lenses on hollow-core fibers and multi-core fibers are also addressed through customized approaches, paving the way for various applications in fiber optics. We will show how we have succeeded to deposit 37 parabolic micro-lenses on a 37-cores fiber from the Phlam lab.

In Chapter 3, the focus shifts to the numerical and experimental characterizations of the newly fabricated micro-lenses. The primary objective is to evaluate the behavior of the emerging beam and identify potential losses as a function of the micro-lens curvature. The chapter shows how light focusing on spot size having one wavelength of full width at half maximum can be achieved with high micro-lens curvatures but also how the same result with larger working distances can be obtained using the spacer we have developed. Moreover, the employed simulations shed light on the tolerable experimental imperfections in micro-lens centering with respect to the fiber core. The subsequent experimental measurements are performed using various characterization setups, depending on the type of fiber, and serve as validation for the numerically obtained results.

Chapter 4 addresses several possible applications of our micro-lenses. The first one is the problem of shaping the tip of non-silica fibers, considering their low melting point and mechanical fragility. The chapter validates the compatibility of the

new micro-lens fabrication technique and utilizes it to enhance the coupling from Mid-IR inter-band cascade lasers (ICLs) into non-silica fibers. The optimal micro-lens design for both single-mode and multi-mode fibers is calculated using the Zemax software. Then, the damage thresholds of PDMS and NOA61 micro-lenses are investigated through a thermic numerical study followed by experimental verification with silica fiber. These validate that these micro-lenses can be employed in high-power laser applications with mean power of few watts, also in nanosecond pulse regime. Silicon etching at the micrometer scale is demonstrated.

Chapter 1

Optical Fiber micro-Lenses: fabrication techniques and Applications

In the early-1970s, the notion of micro-lens on optical fiber started surfacing in response to the growing necessity to improve the coupling efficiency of the light generated from laser diodes into optical fibers. At the time, diode lasers existed for only a few years, but due to their small size and efficiency, they presented a huge potential and later became the backbone of the commercialization of optical fiber telecommunication. The issue, however, was the extremely low coupling efficiencies between these diodes and optical fibers, especially SM ones ($\leq$8%) [3]. The reasons behind this low efficiency are the limited acceptance angle, or NA as explained in the section bellow, of optical fiber and the elliptical nature of the beams generated from diode lasers [4] (This is explained in more details in section 4.1). The first suggested solution to this problem was the use of micro-cylindrical-lens, but due to the difficulty in manufacturing and manipulating such a lens, other more practical solutions started emerging.
Throughout the years, it became clear that micro-lenses are essential components for not just diode-fiber coupling but also for the majority of applications involving optical fibers such as coupling in photonic integrated circuits [5], sensing [6–10], sub-diffraction laser processing [11], nanoparticle manipulation using optical tweezers [12] and more [13–16]. This chapter will include an explanation of micro-lenses working principle, the different fabrication methodologies, and the advantages and limitations of each.

1.1 Working principle of a fiber micro-lens

1.1.1 Light collection and coupling

1.1.1.1 Numerical aperture

The NA is the notion that describes the light-gathering capability of an optical fiber. This dimensionless number is dictated by the index difference between the fiber core and that of the cladding.

$$NA = \sqrt{{n_1}^2 - {n_2}^2} = n\sin(\theta_{max}) \tag{1.1}$$

Where n_1 represents the core's index, n_2 refers to the cladding's index, and n denotes the index of the external medium, typically 1 for air. θ_{max} corresponds to half the acceptance angle.
Given the presented information, it may be tempting to believe that increasing the difference between the two indexes would enhance the light-gathering ability of the fiber. While this is partially true, it also leads to a significant increase in the number of guided modes in the fiber. This may be an issue for various applications where there is a need to control the phase, which varies for each mode and is highly susceptible to fiber bendings. An uncontrolled phase can lead to interferences between the modes, resulting in a beam output pattern that resembles speckle [17]. However, this issue is resolved by single-mode (SM) fibers, which support only one mode - the fundamental mode denoted as LP_{01} (Linearly Polarized) under the low guiding approximation ($n_1/n_2 \approx 1$). The fundamental mode has a Gaussian-like profile. SM fibers are the most common and widely used fibers that guide only one mode. Not only the Numerical Aperture (NA), but also the physical core diameter of the fiber, plays a role in determining whether the fiber can support one or multiple modes. The relationship between NA, core diameter, and the number of guided modes in a step index optical fiber is described by the V number [18]. This dimensionless number can be interpreted as the optical frequency and is defined as:

$$V = 2\pi a\frac{NA}{\lambda_0} \tag{1.2}$$

where a represents the physical core radius and λ_0 is the free space wavelength. If the value of V is smaller than 2.405, then the fiber can only support a single mode per polarization at the considered wavelength. For large values of V, the number of modes with all possible polarization states can be approximated by:

$$N = V^2/2 \tag{1.3}$$

With N representing the number of modes.

This limits the NA due to the generally preferable low number of modes, hence the small acceptance cone of optical fibers. This is especially true in the case of SM fibers, where it is typically at around 12° (e.g SMF-28 fibers which are SM at a 1310 nm and above). For instance, a SM fiber with a cut-off wavelength of 633 nm, and a core diameter of 4 µm, must have a maximum NA of ≈ 0.12, thus an acceptance angle of $\approx 13.8°$.

Daisuke Kato et al., in 1973 [19], suggested the use of curved fiber end, such as that illustrated in figure 1.1 a), to increase the acceptance angle without interfering with the fiber number of modes. He demonstrated that by forming a spherical fiber end, the half-acceptance-angle becomes:

$$\theta = \arcsin\left[n_1\sin\left(\arcsin(\frac{a}{2r}) + \arccos(\frac{n_2}{n_1})\right)\right] - \arcsin(\frac{a}{2r}) \tag{1.4}$$

where r represents the radius of the spherical fiber end, and $r = \infty$ means a flat-ended facet. Figure 1.1 (b) shows that decreasing the fiber end radius significantly increases the acceptance angle, especially for MM fibers (with large core radius "a"

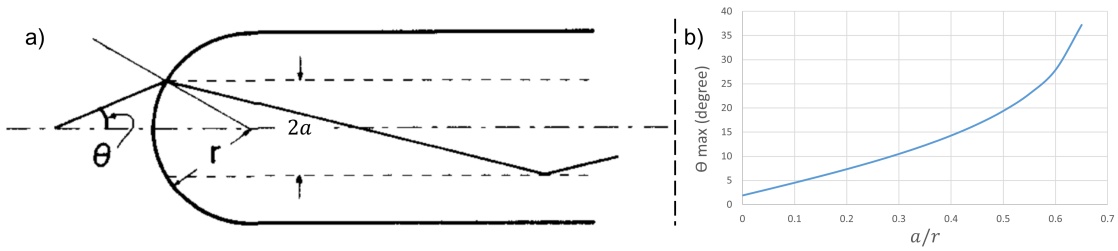

Figure 1.1: a) Representation of curved fiber end with radius r. b) Spherical fiber end half-acceptance-angle as a function of a/r. The considered indexes are those of a typical step index SM fiber: $n_1 = 1.4522$ and $n_2 = 1.4514$.

values). Let's consider the case of the SM fiber with $n_1 = 1.4522$, $n_2 = 1.4514$, and $a = 4\mu m$: its acceptance angle is 3.8° if the fiber end is flat, as shown in figure 1.1 b). But by curving the facet to a radius of 5 µm ($a/2r = 0.4$), the acceptance angle increases to 28.6°. However, such a small radius, of the same order of the fiber core, can be very hard or even impossible to achieve for an optical fiber with a cladding diameter of 125 µm, which is the standard and most common fiber diameter, specifically using the technique suggested by Daisuke Kato, known as thermal melting. Other methods are required. These methods will be thoroughly explained later in this chapter in section 1.2.

Radius of curvature

The radius of curvature is a concept used to describe the approximate circle of radius R at any point of the curve that best fits the highest number of adjacent points (as illustrated in figure 1.2). The formula for the radius of curvature at any point r for the curve $y = h(r)$ is given by [20]:

$$R = \frac{(1 + (\frac{\partial y}{\partial r})^2)^{\frac{3}{2}}}{\frac{\partial^2 y}{\partial r^2}} \tag{1.5}$$

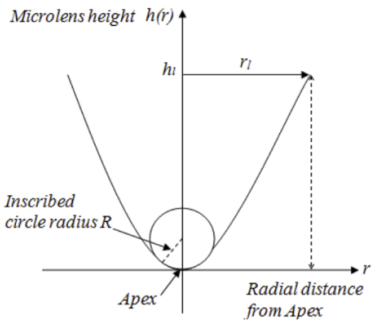

Figure 1.2: Radius of curvature of a parabolic curve. [20]

The radius of curvature of a micro-lens is always calculated at its Apex, and small radii represent high radii of curvatures, and vice versa. This concept will be particularly useful when talking about aspherical micro-lenses which we will encounter very often in this work.

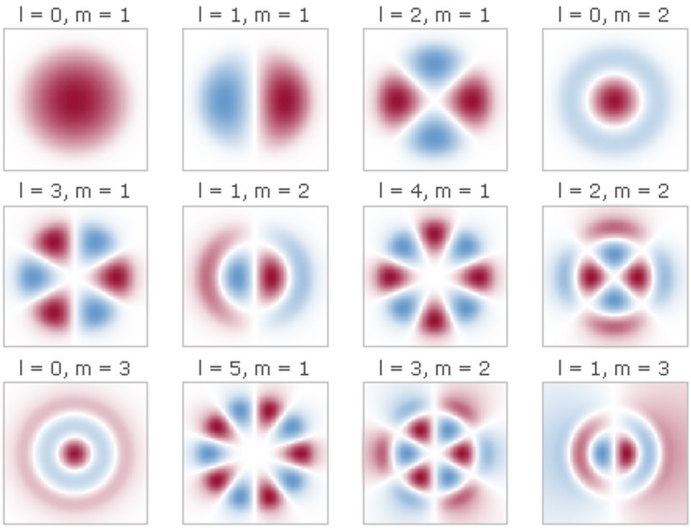

Figure 1.3: 2D representation electric field amplitude profiles for all the guided modes of a fiber with step index profile. The two colors indicate different signs of electric field values. [21]

While the NA describes the light gathering ability of an optical fiber through ray tracing, another approach that provides a more accurate representation is Gaussian beam propagation. This approach allows for the calculation of parameters such as the mode field diameter (MFD), Beam waist (ω_0), and beam divergence, which are crucial for understanding the performance of fiber optic systems. In order to calculate the percentage of light that will couple with a specific optical fiber mode (represented by the power distributions of the first few LP_{lm} fiber modes in Figure 1.3) from a light source (e.g., laser, waveguide, spatially modulated beam), we need to assess the matching of their electric fields at the fiber interface. The parameter that quantifies this is known as the field overlap integral and is defined as η:

$$\eta = \frac{|\iint_{-\infty}^{\infty} E_1(x,y)E_2^*(x,y)\,dx\,dy|^2}{|\iint_{-\infty}^{\infty} E_1(x,y)E_1^*(x,y)\,dx\,dy||\iint_{-\infty}^{\infty} E_2(x,y)E_1^*(x,y)\,dx\,dy|} \tag{1.6}$$

$\eta = 1$ corresponds to a perfect coupling and 0 to no coupling at all. E_1 and E_2 are the electric fields of the source and fiber respectively. When dealing with the fundamental modes (Gaussian-like beam profile), E_1 and E_2 are defines as follows:

$$E_1(x,y) = E_{10}\exp(\frac{-4(x^2+y^2)}{MFD_1^2}) \tag{1.7}$$

$$E_2(x,y) = E_{20}\exp(\frac{-4(x^2+y^2)}{MFD_2^2}) \tag{1.8}$$

The MFD equivalent to $2\omega_0$ (ω_0 being the waist) of the Gaussian beam. The MFD diameter of the fundamental mode of an optical fiber is given by the Marcuse relation shown in 1.9. This relationship is fairly accurate for V values above 1. For $V \geq 2.405$, it applies only to the fundamental mode.

$$MFD_{fund} \approx a\left(0.65 + \frac{1.619}{V^{\frac{3}{2}}} + \frac{2.879}{V^6}\right) \tag{1.9}$$

V is the normalized frequency from 1.2

In a perfect source-fiber alignment scenario, injecting equations 1.7 and 1.8 in 1.6, leads to:

$$\eta = \frac{4MFD_1^2 MFD_2^2}{(MFD_1^2 + MFD_2^2)^2} \tag{1.10}$$

However, if a misalignment Δx is introduced, equation 1.6 becomes:

$$\eta = \frac{4MFD_1^2 MFD_2^2}{(MFD_1^2 + MFD_2^2)^2} \exp(-\frac{8\Delta x^2}{MFD_1^2 + MFD_2^2}) \tag{1.11}$$

In case of an additional angle mismatch, the formula can be found in [22].

Ray transfer matrix

Studying the evolution of a Gaussian beam in free space or its interaction with optical elements, such as classical or micro-lenses, can be facilitated by utilizing the ABCD matrix [23].
In the context of this thesis, which focuses on the fabrication of micro-lenses for optical fibers, we will examine the lensed optical fiber depicted in Figure 1.4.
Regardless of whether the beam emerges from the fiber into free space or vice versa, the methodology remains consistent, with only the order of the matrices being swapped. When considering the propagation from the fiber to free space at the distal end, the transfer matrix M can be expressed as:

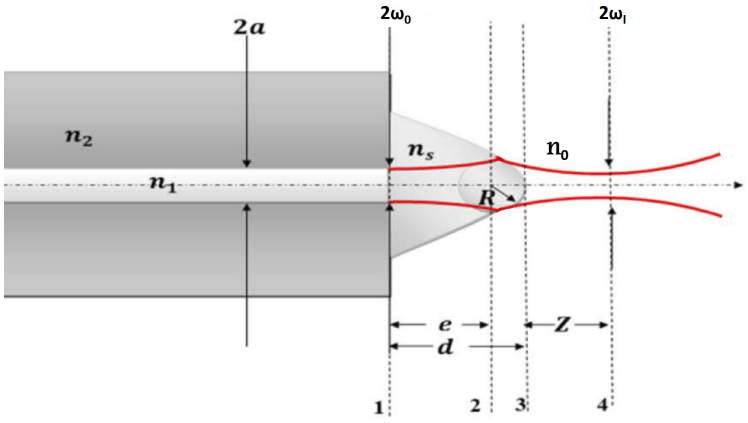

Figure 1.4: Gaussian beam propagation through fiber micro-lens. [23]

$$M = M_{34} M_{23} M_{12} \tag{1.12}$$

$$M = \begin{pmatrix} A & B \\ C & D \end{pmatrix} = \begin{pmatrix} 1 & Z \\ 0 & 1 \end{pmatrix} \times \begin{pmatrix} 1 & 0 \\ \frac{n_0 - n_s}{n_0 R} & \frac{n_s}{n_0} \end{pmatrix} \times \begin{pmatrix} 1 & \frac{d}{n_s} \\ 0 & 1 \end{pmatrix} \tag{1.13}$$

with

$$M_{12} = \begin{pmatrix} 1 & \frac{d}{n_s} \\ 0 & 1 \end{pmatrix} \tag{1.14}$$

$$M_{23} = \begin{pmatrix} 1 & 0 \\ \frac{n_0 - n_s}{n_0 R} & \frac{n_s}{n_0} \end{pmatrix} \tag{1.15}$$

$$M_{34} = \begin{pmatrix} 1 & Z \\ 0 & 1 \end{pmatrix} \tag{1.16}$$

R is the radius of curvature of the micro-lens; Z is the WD, in our case the distance from the micro-lens crest to the focus spot; n_s and n_0 are the refractive indexes of the micro-lens and surrounding medium, respectively; d is the lens thickness, and e is the minimum distance where the beam propagates inside the lens without encountering the lens-air interface.

The relationship between the beam in any two planes 1 and 2 in space is best described using the complex q parameter (q for plane 1 and q' for plane 2), which contains the wavefront's waist ω_0 and radius of curvature R_c information. q is defined as [24]:

$$q = -i\frac{\lambda}{\pi\omega_0^2} + \frac{1}{R_c} \tag{1.17}$$

and

$$q' = \frac{Aq + B}{Cq + D} \tag{1.18}$$

In the case of propagation from free space into fiber, the equation 1.12 becomes:

$$M = M_{12}M_{23}M_{34} \tag{1.19}$$

From this we can deduce that the position of the focus plane does not co-inside with that of the optimal light collection, since matrix multiplication is not commutative.

1.1.2 Beam focusing

The study of the beam focusing response using a micro-lens at the distal end of an optical fiber can be initially approximated using scalar Gaussian beam propagation, similar to the case of light coupling [23]. However, when the size of the micro-lens is on the order of a few wavelengths, the applicable physical laws change at this scale. In such cases, phenomena like the Photonic nano-jet (PJ) can arise, necessitating a rigorous vectorial electromagnetic wave theory to accurately describe the phenomenon.

1.1.2.1 Photonic nano-jet

PJs, as depicted in Figure 1.5 (a), are propagating beams of light that exhibit sub-diffraction-limited characteristics. They arise from the focusing of an electromagnetic wave by a dielectric medium with a diameter on the order of a few wavelengths [25, 26]. A PJ exhibits an exceptionally high spatial field concentration at the mesoscale, with power density (Figure 1.5 (b)) significantly surpassing that of the incident excitation wave [27, 28]. Reported concentration factors have reached 200 or higher [26]. The full width at half maximum (FWHM) of the beam at the focus can be smaller than half a wavelength [29–33], even as small as $\lambda/4$, effectively

surpassing the diffraction limit [34, 35]. Moreover, a PJ is a propagating beam (non-evanescent) capable of maintaining its sub-wavelength beam width along a path extending over 100λ [36]. The phenomenon of PJs is non-resonant and can occur across a broad range of dielectric media sizes, from 2λ to 1040λ [26].

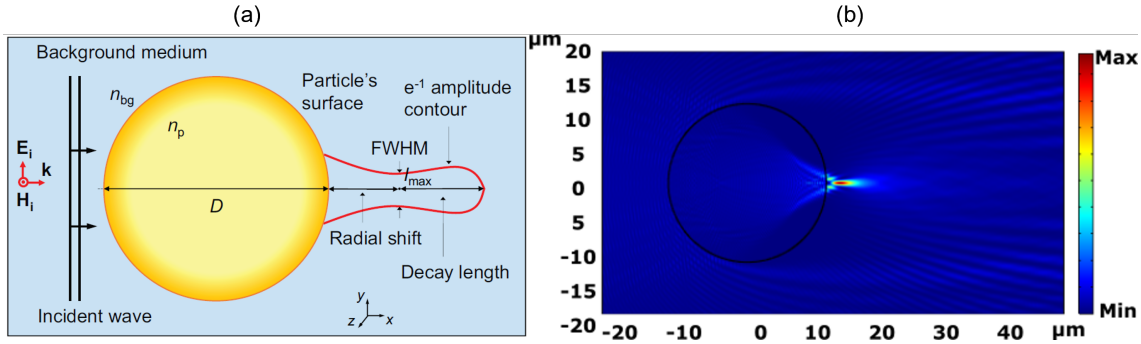

Figure 1.5: (a) Illustration of a photonic jet and its characteristic parameters. (b) 2D Photonic jet power density generated by a cylinder of diameter D = 24 µm and index $n_p = 1.5$, irradiated by an unitary plane wave

In addition to cylindrical or spherical objects, photonic jets (PJs) can be generated using various other geometrical forms. For instance, micro-spheres with concentric rings etched on their surfaces have been shown to generate PJs [37], as well as dielectric cuboids [38–40]. However, manipulating these objects can be challenging. To address this, some researchers have proposed the use of optical tweezers [41] to move micro-dielectric objects, while others have suggested employing waveguides with a spherical end-face [42]. Planar waveguides only yield 2D focusing or PJs. To achieve 3D PJs, Ghenuche et al. introduced a configuration using a hollow core photonic crystal fiber (HC-PCF) with a micro-sphere fixed at the end-face of the fiber's hollow core. This fiber-micro-sphere configuration resulted in a PJ with a FWHM of 540nm [43].

An alternative approach was introduced by the ICube laboratory in 2016, where an optical fiber with a shaped tip was proposed instead of using a micro-sphere. The shaping of the tip can be achieved through various methods, as described in Section 1.2. In this case, even though the photonic jet (PJ) is solely generated by the fundamental mode, multimode (MM) fibers with a core diameter of 100 µm were employed for the first time. The tip of the fiber was shaped using thermal melting techniques [44]. The achieved PJ full width at half maximum (FWHM) was 1 µm at a laser wavelength of 1.064 µm [45].

One significant advantage of the fibers with shaped tips, as shown in Figure 1.6, is that their WD is considerably larger compared to micro-spheres. This is advantageous because, with micro-spheres, it is often necessary to make physical contact with the sample, which can lead to a degradation in the quality of the sphere. Therefore, fibers with shaped tips address two major issues associated with micro-spheres by improving manipulation capabilities and increasing the working distance.

Indeed, since the PJ is primarily associated with the fundamental mode, SM fibers are more suitable for generating and manipulating PJs compared to MM fibers. However, a challenge arises when using SM fibers, as it requires the deposition of

high curvature micro-lenses directly on the fiber core. These lenses are more difficult to fabricate. This served as one of the motivations behind the work of this PhD.

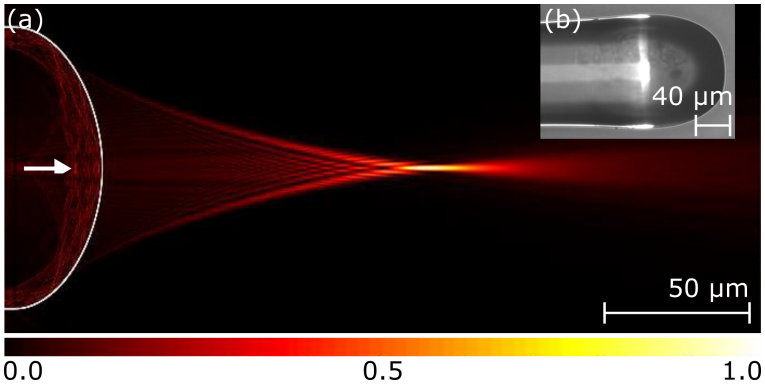

Figure 1.6: (a) Simulation of the intensity distribution generated by MM fiber with 100 µm core diameter. The fiber base diameter and tip length are 100 and 63 µm, respectively. The refractive indices of core and cladding are of 1.46 and 1.44, respectively. The wavelength is 633 nm and only the fundamental mode is excited. (b) Optical microscope view of a shaped fiber tip. [46]

Other beam types that cannot be explained using the Gaussian propagation approach also exist. These are for instance: Bessel beams [47] which can be generated by axicon shaped fiber tips [48], and vortex beams [49] that can only be achieved by diffractive or reflective micro-lenses (described in section 1.2).

The modeling of these unique beams requires solving the vector form of the propagation equation, which describes the interaction of an electromagnetic wave with a dielectric micro-object or nanostructure. The objective is to determine the distribution of the electromagnetic field both inside and outside the dielectric medium.

The methods used to rigorously model these phenomena can be categorized into two main categories: analytical (or modal) methods and numerical methods employing spatial discretization. Each method has its own advantages and limitations, necessitating a critical analysis. In this section, we will provide a brief overview of the most commonly used methods, highlighting their main characteristics.

1.1.2.2 Analytical (modal) methods

Analytical or modal methods, also known as exact methods of solution, offer a rigorously exact solution to Maxwell's equations or the propagation equations. Typically, these methods consider harmonic time evolution. They provide the solution in the form of an expansion using a basis of spatial functions called modes. These methods are generally efficient and require relatively low memory capacity. However, their applicability is often limited to simple geometries and material properties. Consequently, for structures with complex geometries, a transition to numerical approaches is often necessary.

Mie's theory Mie's theory is an analytical method that provides an exact solution to the propagation equations in the case of light interaction with a sphere (or a cylinder). This method is utilized to obtain an analytical solution for the scattering of the electromagnetic field around and inside a dielectric sphere using infinite series

(which are often truncated). In Mie theory, the total field outside the sphere is considered as the sum of the incident and scattered fields [50]. This theory has been employed to model the generation of photonic jets by dielectric spheres [26]. To determine the field distribution in the case of an ensemble of closely coupled microspheres, the Generalized Multiparticle Mie (GMM) theory can be applied [51].

Integral methods Methods based on the "boundary integral equation" approach involve transforming the calculation of the electromagnetic field, which is originally defined in the entire domain, into the evaluation of integrals along the boundaries of the domains [42]. These methods rely on the Huygens-Poincaré principle, which states that if the field is known on a closed surface encompassing all dielectric objects, it can be deduced at any point in space. The Green's function, which is a vectorial solution of the Helmholtz equation for a point excitation, is used in this process. Analytical expressions can be obtained for the incident waves, the Green's function, and the far-field radiated waves.

The boundary element method (BEM) can also be employed to discretize the boundaries and numerically handle the coupling between modes. One significant advantage of integral methods is that they do not require meshing the entire domain, which is a conceptual advantage compared to other differential techniques. The electromagnetic field at any point in space can be determined from the field information at the boundary. Researchers at ICube have developed such a method to study the generation of photonic jets at the exit of a planar waveguide with perfect conducting edges [42]. However, adapting this method to different geometries and dielectric guides has posed challenges.

Modal Fourier Method (FMM)

The Modal Fourier method (FMM), closely related to the rigorous coupled wave analysis (RCWA), was initially proposed by Knop in 1978 [52]. This technique has found widespread use in solving electromagnetic problems, particularly for the investigation of diffraction gratings. The popularity of the FMM can be attributed to its simplicity and versatility.

The FMM calculates the electromagnetic fields based on the staircase approximation. It involves considering a grating with elementary patterns that can have relatively complex shapes, such as a stack of rectangular layers. The modes within each region satisfy Maxwell's equations and the corresponding internal boundary conditions. The total field solution, which satisfies the boundary conditions between the different regions, is obtained by superimposing all the modes using the principle of superposition.

The FMM has been successfully employed to optimize photonic jets at the exit of radio frequency waveguides with rectangular tips [53, 54].

1.1.2.3 Numerical methods

Numerical methods are sometimes considered as "rigorous" although they are not expressed in analytical form when they are based on a vectorial solution of Maxwell's equations. They are based on spatial discretization of the studied domains. First, we will summarize the main characteristics of the most commonly used differential

methods for photonics modeling: the Finite difference time domain (FDTD) method for which there is discretization in space and time, and the Finite element method (FEM) often used to calculate the stationary states at a given frequency.

Finite difference time domain (FDTD) method

The FDTD method employs finite difference calculus to solve Maxwell's equations in both the spatial and temporal domains. It was developed by K. Yee in 1966 [55]. This method directly implements the spatial and temporal derivatives of Maxwell's equations to solve the time variation of electromagnetic waves within a finite space containing the object of interest. Numerical boundaries, such as Perfectly Matched Layers (PML), are introduced to account for absorption boundary conditions [56]. The FDTD method often requires long computation times as it calculates the temporal evolution of the intensity distribution step-by-step. It also necessitates a significant amount of memory due to the discretization, typically around $\lambda/10$.

Finite element method

The FEM is a differential method that discretizes the computational domain into a finite number of elements using geometric elements such as triangular meshes in 2D [57]. The first step in modeling is to divide the study space into sub-domains called elements or meshes, with common boundaries. Each element has defined nodes at its center. The FEM formulates a system of linear equations for each mesh, with the unknowns representing the fields to be determined. The FEM automatically enforces continuity conditions between elements, providing an accurate approximate solution. One advantage of the FEM is its robustness in modeling complex objects and material properties. However, it requires suitable meshing of the space and solving the propagation equations at each grid point, resulting in long computation times and large memory requirements. Nevertheless, the FEM is efficient for studying discontinuities and guided structures [58].

Based on the comparison of modeling methods presented in Table 1.1, we have chosen to use the FEM due to its versatility in handling different geometries and materials. Due to memory limitations, our study will focus on a 2D case. Alternatively, the Finite-Difference Time-Domain FDTD method could have been employed, but we have access to the "COMSOL Multiphysics" software, which is based on finite elements, at the ICube Laboratory.

In summary, after considering the various methods available for solving our electromagnetic problems, we have opted for the FEM due to its adaptability to different geometries and materials. However, due to memory constraints, we will restrict our study to a 2D case. To implement the FEM, we will utilize the "COMSOL Multiphysics" software.

1.1.2.4 Experimental characterization

The characterization of beams generated by shaped optical fiber tips involves measuring various beam parameters such as the beam quality factor "M^2", beam diameter or full width at half maximum (FWHM), Rayleigh length, and intensity distribution. The most commonly implemented method, proposed by Cohen and

Techniques	Benefits	Disadvantages
Mie's Theory	Fast, rigorous	Geometries: cylinders, spheres, ellipses
FDTD	Diverse geometries and materials	Large required memory and computing time
FEM	Diverse geometries and materials	Large required memory and computing time
Integral	No need to mesh the entire domain	Difficulty to adapt to complex geometries
MMF	Efficient for grating and guides	Less suitable for curved shapes

Table 1.1: Comparison of modeling methods to solve electromagnetic problems.

Lannes in 1974 [59] and widely used in recent studies [46, 60, 61], relies on the use of a shallow depth of field microscope objective. This objective allows for plane-by-plane observation of the generated beam. Shallow depth of field objectives typically have high magnifications ($\geq \times 40$). The depth of field (d) of an objective is given by the equation:

$$d = \pm \frac{\lambda \sqrt{n^2 - NA^2}}{2NA^2} \tag{1.20}$$

Here, λ represents the wavelength, n is the refractive index of the medium surrounding the objective, and NA is the numerical aperture of the objective. High NA objectives are typically associated with high magnifications. In our team, we have developed a characterization setup (Figure 1.7) [46] using a microscope objective with a $\times 100$ magnification and a NA of 0.9, resulting in a depth of field of $d = 288$ nm at a wavelength of $\lambda = 1070$ nm. The objective is mounted on a piezo-electric stage that enables precise plane-by-plane scanning of the beam. I have used this setup to obtain experimental characterization results in chapter 3.

While this characterization method is accurate ($\pm 100nm$) and easy to implement, it faces a challenge in determining the WD. The detection of the position of the shaped fiber tip in space, relying on transmitted light, can be difficult due to the high transparency of the fiber tip. To overcome this, a light source emitting light on a beam splitter can be added between the relay lens (RL) and the microscope objective (MO). This allows for imaging of the fiber tip by reflection. Other setups with interferometric configuration also allow the measurement of phase.

Alternatively, a less common characterization method can be employed, which does not require a microscope objective but instead uses a tapered optical fiber connected to a power meter. The tapered optical fiber is mounted on a motorized xyz stage, enabling a 3D scan of the beam. By associating a coupling value with each position in the scanned space, the beam can be reconstructed. The tapered fiber tip enhances the measurement resolution. While this technique is slower than the previously mentioned method, it simplifies the task of measuring the WD. The two fibers (the shaped fiber to be characterized and the tapered fiber acting as a probe) can be monitored laterally using a magnifying optical system. A reference position can be determined when the two fibers are in contact, and the WD corresponds to

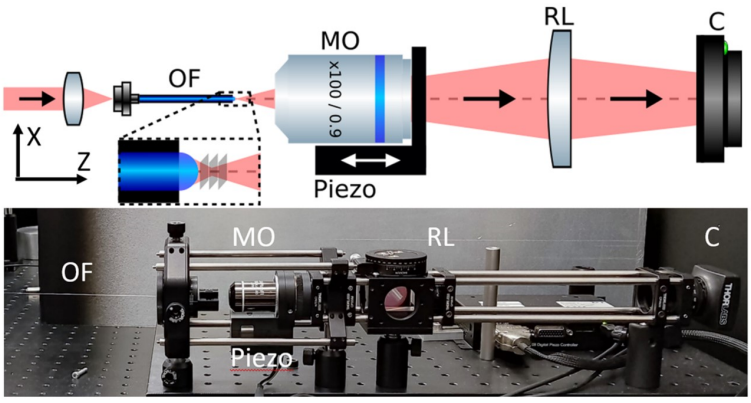

Figure 1.7: Imaging system for beam characterization: illustration and photo. OF, optical fiber; MO, microscope objective; RL, relay lens; C, camera. Black-dashed-line box represents a close-up view of the focused beam through the shaped fiber tip.

the distance from this reference to the position where the highest coupled power is obtained [62, 63]. Figure 1.8 shows an example of this method.

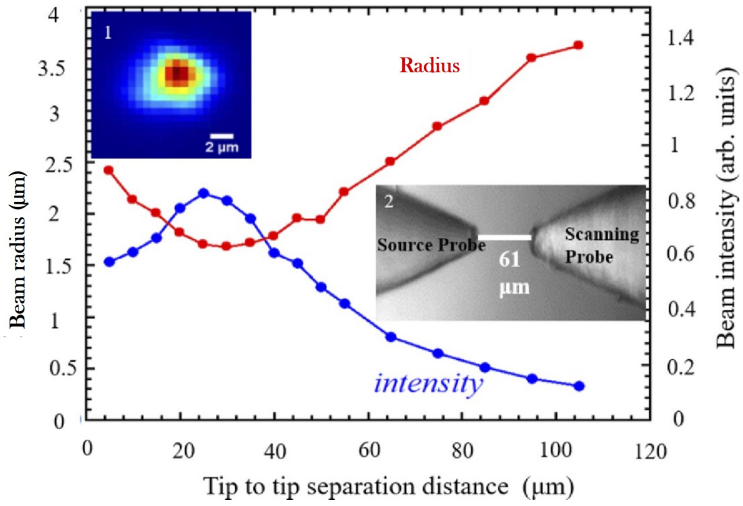

Figure 1.8: Beam radius and intensity as a function of fibers tip-to-tip separation in water. Inset 1: 2D Intensity map at beam waist for 808 nm light. Tip-to-tip distance is 24.69 µm. Inset 2: Shaped fiber tip acting as source and tapered fiber probe with a separation of 61 µm as seen by a lateral magnifying optical system. [64]

1.2 Fabrication Techniques for single-core fibers

Fiber Micro-lenses can be classified into three categories represented in their chronological order of appearance in figure 1.9:

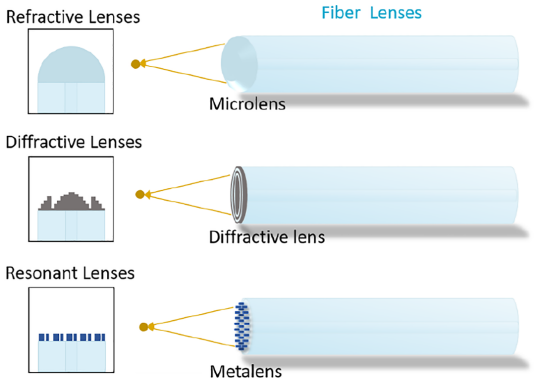

Figure 1.9: Three categories of micro-lenses. Diffractive and resonant lenses are also referred to as flat lenses. [65]

1.2.1 Refractive micro-lenses

The first type of micro-lenses are also the ones that first appeared chronologically. These micro-lenses, resemble bulk lenses in terms of their geometry and structure; they are attached or formed on the tip of an optical fiber. These lenses share some similarities with conventional bulk lenses because they obey, to a certain extent, the refraction laws of geometric optics.

Their smaller size allows them to be more easily integrated onto fibers than larger lenses. The micro-lens geometry and material are the most important factors affecting performance. Over the years, various designs have been proposed to improve power delivery and stability. Thanks to their small size and to the few required components, lensed fibers are easier to align, which is extremely beneficial for compact and stable packaging, such as the one represented in figure 1.10.

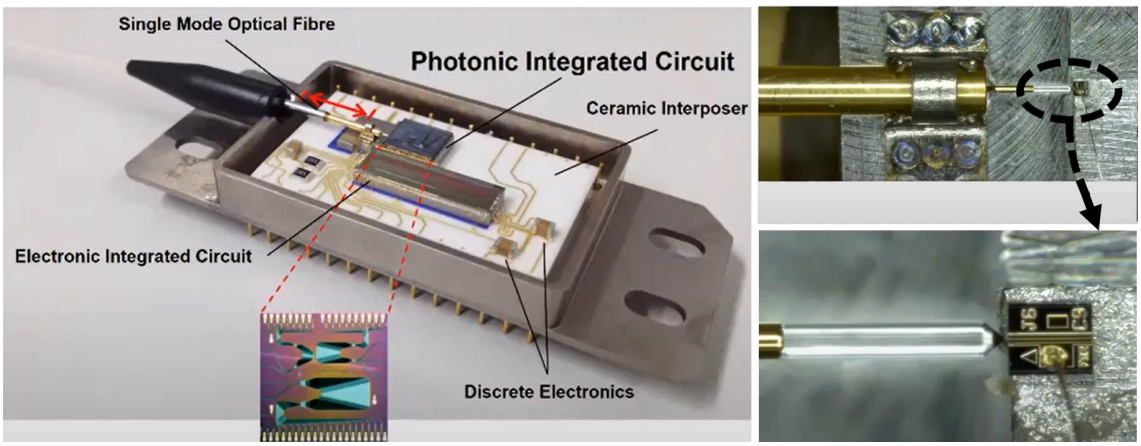

Figure 1.10: High efficiency diode laser-fiber coupling in a stable and compact packaging. [66]

1.2.1.1 Photopolymerization and photolithography

In 1973, L. G. Cohen and M. V. Schneider created the first polymer micro-lens on the core of a SM fiber [59] by depositing a thin photoresist film on the fiber tip and then exposing it to UV light propagated along the fiber core as shown in figure

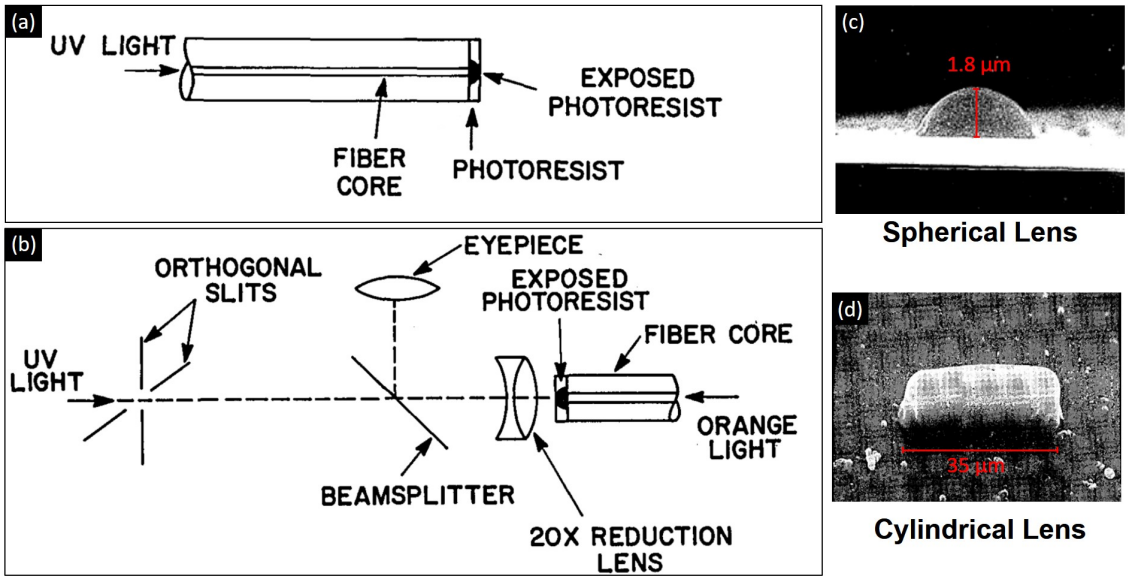

Figure 1.11: a) Generation of a self-aligned hemi-spherical micro-lens by photpolymerzation. c) Generation of a cylindrical micro-lens by photolithography. b) and d): Scanning electron microscope image of the fabricated micro-lens by the procedures depicted in a) and c), respectively [59].

1.11 (a). The unexposed polymer is rinsed off afterwards, leaving a hemispherical polymer lens on the fiber core. This technique allows a self-aligned micro-lens with the fiber core and works well with SM fibers. The fabricated micro-lens height and base are reported to be 1.8 and 4.8 µm, respectively, as seen in figure 1.11 (c). The obtained micro-lens shape and smoothness can be attributed to the Gaussian beam or fundamental mode that emerges from the fiber core.

The authors also managed to created hemicylindrical micro-lenses by photolithography. The experimental setup is depicted in figure 1.11 (b). Two orthogonal slits, which act as a mask for the micro-lens cylindrical shape, are set in front of a UV source. The UV beam is later focused onto the fiber core thanks to a 20× microscope objective. To locate the fiber core before UV exposure, orange light is first injected into the fiber from the other end. This projects the core's image formed by the objective onto an eyepiece after reflecting off a beam splitter. Overlapping the UV and the orange beams insures proper centering of the lens on the fiber core. The control over the lens shape was achieved by subjecting the photoresist to three stages of exposure (10 s, 10 s, 20 s) at consecutively wider slit separation. Figure 1.11 (d) shows the obtained lens image.

These techniques have greatly evolved throughout the years, and have been implemented in a wide range of applications. For instance, Renaud Bachelot et al. in 2001 [67], created by photopolymerization, polymer tips for single and few mode fibers. The fabricated tips height and radii of curvature were controlled by varying the UV exposure time of the polymer. The longer the exposure the higher the radius of curvature. Figure 1.12 (a) shows the shape of the obtained tips on a SM fiber, while figure 1.12 (b) and (c) show a 0.6 and 2.5 µm tip radii of curvatures, respectively. The exposure time of the former is 2 s and that of the latter is 45 s. Similar procedure has been employed for few mode fibers, generating polymer tips that look like the excited fiber mode. An example of this can be seen in figure 1.12

(d), where UV light was injected into the LP_{21} mode of the fiber, creating a 4 peak tip. These kinds of tips have proven to greatly enhance the coupling of incident light into the fiber modes they represent with minimal effort, without the need of shaping the beam, for example using a SLM [68].

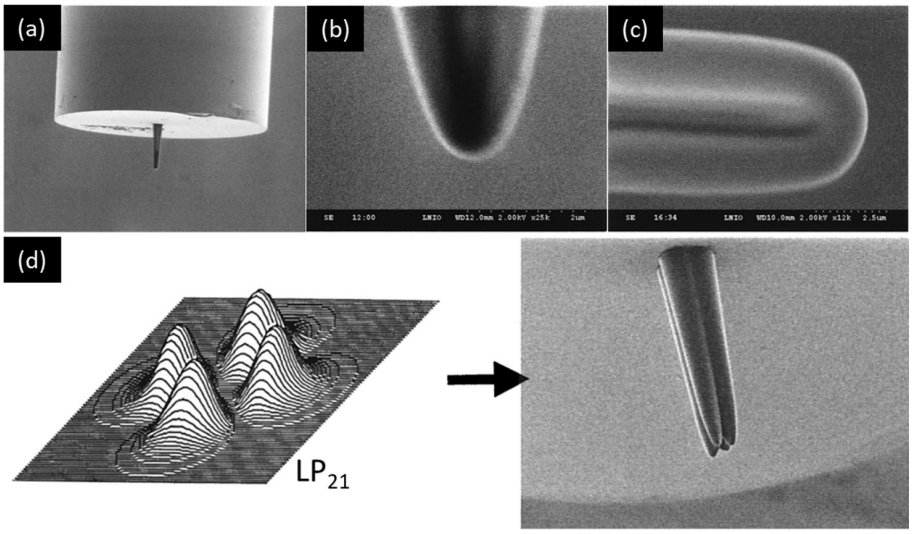

Figure 1.12: (a) Formed polymer tip over the core of a SM fiber (image dimension: 150 by 118 µm). (b) 0.6 µm radius of curvature tip cured for 2 s. (c) 2.5 µm radius of curvature tip cured for 45 s [67]. (d) LP_{21} mode injected into the fiber and the resulting polymer fiber tip [68].

The same type of fiber tip was later revisited with an emphasis on the focusing potential for the fabrication of optical fiber tweezers [69]. 5 µm yeast cells were successfully trapped in the xy plane (2D trapping) at a 6 µm distance from the polymeric tip, using a 40 mW - 980 nm continuous laser.

As for photolithography, only a few attempted later to use it for the fabrication of refractive micro-lenses due to the challenges it presents, and because of the availability of alternative technique. However, it has been widely used to fabricate diffractive and resonant micro-lenses [70], due to the possibility of making complex structures such as the ones shown in sections 1.2.2 and 1.2.3.

An interesting method is presented by Hongmei Zou [71]. Instead of using a mask, they substituted it with a tapered fiber, that will directly polymerize the UV resin without the need for a reduction lens to shrink the image of the mask. The employed procedure is represented in figure 1.13 (a) to (d). The tapered fiber (axicon shaped) is achieved by HF etching, a process described later in section 1.2.1.5. The tapered fiber generate a low divergence and small diameter beam known as "Bessel beam" [47, 72]. This procedure was named direct laser write or laser printing and the resulting micro-lens is shown in figure 1.13 (e).

Another more sophisticated approach than this technique appeared earlier in 2011, and relied on two or multi-photon direct laser writing [74]. Direct-writing technologies has the ability to create three-dimensional shapes accurately and precisely. When it comes to laser-based direct writing methods, two-photon lithography (TPL), also known as two-photon polymerization (TPP) stands out for its unmatched ability to construct well-defined 3D nanostructures with exceptional spa-

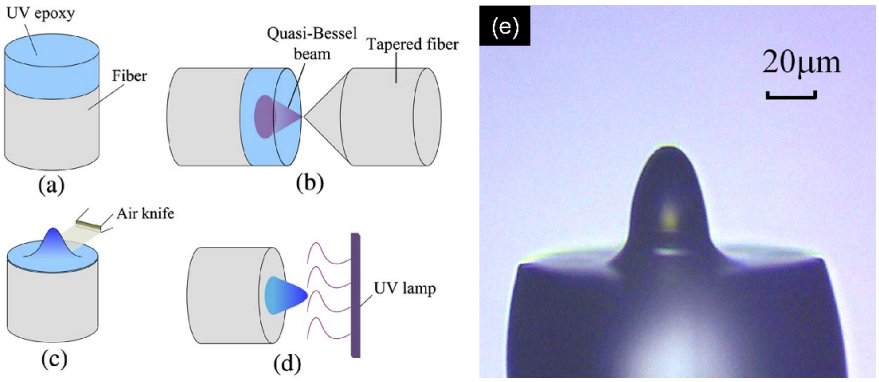

Figure 1.13: (a) A thin layer of UV epoxy corresponding to the final micro-lens height is deposited on the fiber end. (b) The epoxy covering the fiber core is exposed to UV light emerging from a tapered fiber after careful alignment. (c) Unexposed polymer is removed using an air knife. (d) Final UV exposure for complete curing. (e) Resulting micro-lens on SM end [71].

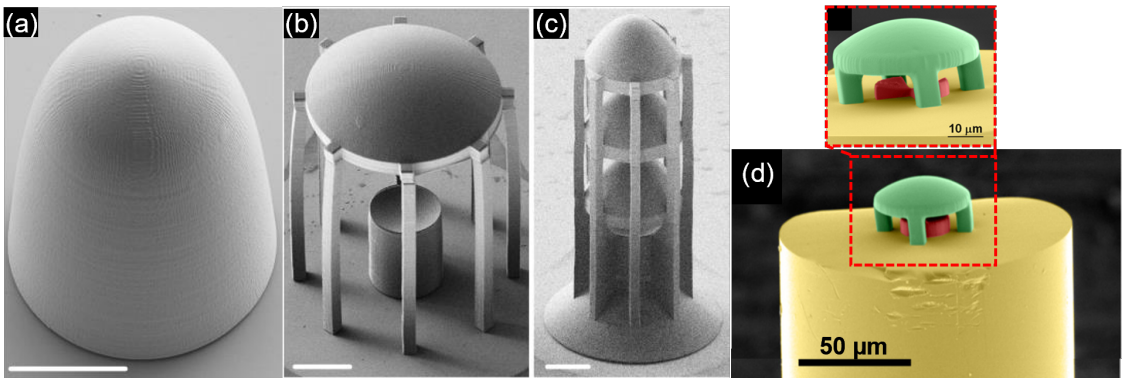

Figure 1.14: Fiber (a) High NA lens (b) Beam expander (c) Multi-lens beam expander (All scale bars represent 20 µm) (d) SU8 polymer plano-convex and plano-concave lens combination (radii of curvature are 29.5 and -23.1 µm, respectively). All fabricated by two photon polymerization [73].

tial resolutions. By utilizing laser beams with intensities just above the threshold for polymerization, sub-diffraction-limit feature sizes and localized polymerization can be achieved. The use of two-photon absorption (TPA) in rapid prototyping offers two significant advantages over conventional single-photon absorption. Firstly, because most commercially available polymers have minimal linear absorption in the near-infrared (NIR) region, the laser beam can deeply penetrate materials and induce polymerization from the inside without initiating any photochemical processes outside of the focal volume. Secondly, the quadratic dependence of the polymerization rate on light intensity allows for a high degree of 3D spatial resolution, resulting in much greater accuracy than single-photon processes. To achieve this, a solid-state laser with an ultrashort pulse-width of less than 100 fs (typically a Ti-Sapphire laser) is used in combination with a high NA objective lens to tightly focus the controlled laser beam onto a photocurable resin. This produces photo density profiles with an equal number of photons at all cross-sections of the focused spot. The resin is only exposed within the focal volume, also known as a voxel (a volumetric pixel that is generally ellipsoidal in shape [75]), allowing for a 3D resolution. By using a

high NA objective lens, the laser can be closely focused onto the resin, enabling a high photon density near the focal point, resulting in the fabrication of sub-100 nm structures [76].

This technique was later first commercialized by Nanoscribe in a very practical 3D nanoprinting machine [77], making it one of the most widely adopted technique due to its designs flexibility. The kind of refractive lenses that can be obtained by TPP are shown in figure 1.14 [73]. This technique is also of great value for the fabrication of diffractive and resonant lenses as seen in sections 1.2.2 and 1.2.3.

1.2.1.2 Thermal melting

From the beginning of modern optical fiber development, Daisuke Kato, in 1973 [19] demonstrated that by melting the optical fiber tip thermally, naturally a spherical surface is achieved. The longer the tip is heated, the larger the sphere's radius. Examples of the generated tips are shown in figure 1.15.

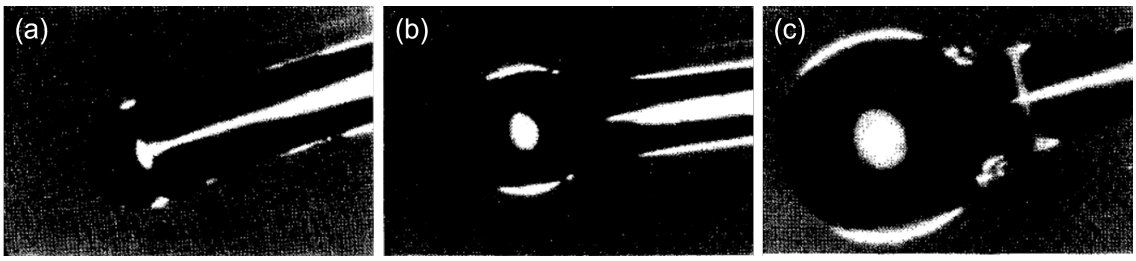

Figure 1.15: spherical fiber ends formed by thermal melting. Each fiber has a 100 µm diameter, and the end has a 50 µm radius of curvature (a), 75 µm (b), and 125 µm (c) [19]

These fiber tips improved by 5.2 times the light coupling between a GaAs laser diode and 50/100 MM optical fibers. It was also mentioned, for the first time, in their paper that these tips can be used to couple light between two fibers.

Due to the lack of repeatability in controlling the sphere's radius using this technique, it was later replaced by a process called electric arc discharge. Both however, were directly applied at the fiber tip (unlike what is presented in the next section), struggle in creating high curvature faces and proportionally melt the core and the cladding. This leads to potentially undesirable deformation and enlargement of the core. Meaning that this could alter the properties of the fiber at the tip by making it for instance MM even though it was originally a SM fiber.

1.2.1.3 Electric arc discharge

It is widely recognized that electric arcs have the capability to selectively melt silica-based fibers, resulting in spherically shaped fiber ends. Initially developed for precise fusion or welding of two fibers, this technique has also been discovered to create spherical fiber ends with greater repeatability compared to thermal pulling. In 1980, Jun-ichi YAMADA et al. implemented this method to deposit silica micro-lenses with significantly higher radii of curvature, as depicted in Figure 1.16 (b)(c) and (d). The silica material used to create the lens is sourced from a rod that is smaller than the fiber itself. This rod is positioned in front of the fiber, ensuring

that the resulting lens fully covers the fiber core while only partially covering the cladding.

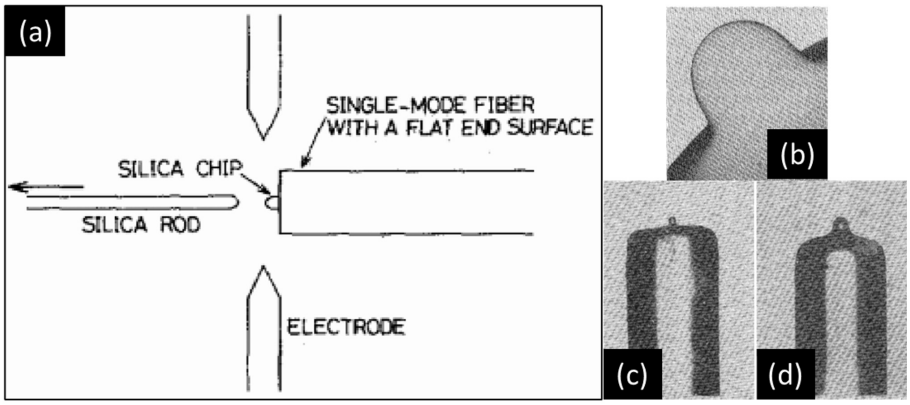

Figure 1.16: (a) Arcing setup used to deposit a silica micro-lens on SM fiber core. (b) Scanning electron photomicrograph of micro-lens with 17 µm radius. (c) and (d) Photographs of silica micro-lenses on 190 µm outer diameter fiber. The radius of each is 8.5 and 17.5 µm, respectively.

This technique (illustrated in figure 1.16) involves aligning and placing a 30–50 µm silica rod in contact with a SM fiber end, where the micro-lens should be deposited. The alignment is achieved by sending visible laser light into the opposite end of the fiber; the light emitted from the fiber is received by the rod, and the rod is placed at the position where the transmitted light is maximized. Afterwards, an arc is applied to melt the end of the rod and attach it to the fiber end face. The rod is quickly pulled, leaving only the appropriate amount of glass on the fiber end face. The amount of glass deposited can be controlled by the position of the arc along the fiber axis. Further arc heating forms a hemispherical lens on the fiber end face. The diameter of the lens is controlled by the volume of glass attached to the fiber end, and the duration of the arc discharge to form the hemispherical lens. The obtained micro-lenses are described as being hemi-spherical and were used to enhance the coupling between a semi-conductor lasers characterized by their circular beam cross section (InGaAsP laser emitting at 1.29 µm in their case) and SM optical fibers. The reported improvement is of 4.4 dB.

To further improve the coupling between diode lasers with non-circular beam cross sections (especially elliptical one) and optical fibers, C.A. Edwards et al.[78], and H. M. Presby et al. [79], in 1993, demonstrated that hyperbolic-micro-lenses are superior to hemi-spherical ones and they managed to fabricate them by CO_2 laser melting (More details in section 1.2.1.4). Later in 2005, M. Thual et al. [80] have also proposed splicing hyperbolic micro-lenses fabricated using graded-index fibre strands for quantum dot devices coupling to polarisation-maintaining optical fibres.

Major improvement to the electric arcing process has been introduced in 2001 by Chung-Hao Tien et al. [81]. By splicing a pure silica coreless fiber to a SM fiber, the beam expands before encountering the hemi-spherical micro-lens formed by electric arc discharge. This reduces the diffraction effect and allows higher focusing. The concept is illustrated in figure 1.17 and the beam expansion region is called spacer.

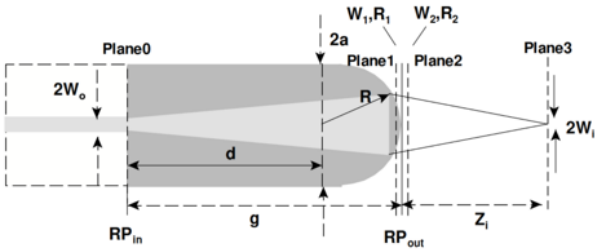

Figure 1.17: Coreless fiber spliced to a SM fiber. Beam is expanded before focusing to get smaller focused beams[81].

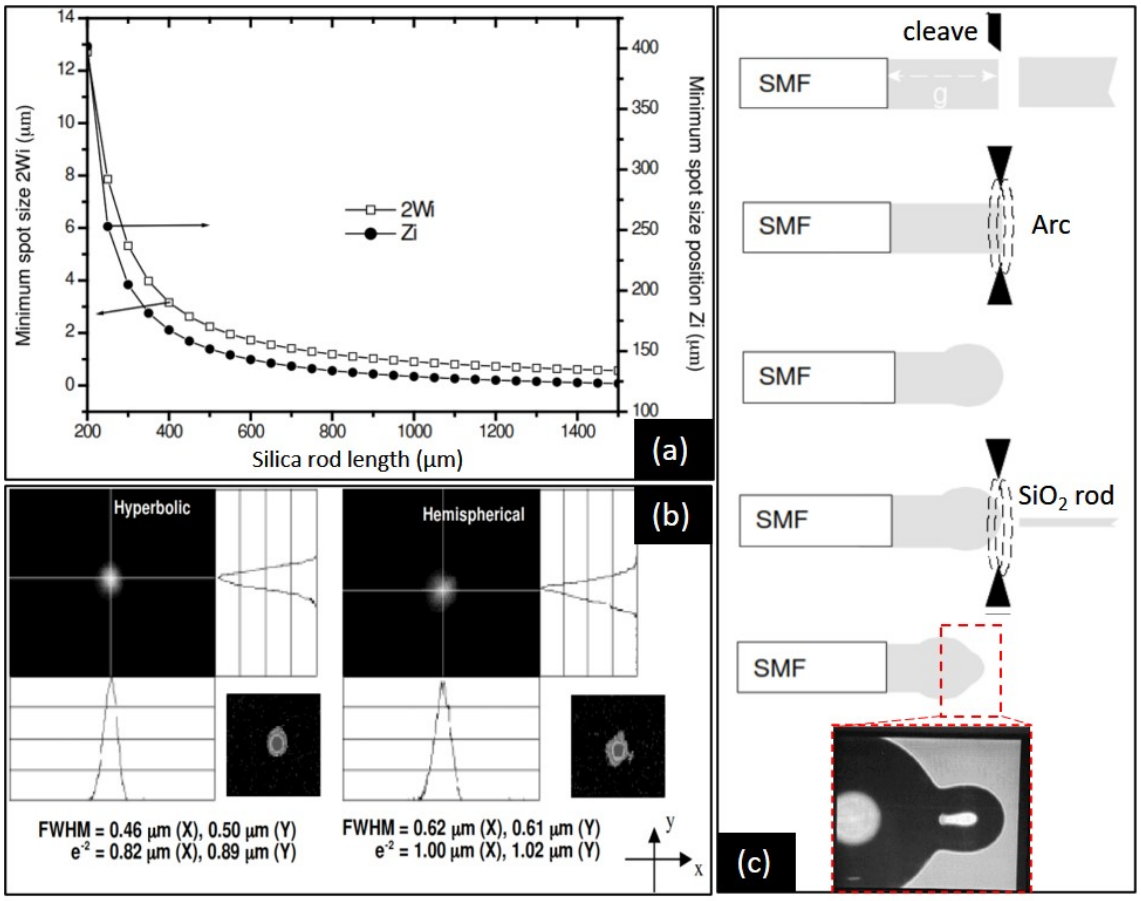

Figure 1.18: (a) Spot size and WD as a function of the coreless fiber length. (b) Focus spot characterization of the hemi-spherical vs hyperbolic lenses; hemi-spherical lens suffers from spherical aberrations. (c) Fabrication procedure of hyperbolic micro-lens [81].

The wavelength considered in their study is λ= 633 nm, and the fiber core is 4 µm, thus the MFD of the fundamental mode is about 4.3 µm. The radius of curvature of the silica-air interface is 62.5 µm. Figure 1.18 (a) show that, the length of the coreless fiber, must be at least 350 µm in order to have a spot smaller than the MFD of the fiber. Longer spacers lead to higher focusing capabilities at the expense of shorter WD. This type of hemispherical micro-lenses suffers from spherical aberrations. Solving this required splicing another hyperbolic micro-lens by electric arcing on top of the hemispherical micro-lens. The fabrication procedure of this micro-lens

and the resulting focus spot are shown in figure 1.18 (b) and (c), respectively. The FWHM achieved with this lens is less than λ.

Another type of micro-lenses that is also attached to the fiber by splicing, called GRIN (graded index), has been introduced by M. Thual et al. in 1996 [82]. This micro-lens gained a lot of attention due to its compatibility with SM fibers, its long WD and the high quality beams it provides [83].

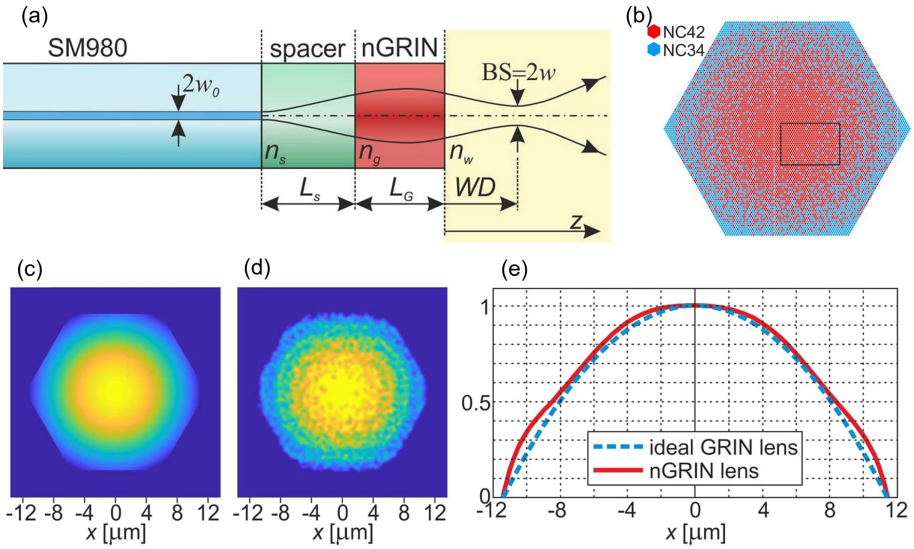

Figure 1.19: (a) GRIN lens splicing configuration and beam spot size evolution. (b) Distribution of borosilicate rods to create a graded index: NC42 (n=1.56895) and NC34 (n=1.56078). GRIN lens index profile: (c) ideal (theoretical), (d) experimental, and (e) ideal (theoretical) vs experimental [84].

A GRIN lens usually has the standard 125 µm fiber diameter and has a large graded index core. This is then cleaved, at the required length, to form the micro-lens on the optical fiber on which it is spliced by an electric arc (figure 1.19 (a)). Obtaining a GRIN lens can be achieved by doping the silica core by an element that increases its refractive index. More information about silica doping can be found in section 2.1.1.

For GRIN lenses to work effectively with SM fibers, the beam must be first expanded in a silica coreless fiber rod as illustrated in figure 1.19 (a).

More recently, in 2018, R. Kasztekanic et al. demonstrated the possibility of creating nanostructured GRIN lenses (nGRIN) using a technique that does not rely on doping. Their manufacturing procedure is similar to that of step-index optical fibers, in a sense that a preform is first created, then set in a drawing tower to get the final shape and diameter. But, unlike step-index optical fibers, their nGRIN fiber is not just made from a core and a cladding but of almost 10000 rods made of two different indexes. The percentage of the rods with the higher index is almost 100% in the center, but more and more rods are introduced by moving radially towards the edges (figure 1.19 b)). This will create an effective index profile that is almost parabolic [84]. Figure 1.19 d) and e) show the deviation from the ideal nGRIN lens represented in figure 1.19 (c).

1.2.1.4 CO2 laser melting

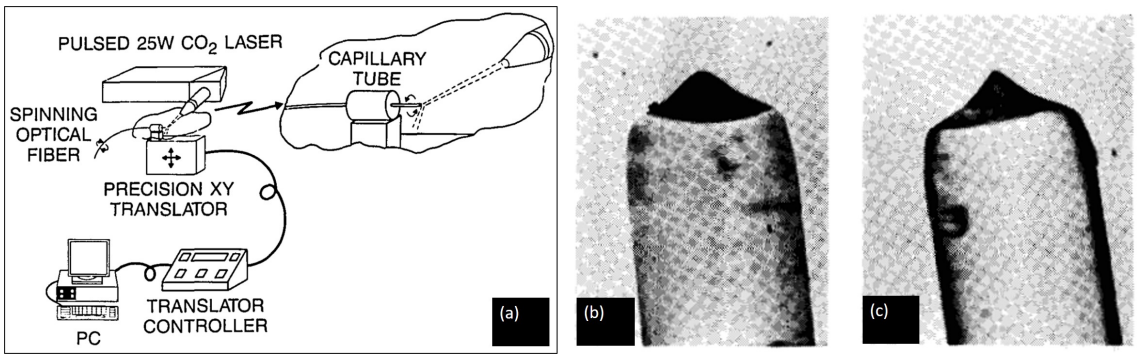

Figure 1.20: (a) CO_2 micromachining fabrication setup [85]. (b) and (c) Photographs of asymmetric hyperbolic micro-lenses [78, 79].

CO_2 lasers emit at a wavelength 9-10 µm, a region where silica glass is highly absorbent. This makes CO_2 laser is one of the best contenders to glass machining [86]. CO_2 laser melting of fiber tips first appeared in 1990 [85], as a substitute to chemical etching, that will be presented in the next section (1.2.1.5). The advantages of this technique are the high precision and repeatability. It relies on the evaporation of the parts subjected to the laser pulses allowing minimal melting to preserve the fibers' structure. The fiber is spun, as illustrated in figure 1.20 (a), around its axis while the laser is focused on its tip leading to perfectly symmetric, intrinsic micro-lenses. Christopher A et al.[78], and H. M. Presby et al. [79], used this technique to create asymmetric hyperbolic micro-lenses such as the ones represented in figure 1.20 (b) and (c). These micro-lenses led to more than 80% coupling efficiency between an elliptical beam and a SM fiber. Moreover, elliptical beams were successfully generated using the fabricated hyperbolic micro-lenses.

1.2.1.5 Chemical etching

HF is capable of etching silica by chemical corrosion. The etching rate depends on the doping of the fiber and the acid concentration and temperature. Based on this, in 1982, G. Eisenstein and D. Vitello suggested a simple method of making a tapered micro-lens, achieved by selective chemical etching of the fiber [87]. A conventional SM fiber is etched in a solution consisting of 40% HF and ammonium fluoride and 60% distilled water. The etch rate is higher in the phosphorus-doped region (the cladding) and lower in the core, doped with germanium (Ge). As a result, the fiber tip becomes conical as shown in figure 1.21.

A tapered micro-lens is naturally created and self-centered. The height of the cones, is controlled by the etching time, the HF concentration, and the solution temperature. The base size of the cone depends on the cross section of the core and gradually widens with longer etching times. HF is a widely used fluoride compound. It is an aqueous solution, highly corrosive and dangerous to living tissues. HF can be stored in polyethylene, fluorocarbon, teflon, or lead containers. It is prepared from a solution of calcium fluoride and concentrated sulfuric acid [88]. When an optical fibre is immersed in this acid, the main silica SiO_2, the main constituent of the glass is dissolved (consumed) by the following reaction which gives rise to to the

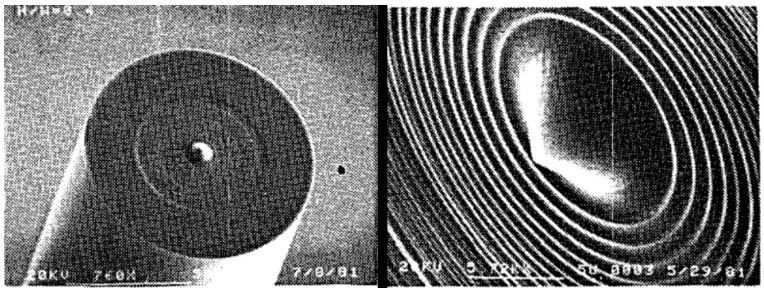

Figure 1.21: Scanning electron photomicrograph of the first SM fiber micro-lens created by chemical etching [87].

formation of hexafluorosilicic acid [89, 90]:

$$SiO_2 + 6HF \rightarrow H_2SiF_6 + 2H_2O \tag{1.21}$$

Chemical etching offers several advantages. The fabrication system is rather easy to implement and inexpensive. The core of the fiber remains present all the way to the tip. The end of the optical fiber can be changed from the original cylindrical shape to the convex conical finale shape (tip), passing through a set of intermediate states described in figure 1.22 (a). We have taken advantage of in this technique in our newly developed fabrication method, which will be described in the next chapter.

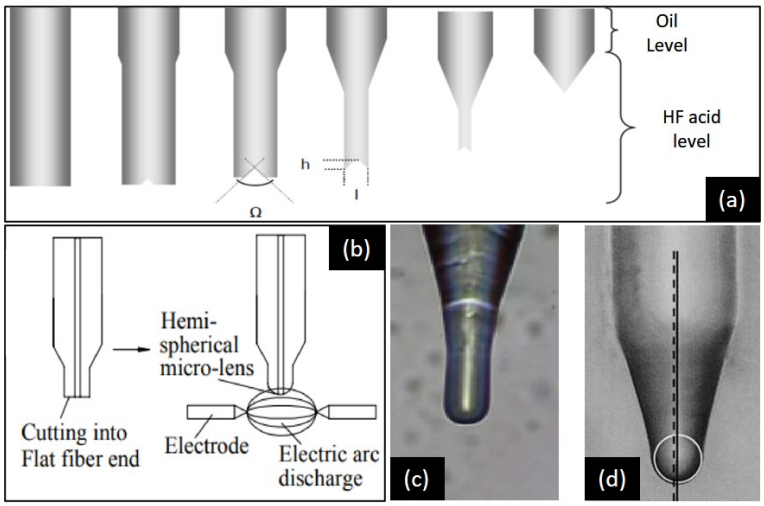

Figure 1.22: (a) Schematic representation of the transformation stages of the end of a silica optical fibre dipped in HF acid. (b) Etching process interrupted before final stage at the desired diameter. Fiber is then cleaved and its tip is melted by electric arc. (c) Resulting fiber tip from process in (b). (d) Electric arc applied on a fiber after the final stage of HF etching [91].

Huo Xin et al. and Huei-Min Yang et al. have demonstrated hybrid methods that links etching and fusion by thermal melting or electric arc discharge [91, 92]. Figure 1.22 show the micro-lenses fabricated by these method. The radii of the presented lenses in (c) and (d) are 20 and 9 µm, respectively.

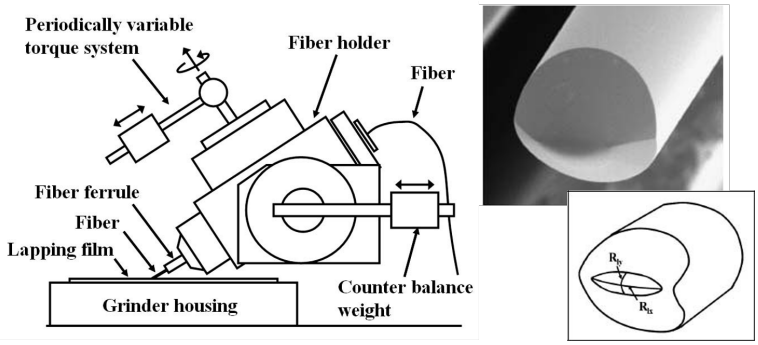

Figure 1.23: Fiber tip grinder scheme and a resulting elliptic-cone-shaped fiber tip [93].

1.2.1.6 Grinding

In 2007, Yu-Kuan Lu et al. utilized a modified fiber polisher to grind the tip of a single-mode (SM) optical fiber and create an elliptic-cone-shaped end-face. The grinding machine and the fabricated fiber tip can be seen in Figure 1.23. The grinding process involves different speeds along the X and Y axes, with the fiber held at gradually increasing angles when shaping the areas close to the fiber core. The material removal rate depends on the pressing force and the relative velocity between the grinding film and the fiber [93]. While this technique allows for the creation of various lens shapes, it can be particularly challenging when attempting to achieve high curvature surfaces, especially for SM fibers.

More recently, in 2021, N. Boulaiche et al. [94] introduced a simplified method for fabricating hemi-elliptical shaped fiber tips for single-mode (SM) fibers. This method combines the micromachining by polishing technique with the use of a polymer droplet. To create the hemi-elliptical micro-lens design, the fiber is polished at different speeds along its X and Y axes at a fixed angle. Once the desired ellipticity is achieved, a polymer droplet is carefully applied to the elliptical fiber tip using a micro syringe. The surface tension forces naturally shape the droplet into a hemi-elliptical form. The polymer is then cured to strengthen its bond to the fiber.

The significance of this approach lies in its ability to simplify the fabrication process of hemi-elliptical micro-lenses on SM fibers. Furthermore, Boulaiche et al. demonstrated that these micro-lenses effectively colimate and correct the beam divergence of laser diodes before the light is injected into the fiber core. This ensures improved coupling efficiency and better alignment between the laser diode and the fiber, resulting in enhanced performance and reduced losses.

1.2.1.7 Electrostatic pulling

Chun-Ching Wu et al. have demonstrated that the radius of curvature of micro-lenses made from SU-8 photoresist can be controlled by electrostatic pulling [95]. First, a thin layer of SU-8 is created on a glass substrate by spin coating. This layer is then soft baked. Afterwards, the fiber is perpendicularly set in contact by the tip with the SU-8 layer. When pulled up, the SU-8 takes a hemi-spherical shape due to surface tension forces. To increase the obtained radius of curvature, the fiber is set between two charged plates generating an electric field parallel to the fiber. The resulting electrostatic force between the droplet and the charged plates deforms the

droplet shape. The obtained radius of curvature is inversely proportional to intensity of the electric field. Figure 1.24 shows a before and after of an electrostatically pulled SU-8 micro-lens. Finally, the micro-lens is exposed to UV light and hard baking to fully polymerize.

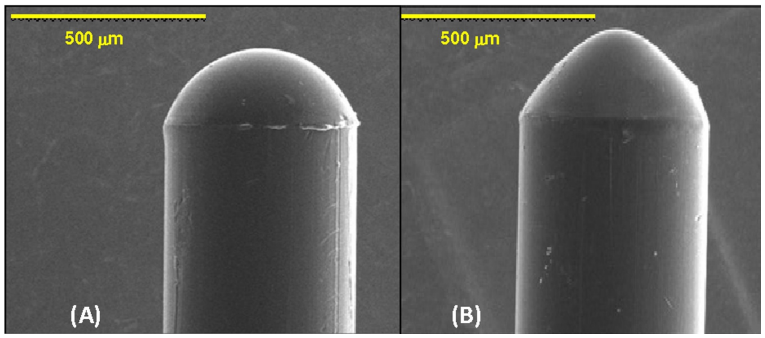

Figure 1.24: (A) Before and (B) after electrostatic pulling of a SU-8 micro-lens [95].

1.2.1.8 Other less-implemented noteworthy techniques

Aside from focused ion beam (FIB) milling, nanoimprint lithography (NIL) which are generally used for the fabrication of diffractive and resonant lenses (more about them in the next two sections), there are a few other less-implemented but noteworthy techniques such as:

- Silica micro bead mounting in etched fiber core (figure 1.25 (a)) [96].
- NOA61 micro-lens in etched fiber core, with controlled wettability to control lens radius of curvature (figure 1.25 (b)) [97].

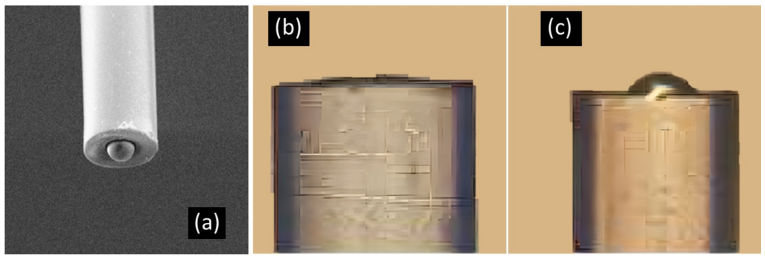

Figure 1.25: (a) Scanning electron microscope of a micro-bead attached to etched fiber core. (b) and (c) are the shape of an NOA61 droplet on the end-face of a fiber with and without hydrophobic treatment, respectively [96, 97].

1.2.2 Diffractive micro-lenses

Diffractive lenses have emerged as promising alternatives to traditional refractive lenses in a wide range of applications, including imaging, sensing, and communication [65]. These lenses work on the basis of interferences of light diffracted through a

series of micro-structures, such as gratings (notably Fresnel zone plates and Fresnel phase plates) or phase-shift structures/diffractive optical elements [98, 99], rather than refracting light as in traditional lenses. This allows diffractive lenses to achieve high levels of control over the phase and amplitude of light, which can result in increased signal-to-noise ratios in sensing applications, and enhanced light coupling efficiency in communication systems [100]. Moreover, beams such as doughnut and top-hat have been successfully achieved by Timo Gissibl et al. [101].

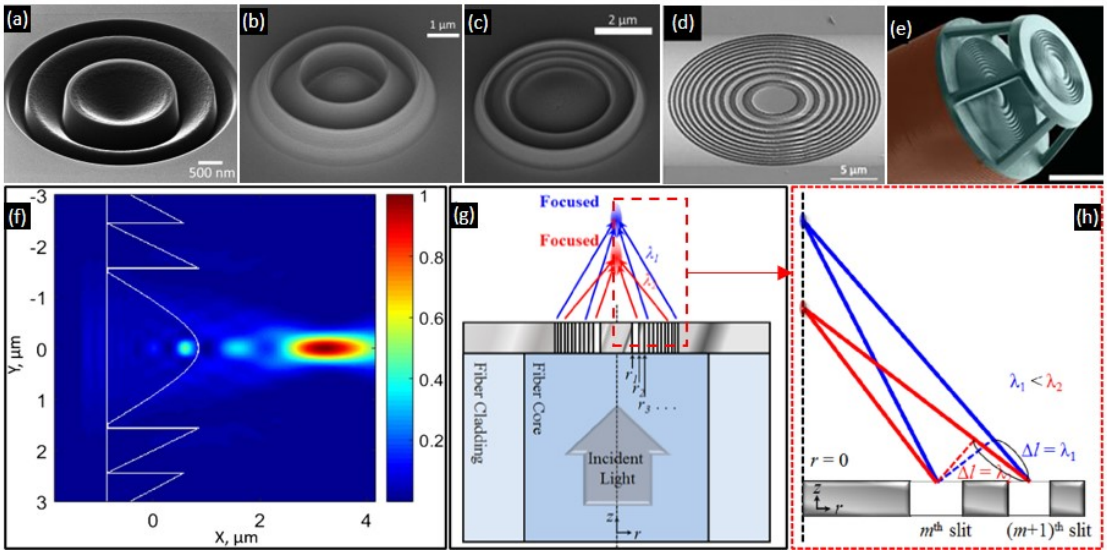

Figure 1.26: (a) Mold used for the fabrication of the diffractive lens shown in (b) by NIL. (c) Fresnel lens on SM fiber core. (d) Fresnel zone plate realized by ion beam milling. (e) Fresnel lens (f) Comsol simulation of light focusing through the Fresnel lens shown in (c). (g) and (h) Schematic representation of the working principle of a Fresnel zone plate and its response to different wavelengths [98, 99].

These microstructures are typically patterned onto a substrate using lithography techniques such as two-photon lithography [102] (already explained in section1.2.1.1), electron beam lithography (EBL) [103], nano-imprint lithography [99] or focused ion beam (FIB) milling [61].

Electron beam lithography (EBL) shares a lot of similarities with photolithography as they both aim to cure or harden a resist by beam exposure. EBL however, has a much higher resolution (sub 10 nm [104]) due to the much smaller wavelength of electrons (few picometers vs hundreds of nanometers for light). The high resolution comes at the price of being extremely slow (low throughput), limiting EBL applications to photo-masks or molds fabrication (such as the ones used in nano-imprint lithography [105]) research and development and low-volume production.

Nano-imprint lithography (NIL) is the process for fabricating nano-scale patterns in a material or substrate, which will be later used to imprint/stamp the negative of the created pattern onto the desired surface. Materials such as monomers and polymers that can be cured thermally or by UV are often used for the imprint [106].

NIL has a high throughput, high resolution, and leads to significant cost reduction when compared to other lithography methods.

Focused ion beam (FIB) milling is the process for selectively etching or sputtering, in a vacuum environment, very small chunks of a substrate under the effect of a focused beam of high energy ions, such as gallium or argon. The resolution of this technique is of the order of a few nano-meters and its etching rate is related to the ion beam diameter, acceleration voltage, and current.

Examples of diffractive lenses and the focusing mechanism of light upon interaction with such structures are represented in figure 1.26.

Despite their potential advantages, diffractive lenses are still subject to a number of technical challenges, including limitations in the size and operating bandwidth of the lenses, sensitivity to environmental conditions such as temperature and humidity, as well as issues related to the design and fabrication of the microstructures that make up the lenses [65, 107].

1.2.3 Resonant micro-lenses

Resonant lenses, also known as fiber meta-tip (FMT), are a type of diffractive lens that operate based on the principles of resonant light-matter interactions. These lenses are made up of arrays of subwavelength resonators, which are structures that can be resonant at specific frequencies. By carefully engineering the resonators, resonant lenses can be designed to diffract and manipulate light in specific ways, such as focusing, collimating, and vortex generation with high efficiency and resolution [108]. Resonant lenses have potential applications in areas such as microscopy, lithography, quantum technologies [109], and sensing, alsot where high-resolution optical imaging and manipulation is required [110, 111].

The design of resonant lenses involves the engineering of sub-wavelength resonators that are typically made up of periodically arranged array of nanoscale metal or dielectric structures, such as nanoparticles or nanorods. To simulate and optimize the response of the meta-elements, FDTD simulation tool is used [112, 113]. The spacing and size of the resonators, as well as their material properties, can be tuned to create a resonant structure that can interact strongly with specific wavelengths of light.

Figure 1.27 show electron scanning microscope images and illustrations of the structure of fiber meta-tips as well as experimental results on the generation of collimated and vortex beams. Meta-lenses are mostly created on large mode area (LMA) fibers (core diameter around 25 µm) instead of SM fibers (core diameter around 9 µm), to increase the number of unit meta-elements inscribed on the fiber core, hence increasing the efficiency of the lens. Ideally, to ensure that a LMA fiber is SM at a wide spectrum range, endlessly SM, photonic crystal fiber (PCF) is used [60]. The same is applicable for diffractive lenses as well.

Just as for diffractive lenses, the fabrication of resonant lenses also involves techniques such as EBL, NIL, and FIB milling.

The fabrication process or resonant micro-lenses can be complex and time-consuming, as it involves creating highly ordered arrays of subwavelength structures

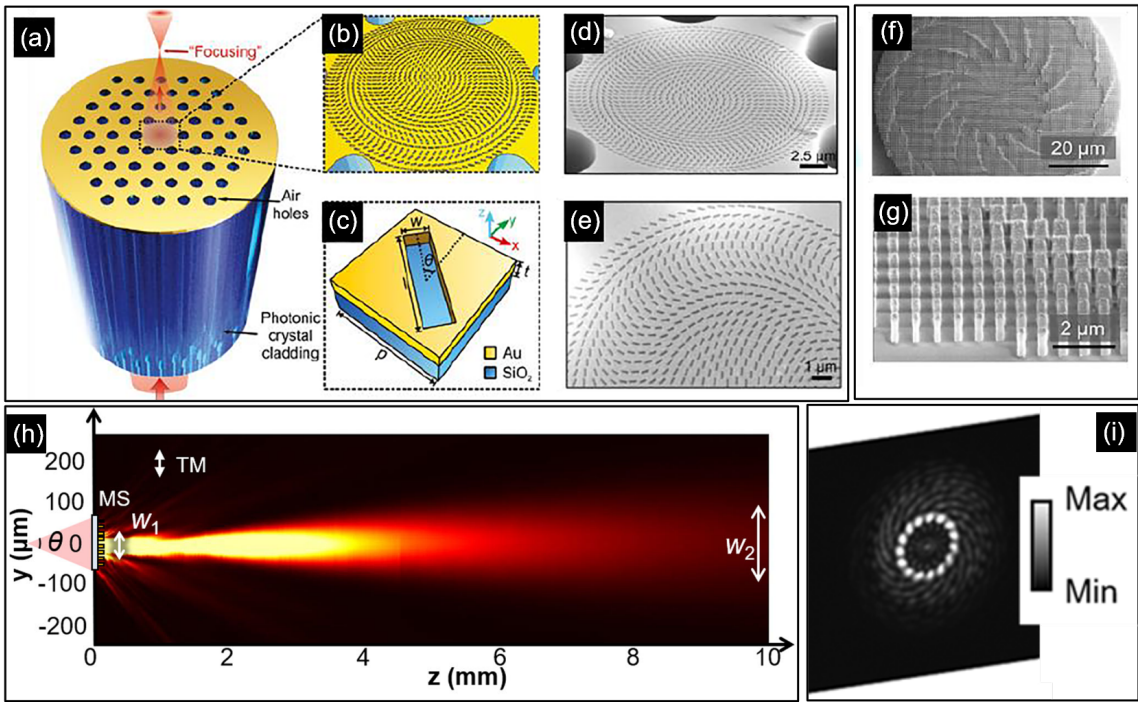

Figure 1.27: (a) Photonic crystal few mode optical fiber with 40 nm gold layer where metalens is inscrivbed by FIB. (b) and (c) show the schematic of the meta-lens design. (d) and (e) are SEM images of fabricated meta-lenses designed to obtain focal lengths of 30 µm and 50 µm with NAs of 0.37 and 0.23, respectively, at an operating wavelength of 1550 nm. (f) and (g) are SEM images at different scales of a meta-lens that serves as vortex beam generator for a SM fiber with beam expander/spacer; Resulting vortex beam is shown in (i). (h) beam collimation achieved using a meta-lens inscribed on SM fiber spacer [13, 108].

with nanometer-scale precision. In some cases, additional processing steps such as metal deposition, plasma etching and beam expansion may be required to create the desired resonant structures.

1.3 Fabrication techniques for Hollow-Core fibers

HCFs, are a particular type of photonic crystal fibers (PCF). They offer unique properties due to their structure, which comprises a hollow core surrounded by a photonic crystal lattice. The latter is a periodic arrangement of dielectric materials with a periodic variation in the refractive index. In the case of HCF, this periodic variation is typically achieved by creating an array of air holes or voids within a solid transparent material. The lattice structure of the photonic crystal creates a bandgap, also known as the photonic bandgap, which is a range of free space wavelengths or frequencies where the propagation of light is forbidden. This bandgap arises due to the interference between the incident light and the reflected and refracted waves at the interfaces of the periodic structure. The bandgap in a HCF acts as a mirror, preventing the propagation of light within certain wavelength ranges. There are typically wavelength ranges where the bandgap does not exist or is minimal, allowing light to propagate. This range is known as the photonic bandgap's

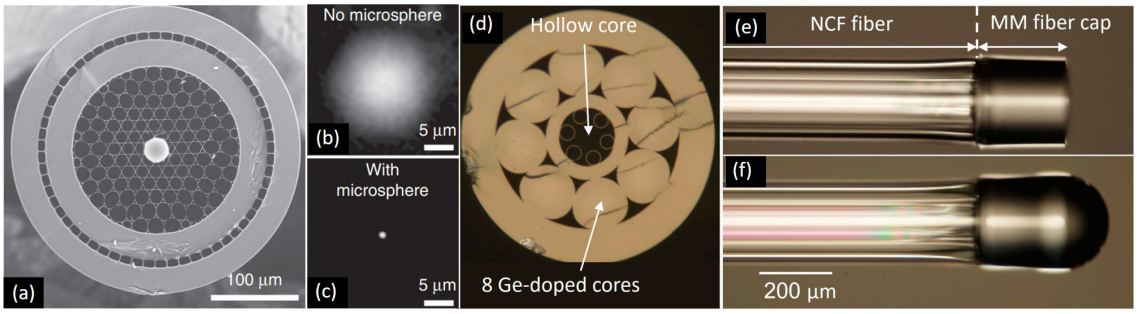

Figure 1.28: (a) silica micro-bead inserted in hollow-core fiber tip (b) and (c) show the difference in beam diameter before and after inserting the micro-bead, respectively [114]. (d) Image of a HCF inner structure (e) Capping the fiber with a MM fiber to block the holes and make it possible to use the fiber in immersion applications. (f) Fiber tip curved by electric arcing [115].

"transmission window." By carefully engineering the size, shape, and spacing of the air holes in the photonic crystal lattice, the transmission window can be tailored to specific wavelengths of interest [116].

By confining light within the hollow core, these fibers can effectively overcome limitations of conventional solid-core fibers, such as high nonlinearity and dispersion. [117, 118]

HCFs have found diverse applications across various scientific and technological domains. In the field of telecommunications [119], these fibers offer low-loss transmission capabilities and higher group velocities [120], enabling the development of high-capacity data transfer systems. They also provide exceptional control over the dispersion properties, making them well-suited for dispersion compensation in optical networks. Moreover, HCFs have proven to be highly efficient for high power processes, facilitating the development of ultra-fast lasers [121]. Additionally, they have demonstrated their utility in gas sensing [122, 123], where the hollow core can be filled with a target gas, resulting in enhanced light-gas interaction and improved sensitivity [124, 125].

1.3.1 Splicing of solid core fiber and shaping by electric a rc discharge

The process of shaping the tip of HCF is a delicate task because there is a risk of collapsing the inner crystal-like lattice, which can significantly degrade the fiber's performance if the heat or an electric atc is applied. H. Gong et al. reported a 30dB insertion loss caused by air hole collapse and power leakages [126]. To avoid this issue, DJJ. Hu et al. and HI. Stawska et al. [127, 128] successfully spliced a MM fiber to a HCF without damaging the inner structure and with minimal loss (approximately 0.32 dB). They achieved this by slightly offsetting the HCF position during the splicing procedure, shielding it from excess heat. Furthermore, parameters like the arc duration and maximum current were optimized [129]. Splicing an MM fiber to the HCF, as shown in Figure 1.28 (e), enables the creation of a shaped tip through

electric arc. HI. Stawska et al. [128] utilized this type of fiber tip to benefit from HCF's low dispersion in multi-photon sensing applications using femtosecond lasers, allowing them to focus the beam at a WD of 180 µm. The fabricated shaped HCF tip resembles the one represented in figure 1.28 (f). Additionally, K. Milenko et al. [115] employed a similar fiber configuration to achieve high signal-to-noise ratio Raman spectroscopy. By replacing conventional fibers with HCFs and incorporating small MM curved fiber tips, they significantly reduced the unwanted silica response, which is important in Raman spectroscopy since silica has a strong Raman peak at around 440 $cm^{-}1$ which intensity is proportionally linked to the fiber length. The curved fiber tip of course contributed to increasing the beam's intensity density, and therefore enhancing the Raman signal from the sample.

1.3.2 Micro-sphere insertion in hollow-core

Another method to equip an HCF with a micro-lens was demonstrated by A. Lombardini et al. [114]. They inserted a micro-sphere with the same diameter as that of the HCF's core. The fabricated fiber is shown in Figure 1.28 (a), and the outgoing beam characterization before and after installing the micro-lens is shown in Figures 1.28 (b) and (c), respectively. Clearly, the micro-lens contributed to a significant increase in beam density, and the device was used for high-resolution Raman endoscopy. Similarly, A. Kudlinski [130] employed a similar approach with a double-cladding anti-resonant HCF for nonlinear micro-endoscopy.

Therefore, in immersion applications, MM fiber splicing is preferred over HCF lensing methods, as the spliced MM fiber also acts as a protective cap, preventing the filling of photonic crystal air holes by the liquid through capillarity.

1.4 Lens fabrication techniques for multi-core fibers

MCFs are currently gaining a lot of attention as researchers are exploring their potential applications in various fields, including data communications, fibre lasers, and sensors. Compared to free space optics, the use of fibres offers benefits such as flexibility, integration, and compactness. In multi-beam applications, MCF outperform fibre bundles due to their increased stability, where each core is exposed to the same environmental changes, such as vibrations, temperature, and pressure. Additionally, MCF are more compact compared to fibre bundles, and the core separations throughout the fibre remain constant, making them more easily repeatable than fibre bundles that involve inserting multiple single-core fibres into a capillary [131].

Lensing MCF has proven to add even more functionalities by giving more control over the light emerging or going into the cores of the fiber in applications such as three dimensional and multi-point two dimensional optical trapping [132–135], beam scanning for medical imaging [136], light coupling between silicon photonic chips and MCF [137].

The most prominent techniques implemented in the fabrication of micro-lenses for MCF are two-photon lithography and photopolymerization. In the case of MCF

these techniques have only been used to make resonant lenses and not diffractive lenses, unlike single-core fibers.

1.4.1 Two Photon Lithography/ 3D printing

In 2013, C. Liberale et al, were the first to fabricate micro-prisms on each of the cores of a four cores fiber by two photon lithography. The prisms reflect the light coming from the fiber cores to meet in one single point on the axis that goes through the fiber center, as shown in figure 1.29 (a). This configuration was used to achieve three dimensional trapping of single cell (figure 1.29 (b)) as well as its Raman spectroscopic measurement [133].

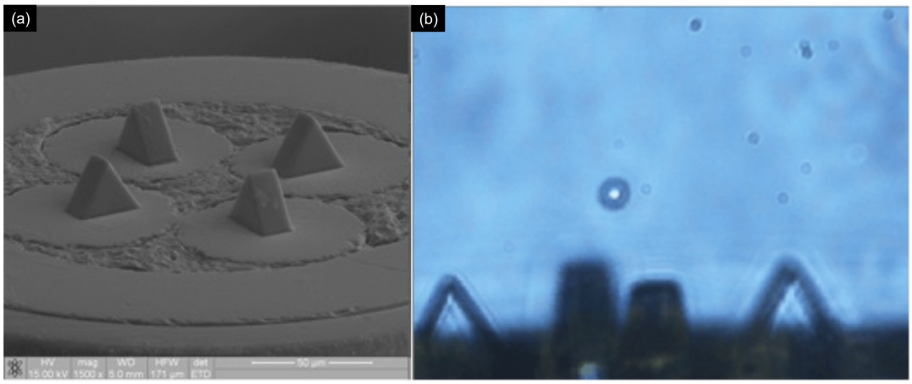

Figure 1.29: (a) Micro-prisms completely covering the cores, fabricated by two photon lithography. (b) Three dimensional trapping of a red blood cell. [133]

P.I. Dietrich et al. later, in 2017, 3D printed by two-photon lithography a micro-lens array to optimize the coupling of light between a Gaussian beam and the individual cores of a hexagonal 7-core fiber. In addition, the fabricated design allowed to precisely detect the position of the incident beam without the need for an imaging system. That is achieved by monitoring the coupling into the cores [138].

A third application of lensed MCF by 3D printing was reported in 2021 by S. Sivankutty et al. [136]. The aim was to develop MCF-based endoscopy. The design consisted of a micro-lens with a 14 µm radius of curvature on top of each core of the 120 cores of the MCF, and 100 µm above this, a lens with the same diameter as the fiber and a 400 µm curvature radius. The micro-lenses on the cores act as beam collimator, and then the lens that has the diameter of the fiber focuses the 120 beams of light into one single point. The injection of light into this fiber was performed using a spatial light modulator (SLM), which means that by introducing a phase term to the used phase map, the generated beam can be scanned laterally and axially [139]. An image of the fabricated MCF tip is shown in figure 1.30 in addition to the achieved lateral scanning results.

1.4.2 Photopolymerization

As seen for single-core fibers, photopolymerization of a UV curable resin can lead to micro-lenses on the core of fibers. These lenses are usually used to enhance the coupling from laser diodes into the fiber. In the case of MCF, recently, Y. Kamiura et al. demonstrated that this technique can be scaled up to multiple cores and that

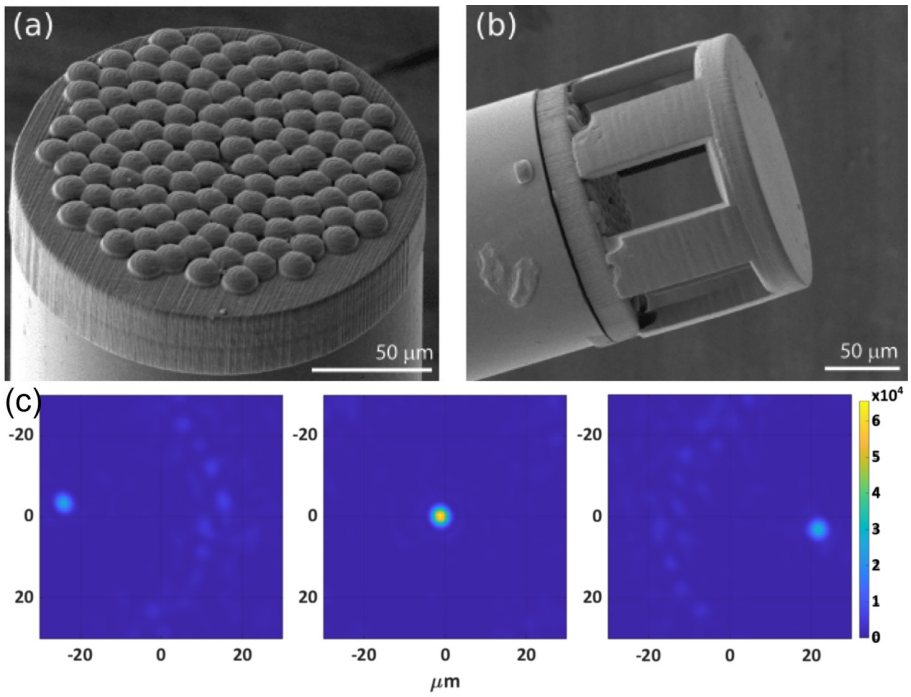

Figure 1.30: MCF lenses. (a) 120 micro-lens acting as beam collimator. (b) The fully printed fiber tip. (c) Achieved lateral beam scanning. [136]

this could be used to simultaneously couple multiple silicon photonic chips to MCF [137], allowing for a much greater transfer of data. Their design consists of two parts: the pillar and the micro-lens. The first step of the fabrication procedure is the dipping of the MCF in a thin layer of UV curable resin that is deposited on a glass slide. The thickness of the resin layer is chosen to be equal to micro-lens pillar desired height. When the fiber is in contact with the resin, UV light is injected into the fiber causing the exposed resin to harden. The uncured resin is later rinsed off leaving a micro-pillar on top of each core. Afterwards, the pillars tips are set in contact again with the UV resin. Surface tension forces will give the newly deposited resin a hemi-spherical shape. Finally, UV is injected again into the fiber to cure the entire pillar + micro-lens structure. The procedure is illustrated in figure 1.31

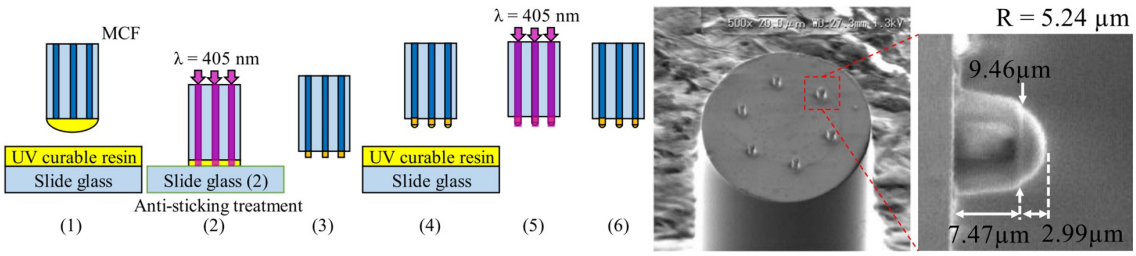

Figure 1.31: Illustration of photopolymerization procedure of MCF micro-lenses and scanning electron image of the resulting MCF tip. [137]

An important experimental observation made by Yoshiki Kamiura et al. was the appearance of higher order modes when the micro-pillar length exceeds 10 µm. These modes are a result of guiding light in a polymer-air cylindrical waveguide. In

such a waveguide, since the index difference is very important ($\geq 30\%$), the number of modes that can exist is much higher than 1. Therefore, the micro-pillar or micro-lens height must remain restrained to a few micro meters when a SM behavior is needed.

1.5 Conclusion

In this chapter, the state of the art of fiber micro-lenses has been explored. The fabrication techniques have been divided into three main categories based on their operating principles (refraction, diffraction and resonance). Diffractive and resonant micro-lenses are considered from a theoretical point of view superior to refractive ones due to the higher number of degrees of freedom and the possibility of creating structures that shape vector beams. With this, it becomes possible to generate beams that were previously unattainable using refractive micro-lenses. However, a major obstacle to implementing diffractive and resonant micro-lens technologies in the market is that they are still new and immature, lacking sufficient development and refinement.

The additional cost and difficulties in fabrication, means that these techniques may not completely replace refractive micro-lenses but expand on them. This is also the case of the various available fabrication techniques of refractive micro-lenses. Each has its advantages and limitations, and sometimes one is better suited than the other depending on the application and fiber type. Figure 1.32 puts in perspective the difference between the three micro-lens categories and Table 1.2 is a summary of the drawbacks of the different major refractive micro-lens fabrication techniques.

An important point which is one of the novelties of the work addressed in this PhD thesis is that most of the mentioned techniques have not been tested on non-silica based fibers such as mid infra-red fibers, in our case: fluoride based fibers. Since these fibers are so much more fragile and have different properties than silica fibers [140], most techniques, especially the ones that rely on grinding, heating, splicing and laser machining are incompatible with this kind of fibers. Our developed technique may solve this issue as shown in upcoming sections of the manuscript, especially in section 4.1.

Table 1.2: **Refractive micro-lens fabrication techniques with their respective limitations. (* indicates: incompatible with mid-IR fibers)**

Technique	**Main Drawbacks**
Thermoforming by electric arc*	- Lead to low curvature micro-lenses
Melting and drawing*	- Hard to control lens shape
Silica micro-bead splicing* [140]	- Difficult to align bead with the fiber core
Two photon lithography; FIB; Femtosecond laser machining [133]	- Long processes - Not adapted for large scale production - Costly and require sophisticated tools and systems

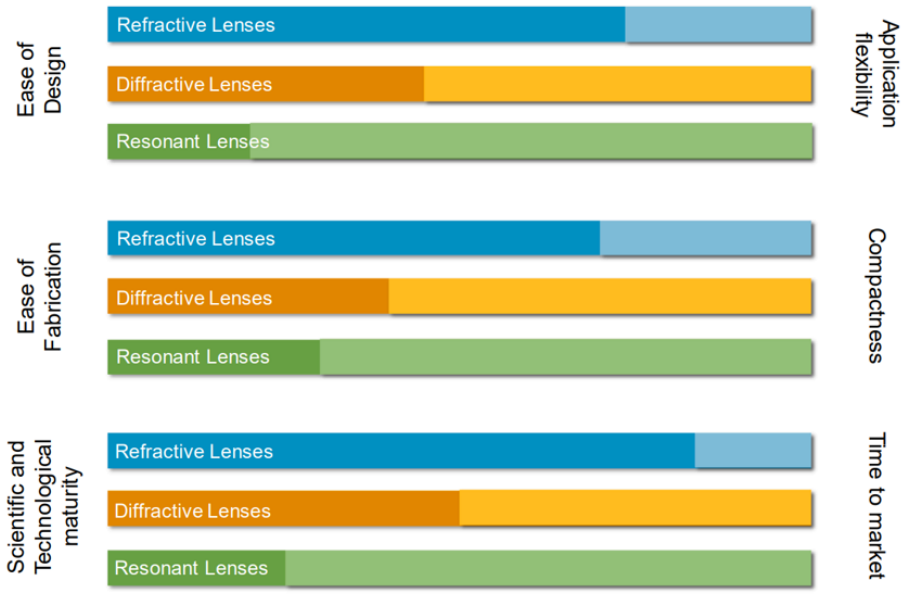

Figure 1.32: Comparison between refractive, diffractive and resonant micro-lenses[65]

Moreover, in this chapter, we have explored two key techniques of the state of the art for enhancing the functionality of HCFs. The first technique involves splicing MM fibers to HCFs, enabling the creation of shaped tips without damaging the inner photonic crystal lattice. This technique has contributed to applications such as multi-photon sensing and Raman spectroscopy, leveraging the low dispersion and reduced silica response of HCFs. The second technique involves equipping HCFs with a micro-sphere.

Finally, the fabrication techniques for MCFs developed to date have been presented. The two most prominent techniques are photopolymerization and two photon lithography. The applications that benefit from lensed MCFs are 3D or multi-point 2D optical trapping and sensing, beam scanning and, and light coupling enhancement between multiple light emitting silicon photonic chips and MCF allowing for a greater broadband transfers in telecommunication.

The next chapter will cover the technique developed by our laboratory in collaboration with the University of Sétif 1.

Chapter 2

Molded polymer fabrication technique

The previous chapter introduced most of the fiber micro-lens fabrication methodologies, and show that there is still a need for a fabrication technique that would be affordable, easy to design and manufacture at an industrial scale, while also being compatible with 1- high curvature microlens; 2- Singlemode (SM) as well as with multimode (MM) fibers; 3- Multicore fiber (MCFs); 4- Hollow core fiber (HCFs), 5- non-silica based fibers, as MIR fibers where no evidence exist for such lensed fibers.

To address this, our team (ICube-IPP) in collaboration with the University of Setif - Algeria, have developed and patented before my PhD a new technique based on polymer molding. The technique is detailed in this chapter. During my PhD and based on the previous experiences, I have rebuilt from scratch the setup to fabricate this micro-lens. In this chapter, we will first consider the case of usual silica single core fiber and then the one of micro structured fibers and multicore fibers. For silica single core fiber, the ability to achieve micro-lenses was already demonstrated in the context of the collaboration between Sétif and Strasbourg Universities. During my PhD, I have improved the robustness, tried to optimize the fabrication parameters and I have achieved rigorous characterizations of the lenses. The results concerning non silica fiber and micro-structured fiber are completely new.

The fabrication process on single core silica fiber has been described in detail in our published article [141]. The first part of this chapter will be based on it.

2.1 On Single-core fibers

The fabrication process consists of three major steps. The first is the creation of a mold that will determine the shape and dimensions of our lens. The mold is also created in an optical fiber end. This fiber will be called the mold fiber. The second step entails polymer preparation and mold filling. Finally, the third step concerns the deposition of the micro-lens on the target fiber.

2.1.1 Mold fabrication and lens shape control

For the mold fabrication, a fluoridric acid (HF) wet chemical etching of the mold fiber flat tip is employed. As described in section 1.2.1.5, the fiber core and the cladding are etched faster or slower depending on their dopant and dopant concentration. In the case of Boron (B_2O_3) doped silica, the etching rate decreases, contrary to when the dopant is germanium or fluorine [142]. The dissolution rate of germanium doped silica is higher than pure silica due to lower energy bonds between Ge-O (662 KJ/mol) versus those of Si-O (799 KJ/mol) [143]. In our study, only germanium doped fiber cores are used. A graded index optical fiber has a parabolic index profile (as shown in figure 2.1), its core is usually germanium doped and its cladding is made of pure silica or Boron doped; both have a lower refractive index than germanium doped silica [144]. The index profile of the core is an indirect representation of the radial germanium concentration; it is highest in the center and gradually decreases towards the core-cladding interface [145, 146].

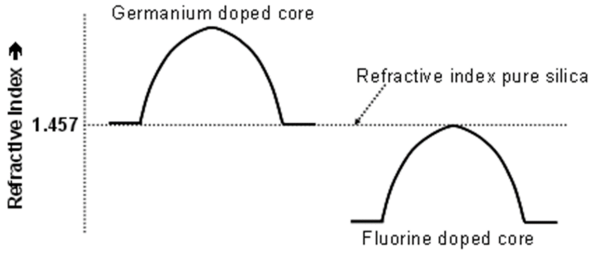

Figure 2.1: Index profile of a MM graded-index fiber doped with (left) germanium, (right) Fluorine. [145]

The doping profile is one of the parameters that could be controlled by the fiber manufacturers. In our technique, this is a degree of freedom exploited to control the curvature of the molds. The HF etching rate as function of dopant concentration in silica is described by the following non-linear relationship [147]:

$$\frac{dx}{dt} = k[C]^n$$

where x is the etched depth, $\frac{dx}{dt}$ is the etching rate, k is the reaction constant that changes depending on the dopant, $[C]$ is the dopant concentration, and n is the reaction order.

Step index fibers on the other hand, lead to molds with conical shapes as shown in figure 2.2 [148].

2.1.1.1 Controlling the mold depth/lens height

The mold fiber etching has been carried out in the ICube C3-Fab platform with the help of Stéphane Roques, engineer. The HF solution preparation, should be done under a well-ventilated fume cupboard using appropriate tools. In our case, all of are Teflon-protected. HF is a highly dangerous acid, which is why we prefer to reduce its concentration to 24% from the original 48% to lower the risks, even though this will result in slower etching rates. Temperature also plays a role determining the

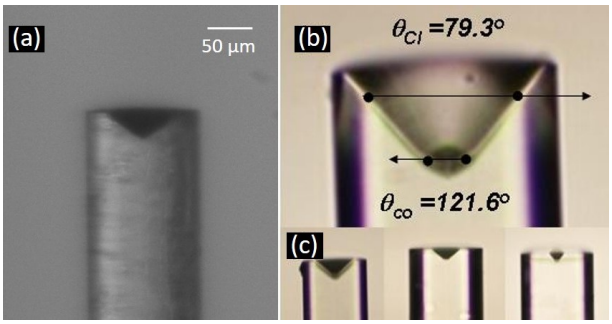

Figure 2.2: Conic molds etched in (a) 50/125 MM, (b)(c) SMF28 and SMF450 [148] step index fibers.

etching speed (Mandeep Kaur et al. [6] show that the etching rate almost doubles by going from 23 to 35°C). In our case, we work in a temperature controlled room (21-22°C). Figure 2.3 depicts the HF etching setup. The fiber is hung on a vertical support, with only around 500 μm of the tip submerged into the HF solution.

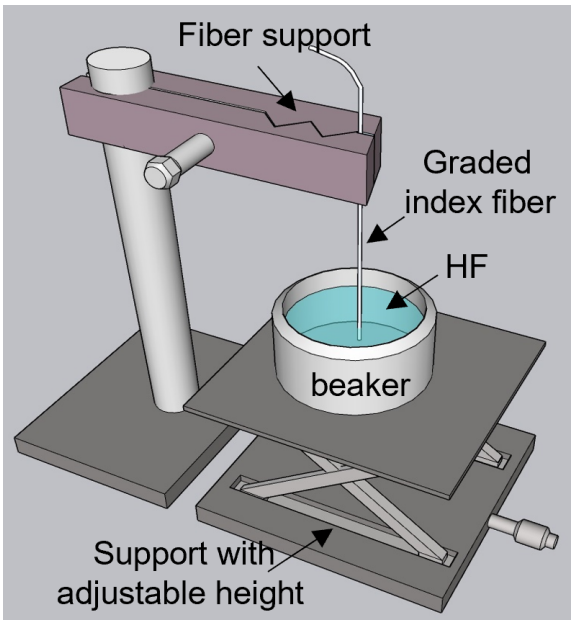

Figure 2.3: Scheme of fiber HF etching setup. Beaker is made of Teflon and the fiber support has a Teflon protective layer.

The lens height is related to the mold depth which depends on the time the fiber is kept in HF. However, since each graded index fiber has different characteristics, such as cut-off frequency, bandwidth and core size, the doping concentrations may vary. This is why the etching rates differ significantly between the various fibers. Determining the etching rates for a specific graded index fiber is straightforward. The relationship between etching time and mold depth is linear as shown in figure 2.3. This figure contains some of our etching results and others found in literature [143, 146]:
- Fiber GIF50C from Thorlabs, a MM fiber with a 50 µm core.
- Customized fiber from Phlam/Lille-France, a few modes fiber with 10 µm core.
Etching for both was performed with a 24% HF concentration at 21°C.
- Fiber GIF625, a MM fiber with a 62.5 µm core. The etching was done with a 48%

HF concentration (temperature unspecified).
- Nine-mode fiber (NMF at 1550 nm), with a core diameter of 33 µm. The etching was done with a 50% HF concentration at 25°C.

It is worth noting that during the etching process, both the core and cladding materials are affected, but the cladding is etched at a slower rate compared to the core. This difference constitutes the apparent cavity etching rate. It is crucial to halt the etching process once the desired depth of the mold is achieved. This is done by submerging the fiber in water, followed by rinsing with ethanol and isopropanol to eliminate any remaining traces of HF.

It is recommended to prepare a new HF solution after one or two hours, since the HF ion concentration drops due to the silica dissolution reactions. Figure 2.5 is a schematic illustration of the shaped mold after HF wet etching.

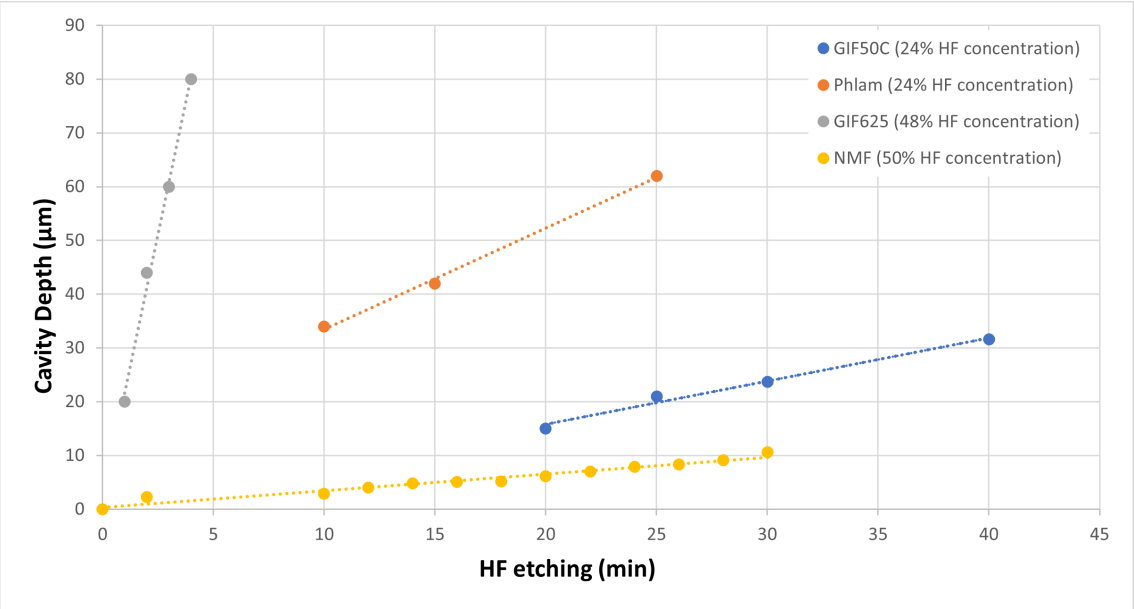

Figure 2.4: Mold depth evolution as a function of chemical etching time. Etching rates are: NMF = 0.37 µm/min ; GIF50C = 0.83 µm/min ; Phlam = 1.87 µm/min ; GIF625 = 20.3 µm/min.

It is possible to monitor the mold formation in real-time using the method presented in [149], by substituting the Teflon beaker with a transparent Polycarbonate (PC) or Polymethylmethacrylate (PMMA) beaker that is parallelepipedic in shape with straight edges. This ensures that there is no image distortion caused by the beaker's curvature.

2.1.1.2 Controlling mold diameter/lens base

The mold diameter depends on the fiber core diameter and on the etching time. For microlenses with diameter around 10 µm or smaller, single mode fiber may be used. However, these SM fibers are generally step indexed, therefore the etching step leads to conic shaped mold [150]. Not being able to find a graded index fiber with a small

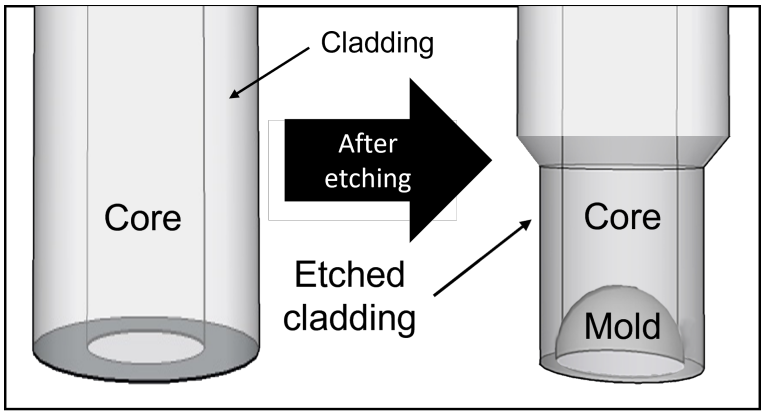

Figure 2.5: Schematic view of the mold in the fiber core after HF etching.

core diameter was an issue. A solution is melting and drawing (otherwise known as tapering) a graded index MM fiber to reduce its core to the required size. To do so, fiber glass processing devices such as the "Vytran" device from Thorlabs [151], or alternatively, a homemade setup (Pierre Pfeiffer in our team) such as the one represented in figure 2.6 (a) can be used.

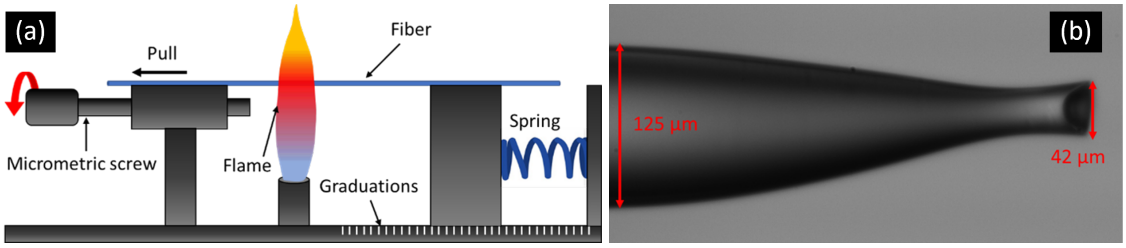

Figure 2.6: (a) Fiber melting and drawing setup. (b) 1.80 ± 0.05 mm stretched 50/125 slica fiber.

Tapering with the Vytran device is quite easy since everything is motorized and automated. Parameters such as filament temperature and tension exerted on the fiber will be automatically regulated depending on the input desired final fiber diameter. With the homemade setup, the fiber should be fixed on both sides of the apparatus. Next, the micro-metric screw is employed to pull the fiber and spring while exposing it to a flame of a temperature slightly higher than the silica softening point of 1650°C [152]. This causes the fiber elongation due to the applied spring tension. When the desired elongation is reached, the flame is stopped. The final diameter of the core is proportional to the initial pull applied. After elongation, the fiber is inspected using a microscope to identify the location where cleaving should be done to achieve the desired fiber diameter. The initial core/cladding ratio is preserved. Once the fiber is cleaved, it can then be etched using HF to produce the mold.

Figure 2.6 (b) shows an HF etched mold on a 1.80 ± 0.05 mm stretched fiber. Before etching, the fiber diameter at the tip was 49 μm, corresponding to a reduction by melting and drawing of the fiber diameter by a factor of 2.55, which means that, the 50 μm initial core was reduced to 19.6 μm. This reduction factor depends on the desired mold size. The desired mold/lens size is deduced from simulations (This is discussed in details in section 3.1).

2.1.2 Polymer preparation

The polymers used for the results presented in this work are: PDMS [153] and NOA61 [154]; But other polymers such as SU-8 and NOA170 have also been tested successfully. The list of compatible polymers may be extended to most of the transparent polymers curable thermally or by UV exposure. The choice of the polymer will depend on the application. Table **??** shows some of the main differences [155]:

Table 2.1: **Main differences between used polymers**

Polymer	PDMS	NOA61
Operating temperature (°C)	– 40 to 200	– 150 to 125
Refractive index at 632 nm	1.556	1.422
Ease of use	+	++
Bio-compatibility	+	- (But NOA86 is)
Hardness	-	+

Other key differences that dictate the choice are:

- Optical transparency;
- Fluence tolerance (More about these in section 4.2);
- Adhesion strength;
- Surface tension and gas permeability (this is an important factor for MCF micro-lens fabrication as later discussed in section 2.3).

To prepare PDMS, its resin and hardening agent (SYLGARD 184 Silicone Elastomer) are combined in a 10:1 ratio and mechanically mixed. The resulting mixture is then placed in a low vacuum chamber for approximately 15 minutes to eliminate any undesired air bubbles. On the other hand, NOA61 does not require any preparatory steps.

2.1.3 Micro-lens deposition

For the micro-lens deposition process, it is necessary to differentiate three different fibers. The first fiber (Fiber 1) is the one that will be equipped with the lens. The second fiber (Fiber 2) serves as mold. The third fiber (Fiber 3) is utilized as a flexible rod to introduce a droplet of the selected polymer into the mold.

After the polymer preparation, the Fiber 3 is immersed into it, and upon withdrawal, small droplets form as shown in figure 2.8 (a). The fiber is then attached on Mount 3, as illustrated in figure 2.7, between Fibers 1 and 2.

Next, the mold (Fiber 2) is gradually approached with a tilt angle from the droplet on Fiber 3 using the translation stage, as depicted in Figure 2.8 (a). Surface

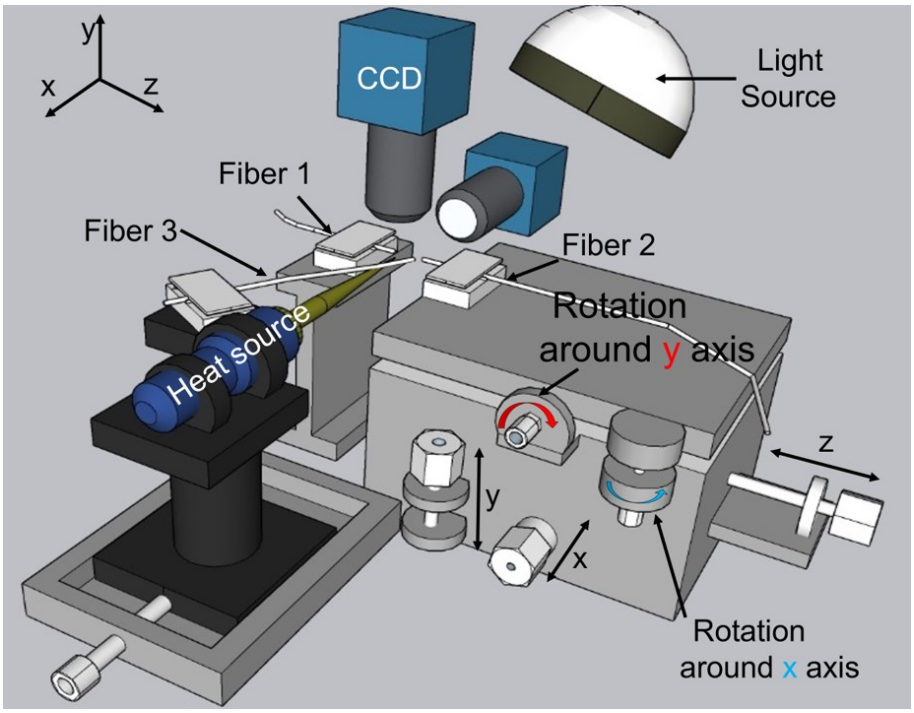

Figure 2.7: Schematic of the micro-lens fabrication setup. Fiber 1 is to be equipped with the lens, Fiber 2 holds the mold, and Fiber 3 brings the polymer droplets. Two CCD cameras are used for alignment monitoring.

tension forces draw the polymer into the mold once it contacts to the droplet. The angle serves the purpose of ensuring that an air bubble does not get trapped under the polymer inside the mold. This is not very important in the case of PDMS due to its ability to displace air bubbles (more information and a comparison between the ability to remove air bubbles between NOA and PDMS will be presented in section 2.3). In the case of mold overfilling, touching the polymer-free zone of Fiber 3 can be used to remove the polymer excess.

After filling the mold, the Fibers 1 and 2 are aligned and centered. Initially, the two fibers are pre-aligned in the both CCD camera planes (xz and yz) by utilizing the rotation degrees of freedom of the micro-positioning stage displayed in figure 2.7. Next, there are two ways to achieve final centering. The first approach involves optimizing light coupling between the two fibers. To accomplish this, light is injected in one fiber while the other is used to collect on a photodiode. When the fibers are perfectly centered and aligned, maximum light power is transmitted. This method is highly precise when the two fibers have comparable core diameters. However, if there is a significant difference in core diameter, the precision is lost. For instance, coupling from a 9/125 fiber (9 μm core) to a 50/125 fiber (50 μm core) can occur even if the fibers are not well-centered. Conversely, coupling from a 50 μm core diameter fiber to a 9μm core fiber is too weak to collect enough light for alignment. In this case, visual data provided by the two cameras is relied upon for alignment. The micro-positioning stage's degrees of freedom are used to align the fibers and bring them into contact, as shown in figure 2.8 (b) and (c). When the two fibers are in contact, the polymer is pre-cured.

To pre-cure the PDMS, a soldering iron is heated up to 200°C and brought below

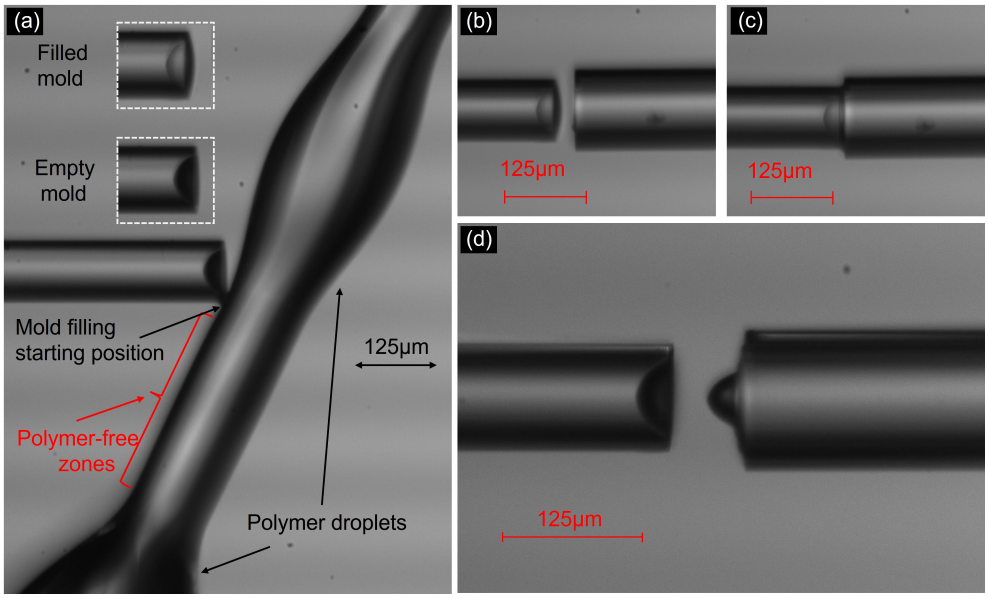

Figure 2.8: (a) Fiber 3 with polymer droplets to fill the mold. Top views: Photos of the mold before and after polymer filling by the droplets on fiber 3. (b) and (c) Fiber and mold alignment: pre and post contact. (d) Mold release. Micro-lens successfully deposited on Fiber 1.

the contact point of the two fibers for a duration denoted by **'t'**. The distance between the point of contact and the heating source should be approximately 100 to 125 µm, slightly less than a fiber diameter, as illustrated in figure 2.9 (a). This ensures good heat transfer to the polymer whilst also avoiding contact.
The pre-curing time **'t'** for PDMS is proportional to the mold volume, which is proportional to the mold etching time. The good PDMS pre-curing time empirically determined as a function of the mold etching time is shown in figure 2.9 (b). A significant dependency on room temperature has been observed.

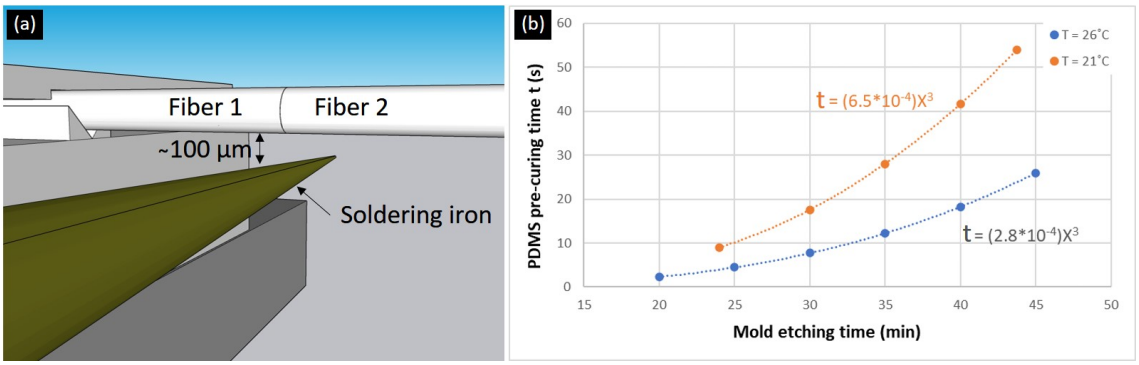

Figure 2.9: (a) Distance between fibers and the 200°C heating source (a soldering iron in our case) for PDMS micro-lens pre-curing. (b) PDMS pre-curing time as a function of mold etching time for a 50/125 GIF50C un-tapered fiber. Blue and orange curves represent pre-curing times obtained at 21 and 26°C room temperatures.

Finally, the mold is gently released (as in figure 2.8 (d)). If over-cured, the PDMS sticks to the mold. When under-cured, some polymer will stick to the fiber 1 and the rest remains in the mold. For a fully cured micro-lens, the fiber should

be left for 48 hours at room temperature or 10 minutes at 150 °C.

The NOA61 process is more straightforward, involving exposing the polymer to a $185mW/cm^2$ UV source for 10 seconds from any direction at a distance of approximately 1.5 cm from the fiber. This will cause the pre-curing of the polymer. The mold can then be released, and the micro-lens should be exposed to UV for 5 to 10 additional minutes for full curing.

The mold can be reused provided it is clean and in good condition. To clean the mold from NOA61, the fiber tip must be submerged in acetone overnight. With PDMS on the other hand, the mold should be immersed in isopropanol and exposed to ultrasonic vibrations for 30 min to an hour. These cleaning methods do not cause any damage to the mold and provides consistent results.

Figure 2.10 highlights the different shapes that can be manufactured using the presented technique. By comparing (a)(b) to (c)(d) the stark difference in possible lens size can be seen. However, when comparing (a) to (b) and (c) to (d), the effect of the mold fiber index gradient is put into perspective, because while the micro-lenses in question have nearly identical bases and heights, their radii of curvature differ greatly. More lens designs and their characterization will be discussed in chapter 3.

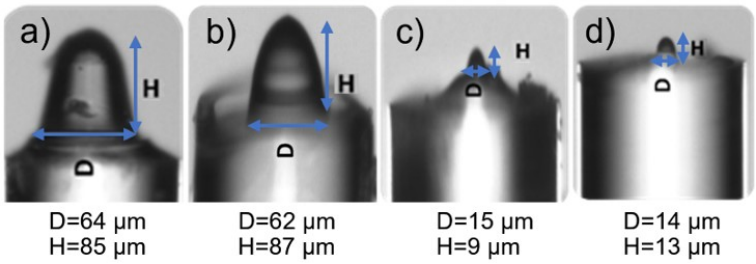

Figure 2.10: (a) and (b): High curvature PDMS micro-lenses with around 60 µm base fabricated on two 50/125 MM fibers; (c) and (d) two micro-lenses with around 15 µm base on SMF-28.

2.1.4 Spacer fabrication

In chapter 3, we will see that if a high curvature micro-lenses on a SM allow focusing on a one wavelength spot, one major issue is the extremely short working distance (WD). However, as Chung-Hao Tien et al. [81] demonstrated (results discussed in section 1.2.1.3), a spacer can be used to significantly increase this later. But for us, the goal is to not use splicing as this can be detrimental for some fibers such as Mid-IR and HCFs.
We have successfully been able to fabricate spacers also out of polymer with precise control over the spacer's length. The fabrication is carried out using the setup in figure 2.7 as well.

The first step of the fabrication is to prepare the fiber to be equipped with the spacer by properly cleaving its ends. Each end is then held by a fiber support. One end takes the place of Fiber 1 and the other that of Fiber 2 on the illustration. Now

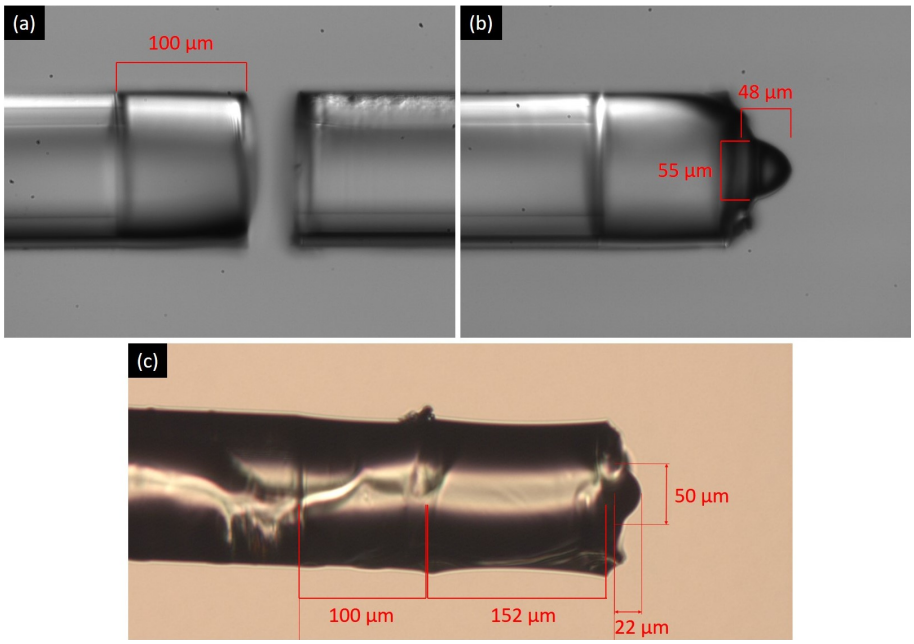

Figure 2.11: (a) Fiber ends separation leading to a 100 µm spacer. (b) Micro-lens deposited on the fabricated spacer. (c) 252 µm spacer made by performing the fabrication procedure twice; in addition to a micro-lens.

that both fiber ends are facing each other, a careful alignment must be performed. Then the two ends are separated by the required spacer distance. Afterwards, Fiber 3 with the polymer droplets is introduced in the gap between the two fiber ends. If the droplet is big enough to touch both ends simultaneously, pulling Fiber 3 back will leave the gap filled with a polymer cylinder. The final steps are pre-curing, separating the two fiber ends, then fully curing the polymer. During the separation, since the fiber ends have identical contact surfaces with the polymer, it is not possible to predict to which the spacer will remain attached. That is not an issue since both fiber ends are similar, making them indifferent. The fabrication procedure is depicted in figure 2.11.
This procedure works well for spacer lengths no longer than 200 µm. If longer lengths are needed, the procedure can be performed several times. In subsequent depositions, the polymer will always attach to the end with the spacer, since the polymer-to-polymer adhesion forces are greater than those of polymer to silica. Figure 2.11 (c) show a 252µm spacer made by repeating the procedure twice.
The micro-lens can, of course, be then deposited on the fabricated spacer as seen in figure 2.11 (b) and (c).

2.1.5 Micro-lens quality

2.1.5.1 Surface roughness and geometry

The lens surface roughness and geometrical symmetry are important parameters to consider since: a rough surface causes light scattering and signal losses, while a non-symmetrical lens may cause beam deflection and aberrations as astigmatism. The micro-lens surface roughness and geometry can be characterized using techniques such as scanning electron microscopy (SEM) and optical profilometry. It is worth

mentioning that in our case, studying the mold or the micro-lens quality comes back to the same thing, as the micro-lens is produced by molding.

We have tried to use an interferometric profilometer from ZYGO corporation, based on a Mirau objective. However, due to the very weak return signal caused by the micro-lens's curvature, the measurements led to inconclusive results. The fringes were almost undetectable over the entire micro-lens surface, as light was being reflected away from the optical axis of the interferometric Mirau objective. The same difficulties were encountered on the shallow mold cavities. We were only able to measure the micro-lens or mold height and base diameter which is delimited by the cladding's flat surface, as shown in figure 2.12.

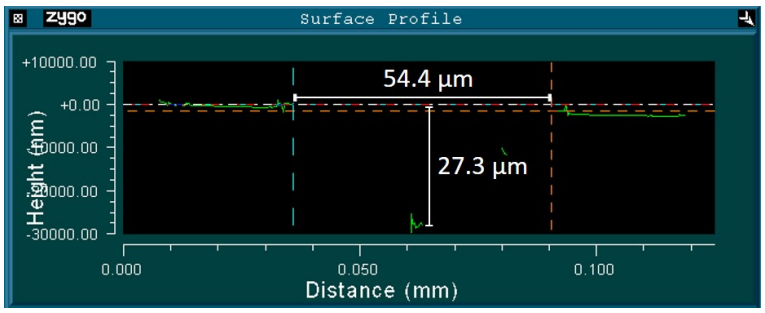

Figure 2.12: Interferometer profilometry measurement of a mold etched in a 50 µm core graded index optical fiber. Information on surface roughness and radius of curvature cannot be deduced.

On the other hand, Kanglin Li et al. [146] with their three-dimensional optical microscope, have managed to measure the mold profile of two fibers. The first is a nine-mode fiber, and the second is a MM fiber with 33 µm and 50 µm core diameters, respectively. The profiles are shown in figure 2.13. What can be concluded from their measurement is that the mold's smoothness indeed varies from one graded index fiber to another, and that the cleave angle of the fiber facet can greatly affect the final geometrical symmetry of the mold.

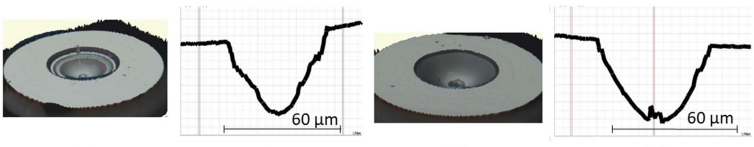

Figure 2.13: (a) and (c) are the microscope images of the molds in a nine-mode and mutli-mode fibers, respectively. (b) and (d) are their respective profiles taken along their height cross sections [146].

Since our ZYGO profilometer measurements did not give clear pictures of the quality of our fabricated micro-lenses, we have used a scanning electron microscopy (SEM). Figure 2.14 shown one of our fabricated NOA61 micro-lenses. The surface roughness appears to be very low, and no imperfection such as what Kanglin Li et al. presented is visible. This may be due to the graded index fiber in which we etched our molds, is of superior quality. Another hypothesis is that the defects

visible on optical profilometry measurements (figure 2.13) would be measurement artefacts. A ring of polymer can also be seen at the edges of the fiber. This is created during the fabrication process. The excess of polymer in the mold may find its way to the edges when pressing the two fibers (Fiber 1 and Fiber 2 in figure 2.7) together. Nevertheless, this will not have any impact on the micro-lens's or fiber's performance, as this part is far from the core and does not interact with light.

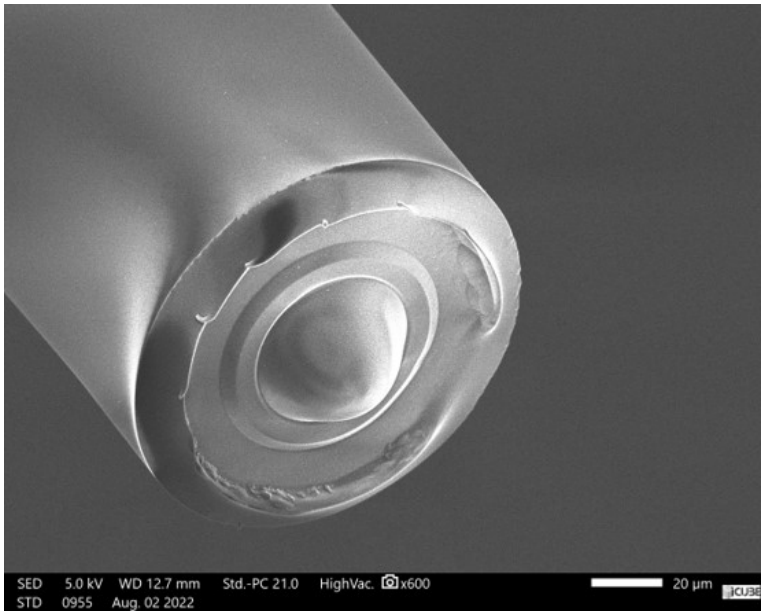

Figure 2.14: SEM image of a NOA61 micro-lens; The lens show a very low surface roughness, and almost no imperfections in its geometry. The ring at the fiber edge is due to the overflow of polymer during the fabrication process.

2.1.5.2 Durability, thermal cycling test

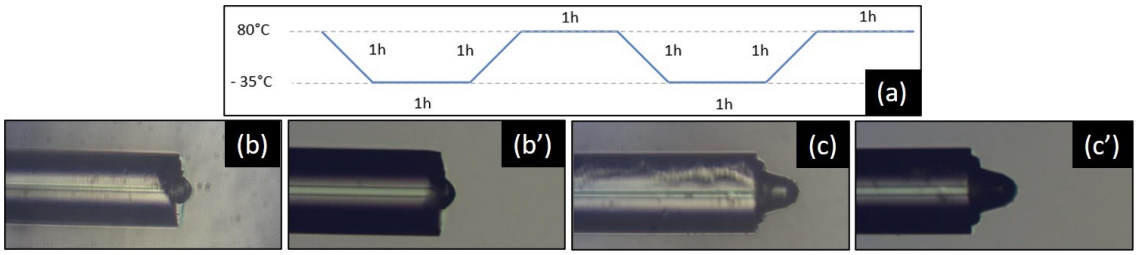

Figure 2.15: (a) Temperature evolution during thermal cycling test. (b)(b') and (c)(c') are images of two micro-lenses before and after the thermal cycling test. No deformation or debonding occurred.

Another important indicator to our micro-lens robustness is the successful thermal cycling test. The later consisted of 6 cycles of 4 hours each, where the temperature was varied between -35°C and 80°C as shown in figure 2.15 (a). The cycle consists in a linear temperature decreases over a period of one hour from 80°C to -35°C. When reached, this temperature is maintained for another hour. Following, the temperature is linearly increase back to 80°C, also over a period of an hour, then

maintained for another hour. This test achieved by one of our industrial partners, LeVerreFluoré on 6 fibers with micro-lens, shows that the micro-lens does not fall off from the fiber tip with time, under varying temperature conditions [156]. In addition, light coupling tests were performed before and after subjecting the micro-lens to thermal cycling, to see if any deformation occurrs. The lenses before and after thermal cycling are shown in figure 2.15. Multiple lenses with different geometries and sizes have been considered for this test, demonstrated the high robustness of the lens deposition technique.

2.2 On hollow core and photonic crystal fibers

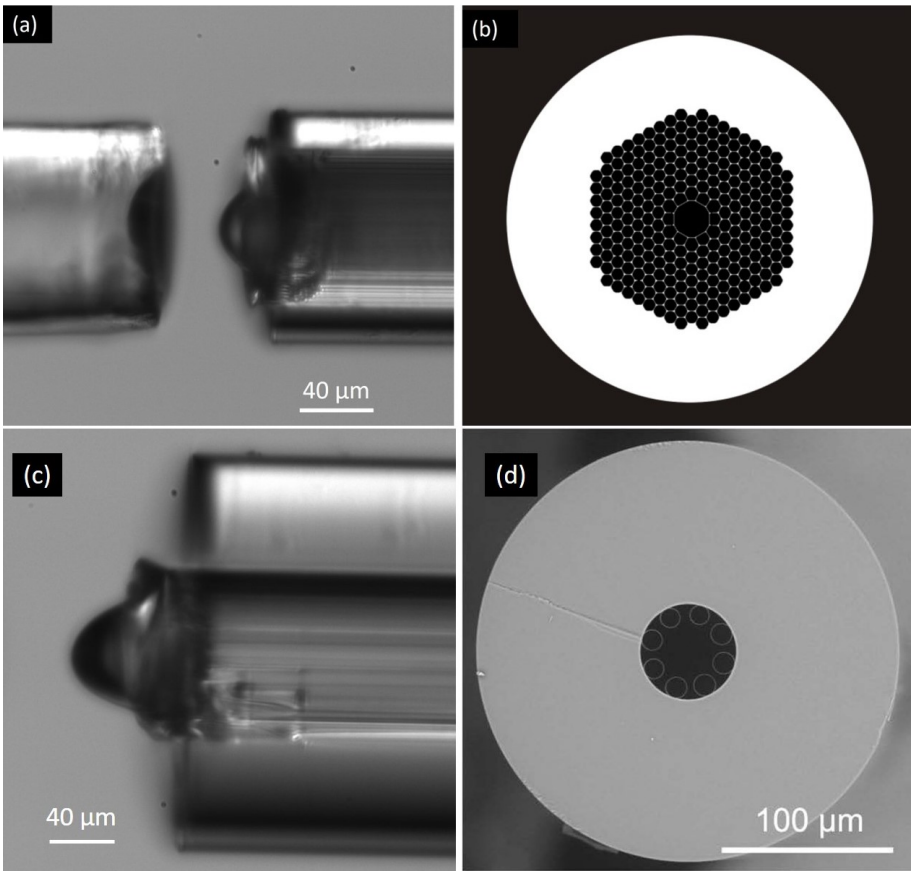

Figure 2.16: (a) On the right, a HCF equipped with one of our NOA61 micro-lenses. The mold etched in HF for 25 minutes is on the left. (b) Structure of a HCF similar to the one employed. The shown HCF has a 15 µm core diameter, while the one we used (HC-1060 from Thorlabs) have a 20 µm core diameter. (c) Anti-resonant HCF equipped with an NOA61 micro-lens. Its mold is etched for 40 minutes. (d) Facet of the employed anti-resonant HCF [130].

Fabrication of micro-lens for hollow core fiber HCFs and more generally microstructured fiber is a challenge. The micro-lens can be used both for injection and focusing. Testing the same procedure to deposit a micro-lens on a HCFs, the polymer inside the mold transitions immediately from the fiber mold into the hollow core and surrounding structure because of the capillary forces. This drains almost completely the mold, and no lens is obtained. The same phenomenon is encountered

in the case of micro-structured fibers with a core made of silica and a structured silica-air cladding. In a first approach, the low viscosity of the polymers we use, seems to make our technique not applicable on this type of fibers.

For these reasons, we have tried to increase the viscosity of the polymer before the lens deposition. To achieve that, following the mold filling step, we have cured the polymer for around 70% to 80% of the pre-curing times previously discussed. This means that for NOA61 the curing time is 7 to 8 seconds and variable for PDMS depending on the mold volume. Afterwards, the mold is set in contact with the HCF or micro-structured fiber. Then, the pre-curing is continued for the remaining time (2 to 3 seconds for NOA61), followed by the mold release. Figure 2.16 (a) shows a NOA61 micro-lens deposited on a HCF (reference: HC-1060 from thorlabs) with inner structure such as the one seen in figure 2.16 (b). The core diameter of the used fiber is 20 µm. As seen in figure 2.16 (a), the polymer was able to slightly penetrate inside the air cylinders (depth $\leq$ than 30 µm). This should not have a big impact on the fiber's properties such as its low dispersion and low absorption. Furthermore, another micro-lens has also been successfully deposited on a double cladding anti-resonant HCF [130]. The micro-lens on fiber is shown in figure 2.16 (c), and the corresponding fiber facet in figure 2.16 (d). The core diameter in this case is about 29 µm.

Focusing and numerical aperture evaluation due to the micro-lenses are currently being investigated.

2.3 On multi-core fibers

As presented in the state of the art, the deposition of micro-lens on each core of a multi-core fiber (MCF) is still a challenge. Our conviction was that our technique could be adapted for these fibers. The procedure of micro-lens fabrication for MCFs shares many similarities (mold etching, mold filling, alignment, and curing) with that of single-core fibers, but with additional challenges for each step.

2.3.1 Challenge 1: Mold cavity dimension control

Creating an array of the desired micro-lens design and dimensions for MCF is more difficult than in the case of single-core fiber. A first simple reason is that tapering a MCF to change the size of the cores is not a valid option, as this will alter the inter-core distances, and therefore the alignment between the mold cores and those of the target fiber. For this reason, having a lens/mold base for instance, bigger than that of the target MCF, usually requires asking the manufacturers to customize a MCF with the same distribution and core-to-core distance as the target fiber, but with bigger cores. Obviously, the same MCF can be used to achieve the mold, but this will limit our control on the lens' shape. For instance, step index cores will lead to conic lenses.

2.3.2 Challenge 2: Mold polymer filling

The increased number of mold cavities in the fiber, makes air trapping very probable during the process of mold filling as shown in figure 2.17. These air pockets can be

detrimental to the fabrication as the polymer will not be able to take the shape of the mold. However, this is not true for PDMS, due to its ability to displace or purge air bubbles out of micro cavities and structures [157]. This is because PDMS has a very high permeability to gases [158], several orders of magnitude higher than those of other commonly used polymers. This high gas permeability is attributed to the low glass transition temperature of PDMS ($\leq -70°C$), which allows the polymer chains to easily move and create free volume for gas molecules to pass through [159]. This is why PDMS is useful in many applications such as gas separation membranes, microfluidics, and biomedical devices [160].

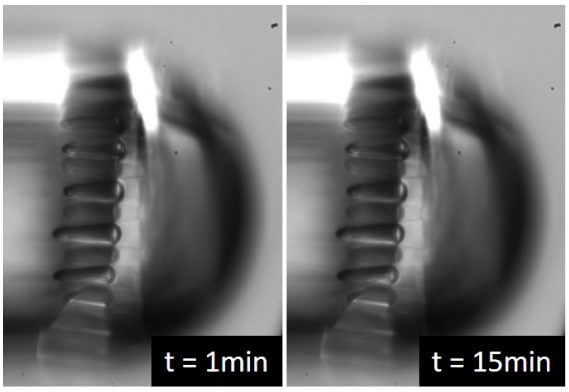

Figure 2.17: Attempt to fill a 37-core-fiber mold with NOA61. Air bubbles remain trapped underneath the polymer even after 15 minutes.

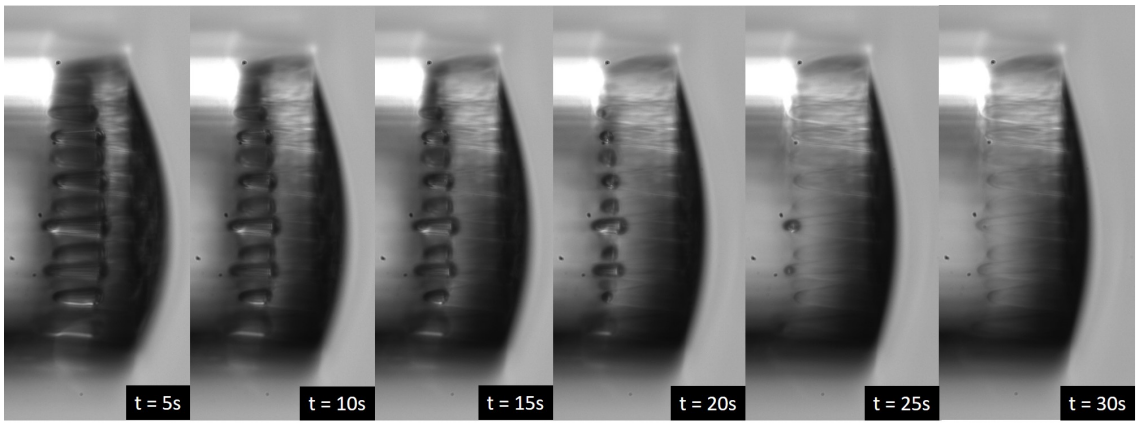

Figure 2.18: PDMS filling 37-core-fiber mold while purging air out of the structure in around 30 seconds.

Figure 2.18 shows how after fixed time intervals, air pockets are purged out by PDMS allowing it to penetrate all the space inside the mold structure. For this reason, all micro-lens arrays created for MCF, and shown in this work will be made of PDMS.

2.3.3 Challenge 3: Core Alignment

MCF cores can be distributed under various geometries and different center-to-center distances inside the fiber. The cores alignment between two MCF is therefore impossible by simply adjusting the X,Y,Z, and the two rotation axes shown in figure

2.7, since even-though the two outer fiber claddings seem aligned, the cores inside will not be facing each other. An additional degree of freedom that allows the fiber to rotate on its axis is required in this case. This can be achieved by swapping the fixed fiber 1 mount from figure 2.7 with a rotating mount such as the one shown in figure 2.19 (a). Figure 2.19 (b) and (c) illustrate examples of what perfect core alignment of seven and four-core fibers looks like. Our setup that consists of two orthogonal CCD cameras, is not able to give a clear image of the core positions. For this reason, we decide to perform the alignment using the light coupling between the two fibers. First, a Gaussian beam with a beam diameter larger than the fiber cladding is injected in the target fiber (Fiber 1: held by the rotating mount's fiber clamp). This allows to globally illuminate the majority of the cores, especially the ones adjacent to the center of the fiber. Part of the injected light will be guided by the cores. The light going through the cladding is radiated out of the fiber and lost after around 1m of fiber length.

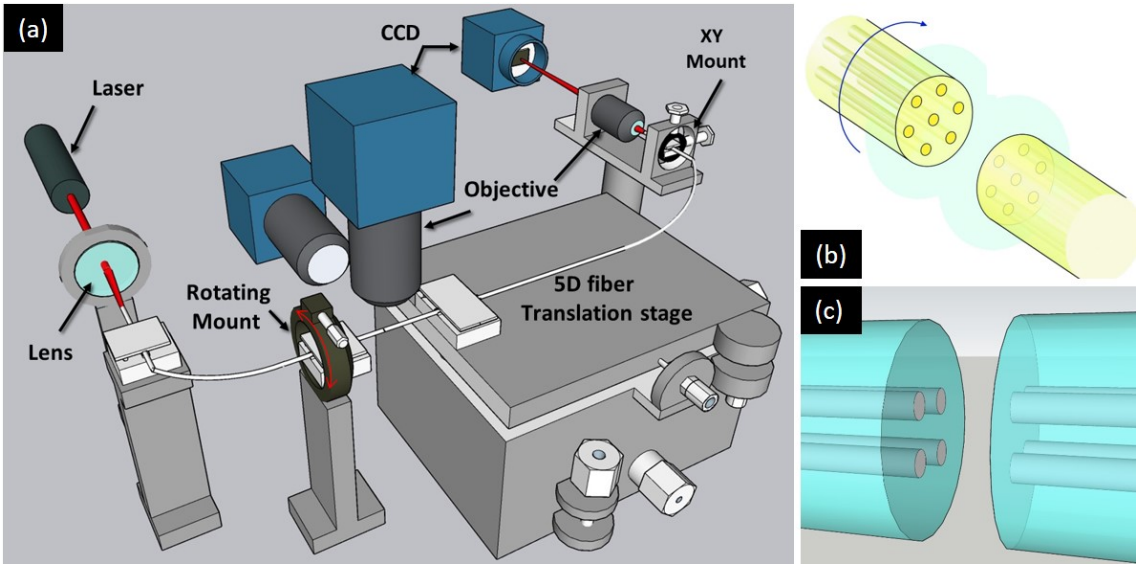

Figure 2.19: Schematic illustration of micro-lens fabrication setup adapted for MCF.

Afterwards, the mold fiber (Fiber 2: held by the 5D stage's fiber clamp), is brought close to the first fiber. Light from Fiber 1 cores will be coupled into those of Fiber 2 at very poor efficiency when the core alignment is not fulfilled. To monitor the coupling into each core, the other end of Fiber 2 is monitored thanks to a x20 objective that projects the image on a CCD camera. The two fibers tilt must be first adjusted, then the XY plane alignment must be performed, and finally rotations around the fiber axis can be executed to get all cores illuminated and be the brightest possible on the CCD.

While this alignment technique works in theory, we found it to be not accurate because of the cross talk between the cores and more importantly because no rotating mount is perfectly centered around the fiber axis. Which means, that adjustments in the X and Y planes must be made each time after rotating the fiber mount. This makes the alignment procedure more difficult and leads to around one properly aligned micro-lens array every five attempts on average.

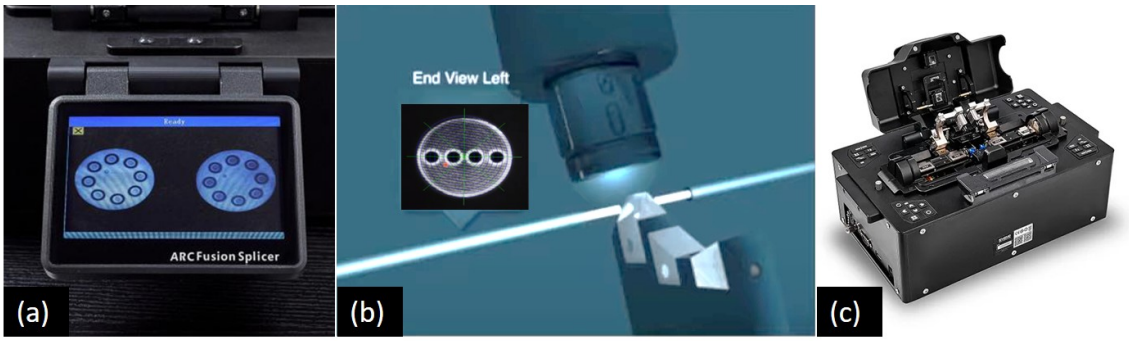

Figure 2.20: (a) Image of two MCF facets with matching orientation seen on ShinhoAmerica splicing device shown in (c). (b) Illustration of imaging technique that allows the visualization of fiber facets thanks to a Prism.

Looking the state of the art gave us a potential solution. Polymerization maintaining (PM) and MC fiber splicing tools have the capability of achieving perfect alignment by relying on an imaging technique that can give a perspective similar to what is shown in the illustrations in figure 2.19 (b) and (c). Such tools can be found for instance at Thorlabs and ShinoAmerica (device shown in figure 2.20 (c)) [161, 162]. The essential element of this imaging technique is a small prism that project the images of the fiber facets onto the camera as shown in figure 2.20 (b). By analyzing the geometries of the cores distribution on each side, the two images can be precisely matched to one another, as in figure 2.20 (a). This step would guarantee that the cores will end up exactly facing each other if the X,Y plane alignment is done properly. Unfortunately, due to time constraints, we were not able to implement this alignment technique.

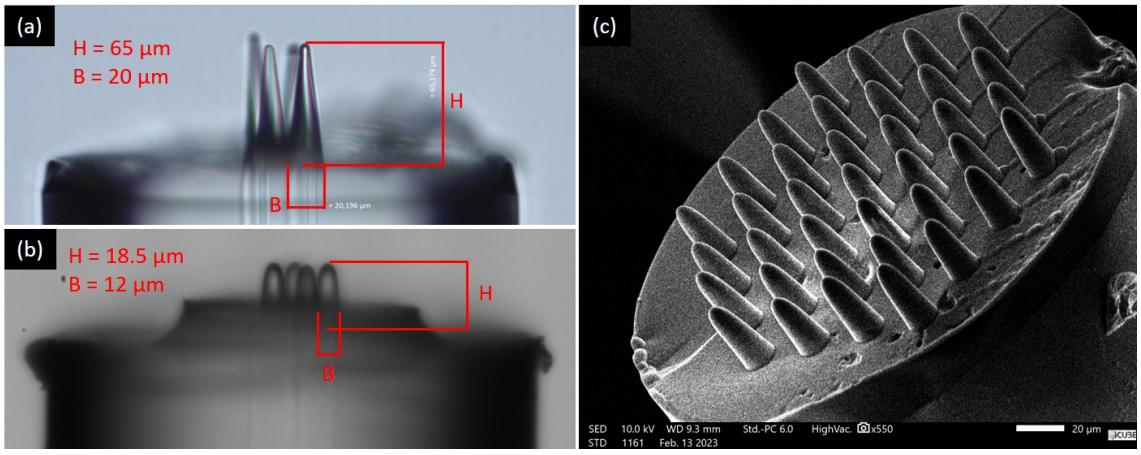

Figure 2.21: PDMS micro-lens array deposited on 4 and 37 cores fibers using: (a) a 4 step index cores fiber etched during 25 minutes (b) a 4 graded index core fiber etched during 10 minutes (c) a 37 graded index cores fiber etched during 10 minutes. The used HF concentration is 24%. The MCFs come from the Phlam laboratory.

When the alignment is achieved, the PDMS is pre-cured and the mold is released. Images of some of the achieved micro-lens arrays on MCFs from the Phlam

laboratory shown in figure 2.21.

The characteristics of the fibers used for the fabrications are summarized in table 2.2. Each fiber will be attributed a reference number.

Table 2.2: **MCF characteristics and mold etching times.**

Ref. number	**Fiber type**	**core index profile**	**Core diameter**	**Core-to-core distance**
4.1	4-core (square geometry)	Step index	4 µm	28.5 µm
4.2	4-core (square geometry)	Graded index	10 µm	28.5 µm
37.1	37-core (Hexagonal geometry)	Graded index	10 µm	28.5 µm

The fibers in figure 2.21 (a) and (b) are the 4.1 fiber, however, the fibers used to etch their respective molds in are the 4.1 and 4.2. The influence on the micro-lens shape can clearly be seen on the figures; the smoother curve are due to the gradient index, whereas the sharp peaks are a result of the mold being etched in step index cores. As for the fiber in figure 2.21 (c), it is fiber 37.1. Its mold, was also etched in the same fiber type.
The mold etching times, and PDMS pre-curing are shown in table 2.3.

Table 2.3: **MCF Mold etching times and PDMS pre-curing time.**

Fiber in	**HF etching time (min)**	**HF concentration (%)**	**pre-curing time (sec)**
Figure 2.21 (a)	25	24	24
Figure 2.21 (b)	10	24	9
Figure 2.21 (c)	10	24	15

The characterization results of all the micro-lenses presented in this chapter, including micro-lens arrays for MCF will be discussed in the next chapter (3).

2.4 Conclusion

In conclusion, the fabrication of micro-lenses on single-core fibers has been successfully demonstrated. The process involves the molding of a polymer droplet using a mold which has been chemically etched inside the core of a graded index optical fiber. An estimation of the quality of the micro-lenses, including surface roughness and geometry, has been obtained from scanning electron microscopy. The results show low surface roughness (sub wavelength over ten) and good geometrical symmetry, indicating the high quality of the fabricated micro-lenses. The durability of the micro-lenses has been tested through thermal cycling No deformation nor detachment has been observed. In addition, a new method for making a fiber spacer that is compatible even with Mid-IR fibers, such as fluoride and chalcogenides fibers

has been presented. It consists of aligning the fibers and separating them by the desired spacer distance (preferably ≤ 200 µm per procedure). A Polymer droplet is then introduced between the fiber ends, followed by pre-curing and separation.

For hollow core fibers and more generally for micro-structured fibers, we have shown that the fabrication process requires a pre-curing to increase the viscosity of the polymer in the mold before the contact with fiber. The challenges to fabricate micro-lenses on MCFs, which concern the control of the mold size, the filling of the mold with polymer without air bubbles, and the cores alignment have been addressed with success through customizing MCFs with larger cores, using PDMS for filling the mold due to its high gas permeability, and employing a rotating mount for cores alignment. Overall, the fabrication of micro-lenses on single-core, micro-structured fiber, and MCF fibers are promising results, paving the way for various applications involving fiber optics. The technique is easy to implement, not expensive, compatible with many fiber types, allows the micro-lens shape to be controlled, centered on fiber core and with curvature radius as small as 10 µm. Their characterization is described in the next chapter.

Chapter 3

Micro-lens modeling and characterization

In the previous chapter, we have introduced a novel micro-lens fabrication technique for both single and multicore fibers. This technique holds great promise for improving the performance in a wide range of optical applications of these fibers, as well as other types of fibers as we will see in section 4.1. In this chapter, we shift our focus to the numerical modeling and experimental characterization of these newly fabricated micro-lenses. In particular, we will evaluate how the micro lenses focus, collimate or deflect the light emerging from the fiber depending on the micro-lens design.

For this study, we utilize the COMSOL Multiphysics software (version 6.0), which solves numerically the propagation equation using the finite element method. The wave-optics module in frequency domain has been used. Due to computing time and memory size limitations, the simulation has been done in 2D. Then experimental measurements have been conducted to validate the numerical results. Additionally, we investigate the effect of spacers (otherwise known as coreless fibers or beam expander), micro-lens misalignment, and the potential of a coating layer to improve the performance.

3.1 Numerical study of the micro-lens design

3.1.1 Lens Design

When designing a micro-lens we need to first determine what application we are going to use it for. Depending on the application, some constraints may be imposed; For instance, in light coupling from an optical fiber into a waveguide or photonic integrated circuit (PIC), a specific beam diameter is needed for optimal coupling efficiencies; In laser processing a long WD is often required; In optical coherence tomography, a large depth of field is a necessity...
For each application, the optical fiber's choice is a key parameter that impacts the micro-lens design. For example, it is easier to obtain longer WDs and smaller spot sizes by using Large mode area (LMA) fiber rather than normal SM fibers [11]. On the contrary, for a given WD, a larger depth of field beam is easier to achieve with

a SM fiber with a smaller MFD...

Since there is a countless number of different optical fibers with different core sizes, MFDs and cut-off wavelengths, we need to restrict our design study to few fibers and wavelengths of interest. The fiber that we have studied the most is the SMF28. This fiber initially developed for telecom applications has a 9 ± 1 µm core diameter and a NA of 0.12. Simulations have been performed at 1550 nm and 1070 nm. However, most of the characterizations have been performed at a wavelength of 1070 nm that corresponds to our VGEN ytterbium doped fiber nanoseconde pulse laser from Spectraphysic. The SMF28 is a two-mode fiber at 1070 nm and only becomes SM at 1310 nm and beyond. This choice has been made in order to make the beam characterization using the camera with a silicon detector possible. At 1300 nm and 1550 nm an InGaAs camera would be required[163]. This source choice has also two other advantages: 1070 nm is close to the classical telecom wavelengths (850 nm, 1300 nm and 1550 nm) and also allows for material processing. This allows us to consider a larger range of possible applications. With proper light injection (matching the incident excitation beam diameter with that of the MFD of the fiber) and no fiber bending, we can couple most of the light in the fiber's fundamental mode and get a proper Gaussian beam at the output.

Our fiber micro-lenses are generally aspherical and such surfaces' transverse profile shapes, z(r), are described by equation 3.1.

$$z(r) = \frac{r^2}{R(1+\sqrt{1-(1+\kappa)\frac{r^2}{R^2}})} + \alpha_4 r^4 + \alpha_6 r^6 + ... \tag{3.1}$$

Where R is the radius of curvature of the tip, κ is the conic constant which can roughly represent the surface shape, the coefficients α_i describe the deviation of the surface from the axially symmetric quadric surface specified by R and κ.

However, studying the effect of each parameter would be very complex and not very beneficial since some parameters do not have a big impact on the final result, and in our fabrication, we do not have precise control over all of them. Thus, to simplify the study without sacrificing accuracy, we have used Bézier curves, more specifically the Rational Bézier curves. A Bézier curve is a continuous curve defined by a set of control points; three in our case, are enough to describe half of the micro-lens and then complete the rest by symmetry. One of the points (P_2) is chosen to be at one of the edges of the micro-lens's base, another (P_0) at its tip, and the last (P_1) will have the abscissa of (P_2) and the ordinate of (P_0). A parameter called the Bézier weight "W" and can take any positive value. At W= zero, a conic shape is obtained, while at W= 0.7 the micro-lens will be not far from being elliptic. Example of Bézier curves are shown in figure 3.1. The equation that describes any rational Bézier curve is parametric and is given by [164]:

$$P(t) = \frac{(1-t)^2 P_0 + 2(1-t)tWP_1 + t^2 P_2}{(1-t)^2 + 2(1-t)tW + t^2} \tag{3.2}$$

With this approach, the lens can be described by its base diameter, height, and the Bézier weight which roughly describes its shape. An additional advantage, is

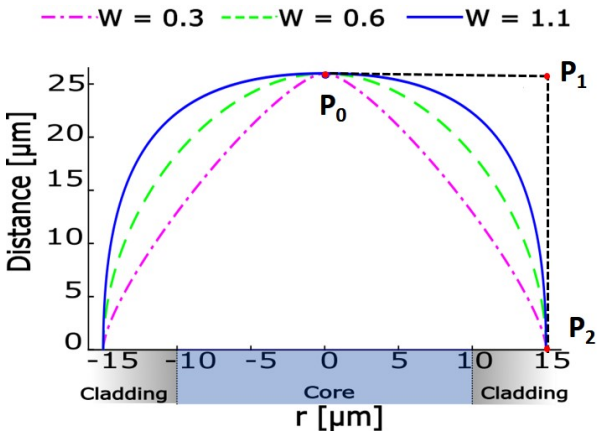

Figure 3.1: Lens base and height are 30 and 25 µm, respectively, and 3 Bézier weights W: 0.3, 0.6, 1.1.

the ease of implementation of the Bézier curve in COMSOL.

To study the effect of each of the mentioned three parameters on the outgoing beam, two of them will be fixed at a time when a third is varied. We begin first by the Bézier weight.

3.1.1.1 Bézier weight

The considered lens base and height are 20 and 15 µm, respectively. The Bézier weight W will be varied from 0.1 to 1 with a 0.1 increment. The simulations are carried out at 1550 nm.

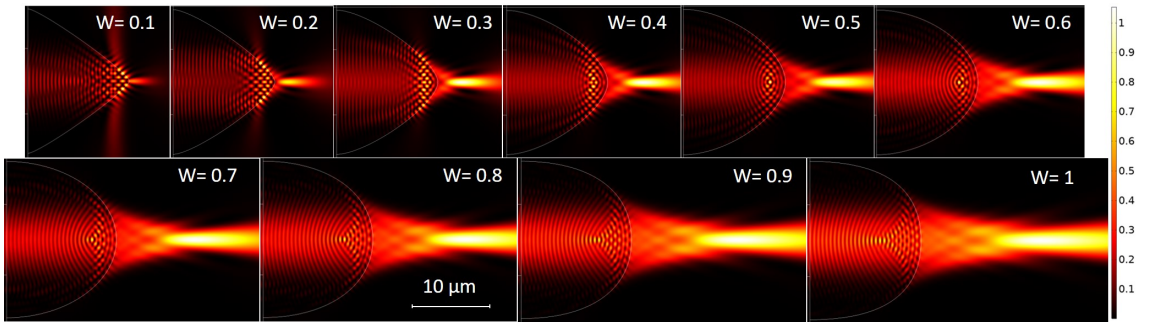

Figure 3.2: Beam intensity distribution in space upon interacting with a PDMS micro-lens with a Bézier weight going from 0.1 to 1. Lens base and height are 20 and 15 µm. SMF28 in 2D. Fundamental mode at 1550 nm.

In figure 3.2 and 3.3 we can see a linear dependency of the the beams' WD and FWHM to W. When the later is low (approaching 0), it means the lens has a high curvature (at apex), resulting in strong focusing power. However, this intense focusing comes at the expense of a shorter WD. On the other hand, when the Bézier weight is high (close to 1 for instance), the depth of field is extended, allowing a wider range of distances to be in focus. However, the focusing capabilities will be compromised.

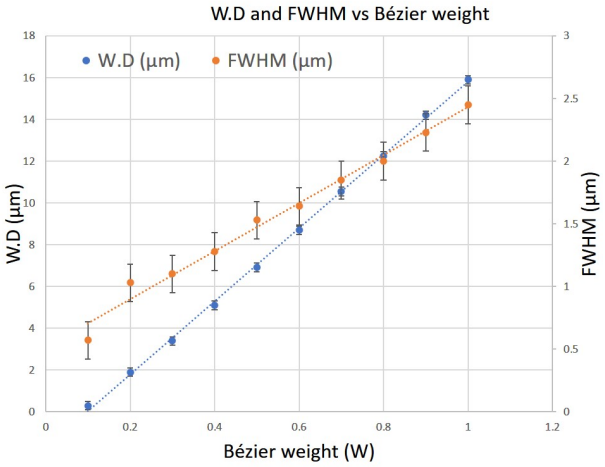

Figure 3.3: WD and FWHM evolution of the emerging beam as function of the Bézier weight describing the micro-lens. PDMS Lens base and height are 20 and 15 µm on a SMF28 in 2D. Fundamental mode at 1550 nm.

3.1.1.2 Base diameter and height

If we keep W and the height of the micro-lens constant, increasing the lens base diameter has similar effect to that of increasing the Bézier weight. This change causes the micro-lens to have a larger radius of curvature. Conversely, increasing the height of the micro-lens has the opposite effect on the curvature. As the height increases, the lens adopts a sharper form with higher curvature. Long micro-lenses with small base diameters (close to the MFD of the fiber) must be avoided. Namely, Yoshiki Kamiura et al. have demonstrated that higher order modes will be excited in the lens when its length exceeds 10 µm [137].

3.1.1.3 Spacer

A spacer gives a lot of flexibility in designing the micro-lens and permits, in some cases, to achieve better performances not possible with just a micro-lens (for instance a combination of large WD and small beam FWHM). For example, figure 3.4 shows an SMF28 equipped with a high curvature micro-lens. A highly focused beam with a FWHM = 1 µm is obtained. However, the WD is just 6 µm. To get a longer WD (21 µm), a design such as the one seen in figure 3.5 (a) can be used. However, it comes at the cost of larger beam FWHM (2.1 µm). A spacer in this case can be implemented to overcome the presented limitations by allowing to maintaining almost the same long WD, and leading to a highly focused 1 µm FWHM beam, as shown in figure 3.5 (b).

3.1.2 Reflection losses and coating

In figure 3.2, high intensity local maxima can be found inside the micro-lens (for W$\leq$ 0.2)). These are due to interferences between the incident fundamental mode and light reflected at the micro-lens' interface. These reflections can correspond to backscattered light (W$\leq$ 0.3) or laterally deflected light (W$\leq$ 0.1). In both cases, these can be problematic since they equate to losses. Moreover, this puts the micro-

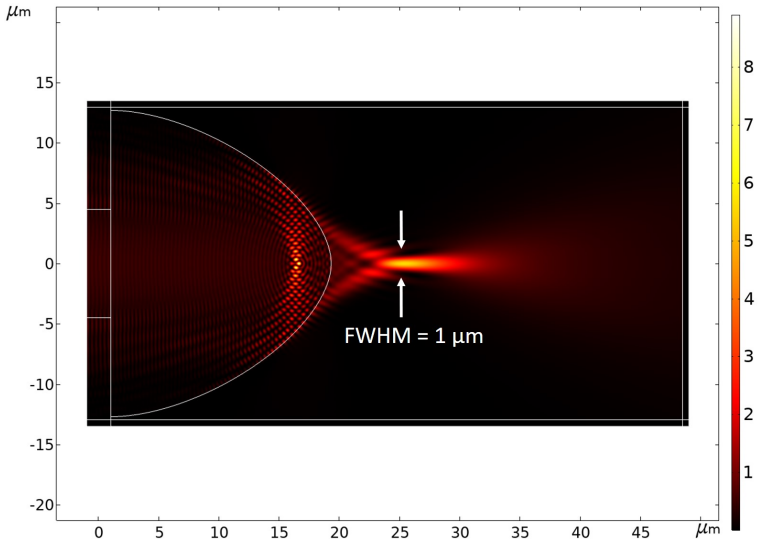

Figure 3.4: Intensity distribution simulation with a NOA61 micro-lens with a base diameter, height and W of 25 µm, 18 µm, and 0.47 respectively. The obtained FWHM is 1 µm and the WD is 6 µm. SMF28 in 2D. Fundamental mode at 1070 nm.

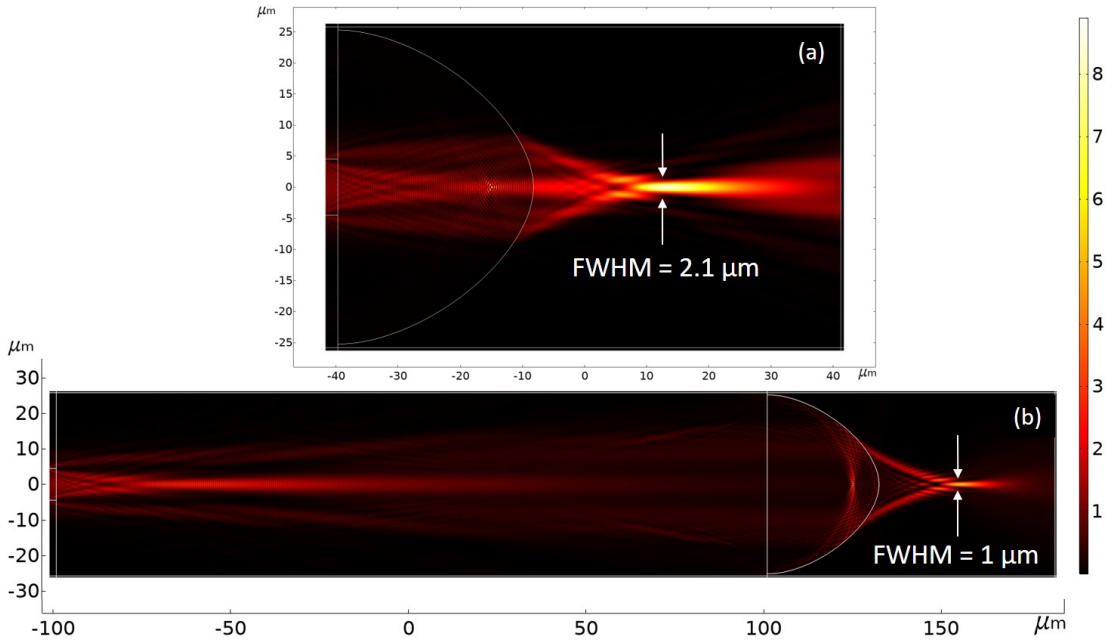

Figure 3.5: Intensity distribution simulation of the SMF28 fiber fundamental mode at 1070 nm interacting with (a) a NOA61 micro-lens with a base diameter, height and Bézier weigh of 50 µm, 31 µm and 0.5, respectively (WD = 21 µm); (b) the same micro-lens but on a 200 µm long NOA61 spacer (WD = 22.5 µm). A more tightly focused beam is obtained

lens at higher risk of damage when using high power lasers. To numerically study these losses due to reflection, a 1 W guided beam has been considered. Three probe surfaces have been defined: one at the input to evaluate the input power and the backscattered one, the second probe at the output to evaluate the output power and the third one laterally parallel to the propagation axis to measure the power lost

to the sides. The laterally deflected power is multiplied by two since the system is symmetric (the lateral losses above and below the axis are equal). Figure 3.6 (a) show the evolution of the powers with respect to W. Clearly, the losses by reflection are very important for small W values.

To improve the efficiency of the system by reducing the reflection, an Anti-reflective (AR) coating has been simulated. For flat interface, the coating's thickness must ideally be equal to $\lambda/4n_2$ [165], and its refractive index equal to $\sqrt{n_2 n_1}$. n_1 being the micro-lens's polymer index and n_2 that of the surrounding medium. In our case, the surrounding medium is air and PDMS's index is 1.39 at 1550nm [166], hence the coating's thickness and index are 387.5 nm and about 1.179, respectively. A noticeable 5% improvement is obtained with the AR coating.

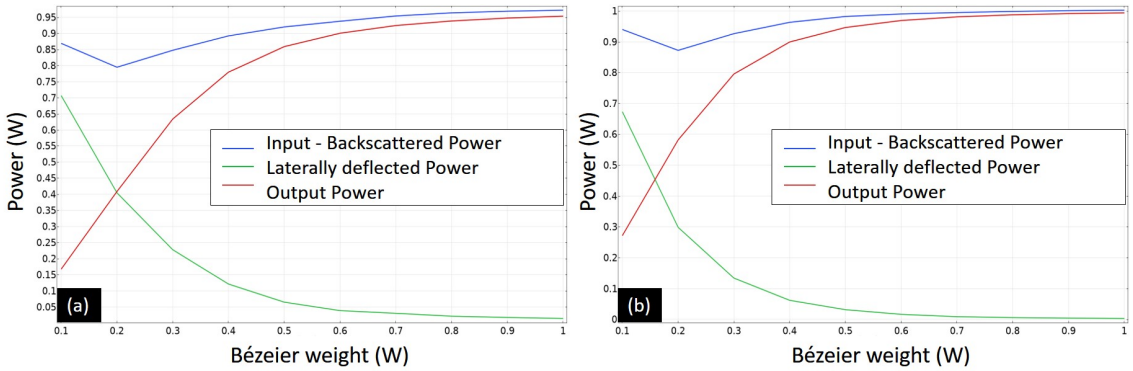

Figure 3.6: Evaluation of the transmitted, back-scattered, and laterally deflected power as function of the Bézier weight of an (a) uncoated and an (b) AR coated micro-lens. A noticeable 5% improvement is obtained with AR. Lens base and height are 20 and 15 µm. SMF28 in 2D. Fundamental mode at 1070 nm.

It is important to note that, in case of light collection, from a laser diode into a lensed fiber for instance, the losses due to the micro-lens, even at high curvatures (low W), remain negligible in comparison to those generated when focusing the beam, as seen earlier. That is because when light encounters the air-microlens interface, no total internal reflections can take place. The losses can be evaluated by the Fresnel reflections . Figure 3.7 helps to visualize this. The beam propagation in this figure is from right to left. The Gaussian source, on the right, has a beam diameter of 5 µm and a wavelength of 1070 nm. The micro-lens is made of PDMS and has 15 µm height and base diameter. Its Bézier weight W is 0.4. Only a small portion of the light intensity is lost by reflection. The power losses as backscattered and deflected light is only 5.5%. The same done for W= 0.3 and 0.5, leads to 6 and 4 % loss, respectively. These values are very close to the average Fresnel losses obtained from a flat interface [167]. An anti-refractive coating can be highly effective at reducing these losses.

3.1.3 Effect of micro-lens misalignment

During the micro-lens alignment procedure, 100% accuracy is not always guaranteed. Since often, there is a margin of error on the readings of the coupled power or pixel counting, which are the two alignment techniques discussed in section 2.1.3.

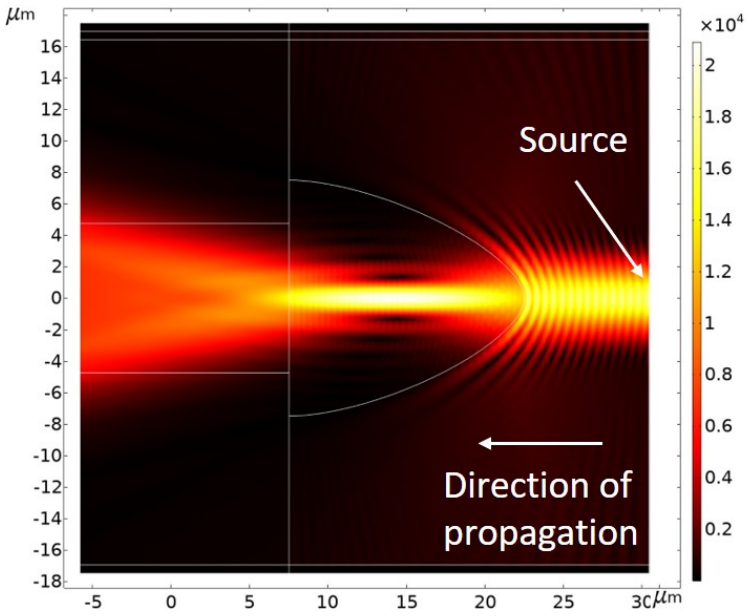

Figure 3.7: Intensity distribution simulation. The direction of propagation is from right to left: a 5 µm diameter Gaussian beam (1070 nm wavelength) from the right coupled into a SMF28 fiber with a PDMS micro-lens (height and base of 15 µm, W= 0.4). This does not represent a good coupling configuration.

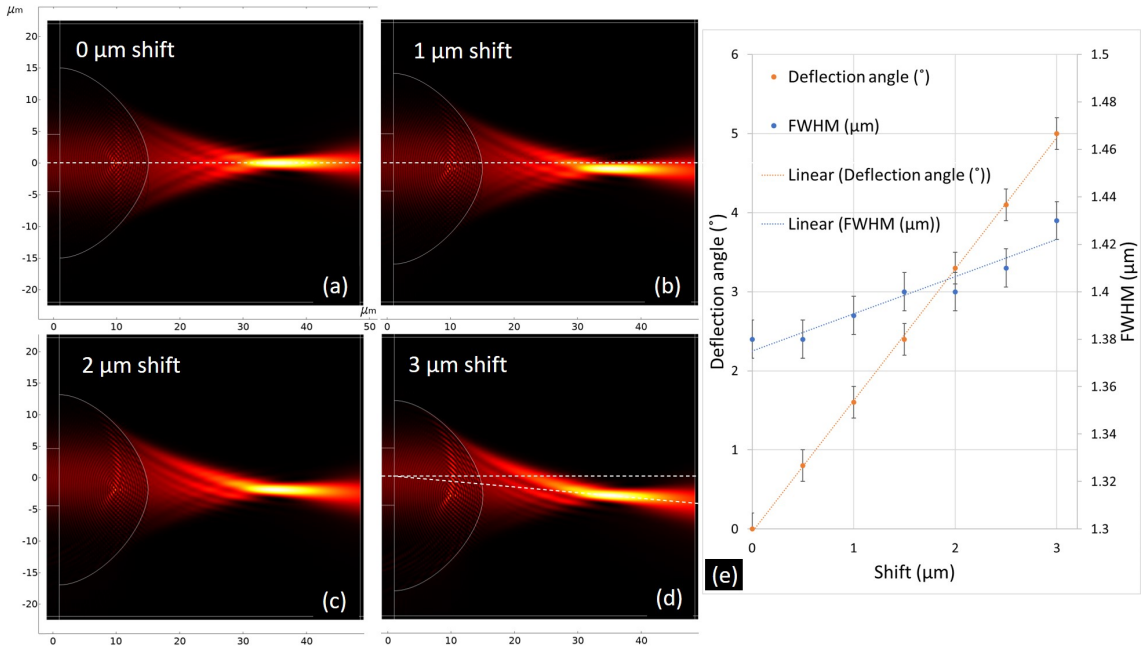

Figure 3.8: (a - d) Intensity distribution simulation at different micro-lens position with respect to an SMF28 core axis. (e) Beam deflection and FWHM as function of the micro-lens's shift. PDMS micro-lens (height of 14 µm, base of 30 µm, W= 0.47). Fundamental mode at 1070 nm.

To determine what is the tolerable deviation from a perfect alignment, a study of the beam deflection angle with respect to the micro-lens shift was performed. By referring to experimental characterizations in literature, we see that deflection angles of $\leq 7°$ are often considered acceptable. It obviously depends on the application. For

instance, in [102], where 3D printed diffractive Fresnel lenses are fabricated to be used for optical trapping, a 6.7 and 3.2° deflection angles are measured. Moreover, in [84], for a GRIN lens, a 1.4° deviation from the theoretical center is observed. My simulations presented in figure 3.8 (a-e) show that a 0.8 µm shift of 14 µm height and 30 µm base micro-lens from the center of a SMF28 would lead to a 1.4° deviation, which can be considered as acceptable for most applications, since it is equivalent to what is usually obtained by a GRIN lens. Hence the acceptable alignment error for this king of micro-lens during the fabrication must remain below ±0.8 µm

The FWHM on the other hand, as seen on figure 3.8 (e), does not increase significantly with respect to the micro-lens shift, but a 2D simulation, such as the one presented here, is not sufficient to see the full impact on the beam. For that, a 3D representation would be required, what was not possible using Comsol. Increase in aberrations and astigmatism will undoubtedly be observed at high deflection angles.

It must be noted that for some applications, light deflection, often at high angles ($\geq 10°$) is needed. For these cases, a controlled and precise decentering may be a solution.

3.2 Experimental characterization

3.2.1 Single-core fiber

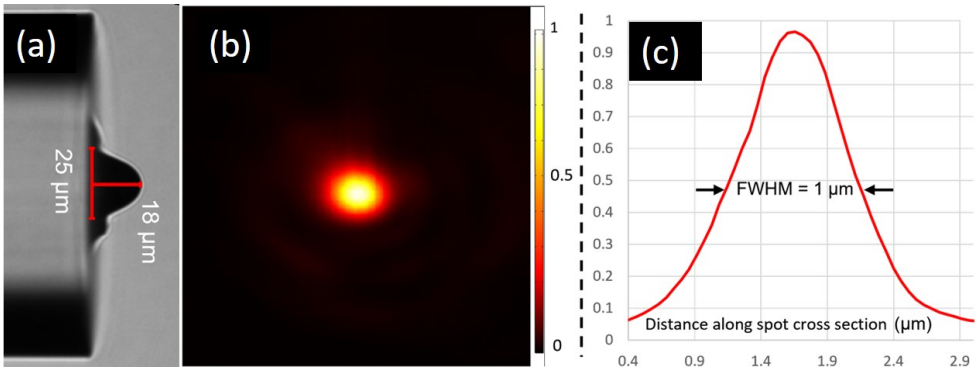

Figure 3.9: (a) SMF-28 with NOA61 micro-lens; base diameter, height and W are 25 µm, 18 µm, and 0.47, respectively. (b) Intensity measurement of the beam at the waist for the fundamental mode at 1070 nm. (c) Plot profile of beam waist cross-section.

The characterization setup depicted in figure 1.7 was first designed by D. Bouaziz and S. Perrin [46]. I have rebuilt an improved version of it to check the validity of our simulation model and characterize the achieved micro-lenses.

The first focusing micro-lens to be considered is shown in figure 3.9 (a). Its base diameter, height and W are 25 µm, 18 µm, and 0.47 respectively. The micro-lens is deposited on a SMF28 fiber. The fundamental mode of the fiber is excited at 1070 nm and the output beam is imaged at the waist plane (where the smaller diameter is

measured). The measured spot, shown in figure 3.9 (b) is quite symmetric. A profile along a cross section gives the curve shown in figure 3.9 (c). The FWHM (distance between the two intersection points at half the maximum intensity, $I_{max}/2$, is equal to 1 µm. It is in agreement with the simulated value shown in figure 3.4. This demonstrated experimentally the ability of our micro-lens to focus the light from a SMF28 on a one wavelength spot.

Another micro-lens design that permits to obtain a long Rayleigh length (or long depth of field) will now be considered. The micro-lens deposited on the SMF-28 is shown in figure 3.10 (a). The corresponding simulated results shown in 3.10 (b) depict a slowly changing beam diameter over a distance of more than 30 µm that could be useful for fiber-fiber coupling. The beam's FWHM vary between 3.3 and 3.8 µm over the mentioned distance. It is in good agreement with the experimental measurements in figure 3.10 (c).

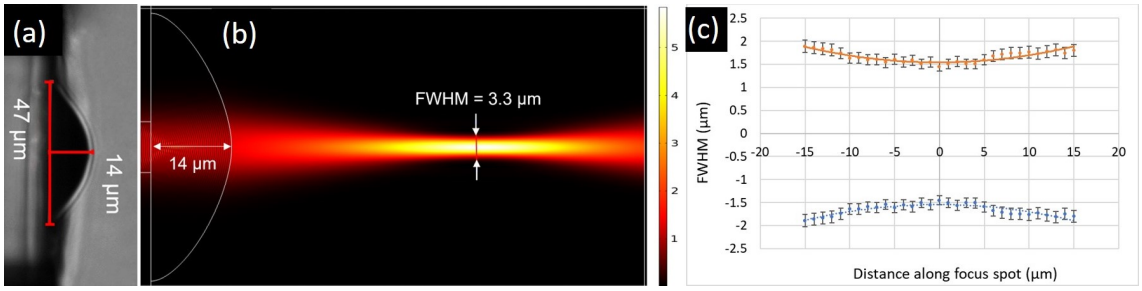

Figure 3.10: (a) SMF-28 with NOA61 micro-lens; base diameter, height and W are 47 µm, 14 µm, and 0.42 respectively. (b) 2D simulation of the fundamental mode at ($\lambda = 1070\ nm$) (c) experimental measurement of the evolution of the FWHM along the optical axis (0 on the x-axis represents the position of the beam waist).

The presented comparisons between experimental and numerical results show that the numerical model with micro-lens shape described by Bézier curves can accurately predict the optical behavior of micro-lenses. These measurements and comparisons have been carried out on many fibers and micro-lenses with a good repeatability.

3.2.2 Multi-core fiber

The characterizations of the beam at the output of MCFs at 1070 nm have been performed at ICube on the same setup as the one used for single-core fibers (figure 1.7). Only the injection part can be different. Additional measurements have been done at 1550 nm by our partner at the Phlam Lab. Two different configurations for light injection have been considered. The first where each core is addressed individually, and the second one, where all, or a selection of them are addressed at once. The injection techniques will be first explained in the next section, then the characterization results will be discussed in section 3.2.2.3.

3.2.2.1 Injection in each core individually

Injecting light into a single core of a MCF can be achieved using either a SM fiber or a focused laser beam with an appropriate focal length to match the diameter of

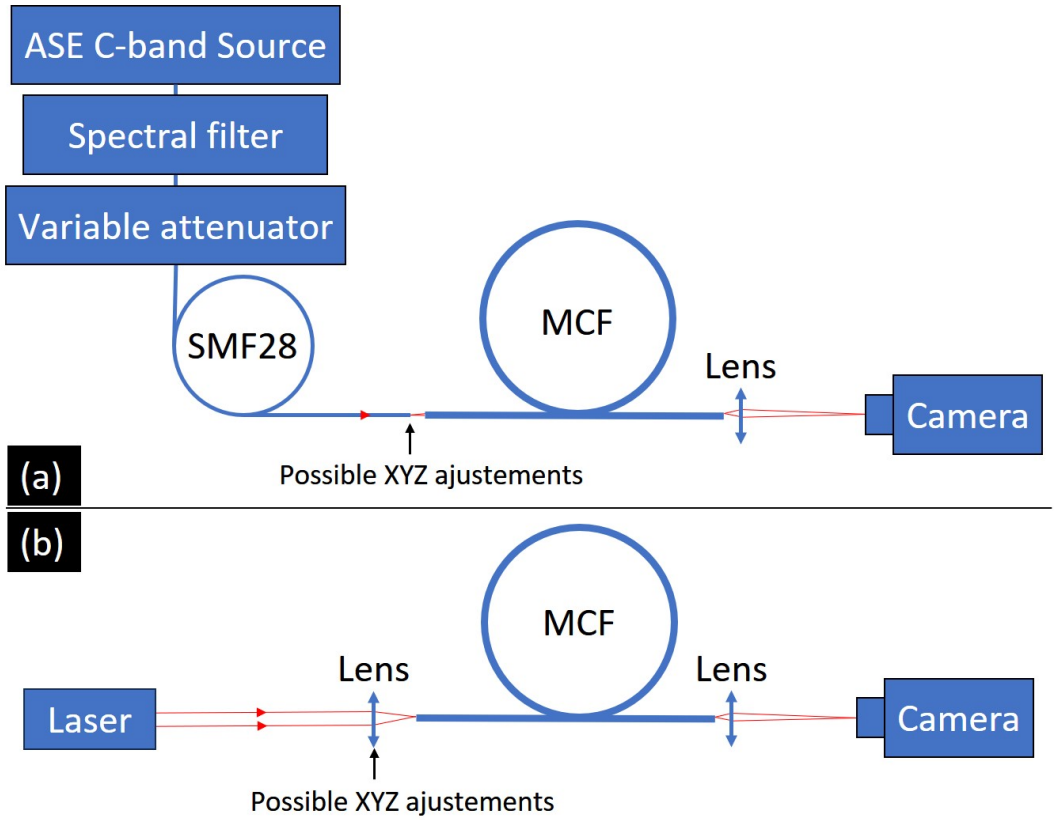

Figure 3.11: Schematic representation of MCF characterization setup of the Phlam lab with light injected in each core individually using: (a) a SMF28; (b) a focused laser beam. For wavelengths $\lambda \geq 1.1\mu m$, they use a camera with an InGaAs sensor [168] instead of a silicon-based one.

the core MFD. These two configurations are illustrated in Figure 3.11. In Figure 3.11 (a), the SMF28 configuration is shown, while in Figure 3.11 (b), a focusing lens is used. The MCF input end is placed on an XYZ micro-positioning stage to enable to select the core to excite.
By injecting light using this approach, each core can be individually characterized by acquiring images from the camera. Then a complete characterization image can be obtained by merging numerically all the acquired images into one.
This approach is the simplest to implement but is relatively slow.

3.2.2.2 Multi-Core dynamic excitation by beam shaping

Light injection into few or all cores simultaneously can be achieved by implementing a diffractive optical element capable of splitting the main incident beam into multiple ones [169, 170]. SLMs, generally based on LCOS are dynamic diffractive optical elements are useful also due to their phase modulation capability [171]. Phase modulation is superior to amplitude modulation because higher diffraction efficiency can be achieved. It allows a more efficient utilization of the available light power. Full field (amplitude and phase) modulations are also possible using two phase-only SLM. The Gerchberg-Saxton algorithms is generally used to computed the phase mask also called computed generated hologram [172, 173]. By applying appropriate phase masks and/or amplitude modulation patterns on the SLM, the light passing

through leads to the generation of specific patterns or structures.

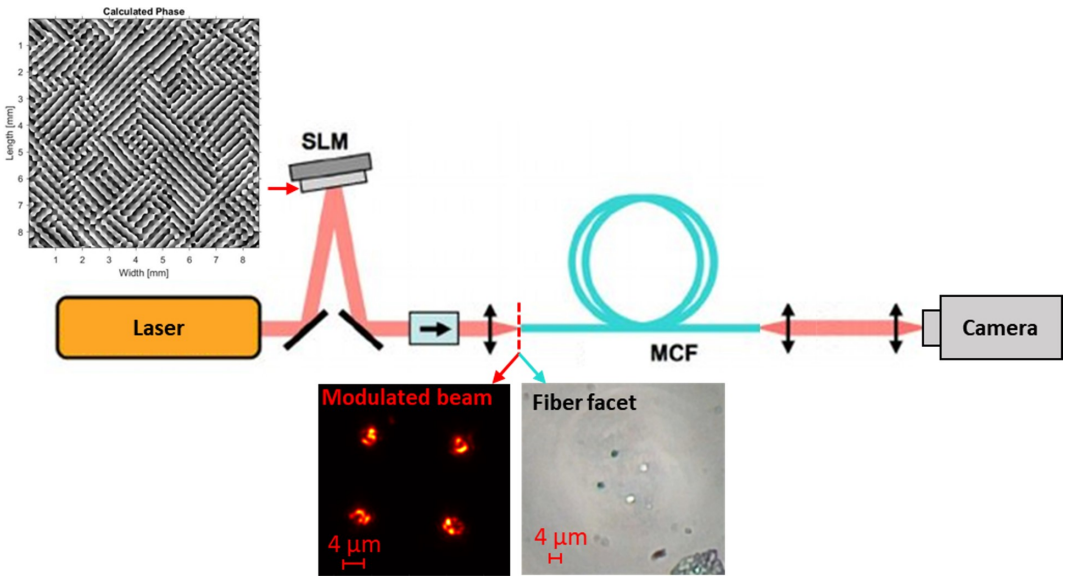

Figure 3.12: Schematic representation of MCF characterization using an SLM. [174]. Phase mask to generate 4 spots having a 4 µm diameter, equivalent to the MFD of the fiber cores.

The beams generated by the SLM must overlap the cores positions. Therefore, for MCFs, the sought-after pattern is an array of multiple Gaussian spots centered on the the MCF's cores, and with diameters corresponding to the core MFD.

A typical MCF characterization setup of the Phlam lab, using a SLM is represented in Figure 3.12. The gray-scale image shown on the SLM is the phase mask, and it represents the phase delay of each pixel of the SLM's liquid crystals. The relationship between the phase shift and gray-scale is linear for a reflective SLM, but this is not the case for a transmission one [175].

This characterization technique, although more complex to set up, allows faster characterization and the ability to dynamically choose the cores to be illuminated. I have developed a similar setup at ICube for future uses. The optimization of the multi-beam generation and phase maps calculation is still a work in progress.

3.2.2.3 Characterization results of an array of micro-lenses for a 4-core fiber

For our measurements, only the first method has been implemented.
The two fibers that have been characterized, before and after the deposition of the micro-lens array, are named 4.1 and 37.1 (details are in table 2.2). The corresponding lensed fibers are those of figure 2.21 (b) and (c). Fiber 4.1 has 4 cores separated by 28.5 µm and a cut-off wavelength between 1050 and 1100 nm, while the 37.1 has 37 cores separated by 28.5 µm and a cut-off wavelength of 1330 nm because of its larger core. The characterizations have been carried out at 633 nm (37.1 only), 1070 nm in ICube and at 1550 nm at Phlam.

At 1070 nm:
The four output beams measured from fiber (4.1) without micro-lens are represented

in figure 3.13 (a). Their beam FWHM measure 3.5 ± 0.1 µm, which is the core MFD. In contrast, the MCF with four parabolic micro-lenses led to four focused beams. One has a FWHM of 1 ± 0.1 µm as shown in figure 3.13 (b). These results show that our core-mold alignment procedure is valid since the four cores led to a focused beam. However, we see some imperfections. Two spots rather than one can be observed. Knowing that the fiber is SM at the employed wavelength, we can attribute these defects to either small micro-lenses misalignment or to lens modes as explained by Yoshiki Kamiura when the micro-lens is as a micro-pillar with a height > 10 µm [137]. This has been discussed in section 1.4.2. For better alignment a solution has been suggested in figure 2.20.

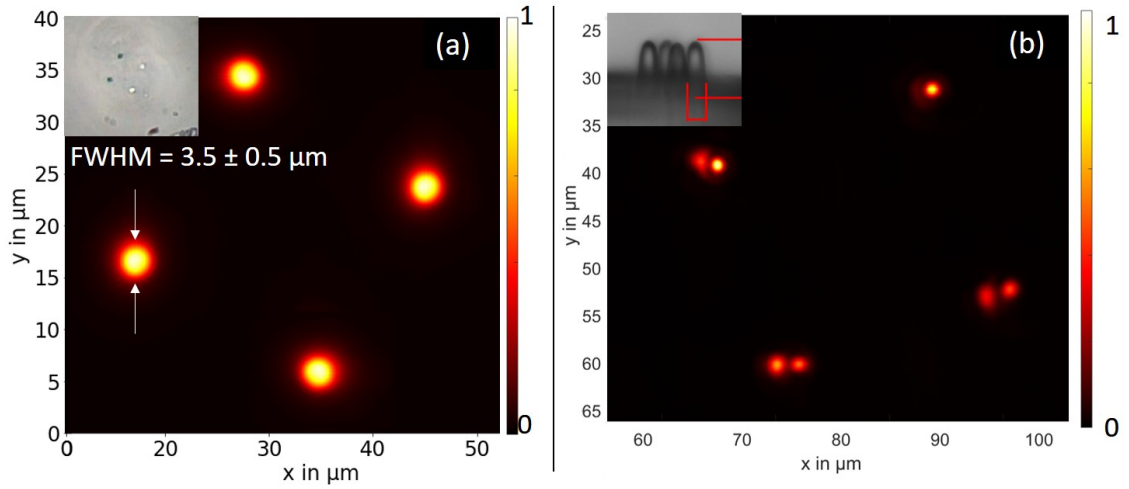

Figure 3.13: 4-SM-core fiber's output beam characterization at 1070 nm (fiber 4.1): (a) without lens (inset: distal face) ; (b) with an array of 4 micro-lenses (figure 2.21 (b)) (inset: array of the 4 parabolic micro-lenses).

Nevertheless, the experimental results depicted in figure 2.21 (b) demonstrate a FWHM beam of 1 µm after the micro-lens. These experimental findings are in close agreement with the COMSOL simulation shown in figure 3.14 (a), which was conducted on a single core

At 1550 nm:
Similar measurements have been conducted at a wavelength of 1550 nm at Phlam Lab. The results after selective excitation of each individual core are represented in figure 3.15.

The light is focused by the 4 micro-lenses creating four spots having FWHM around 1.2 µm. The difference in the focused spot quality is very low and may be due to small misalignment. Nevertheless, in this case as well, we see a similar behavior to what has been obtained numerically in figure 3.14 (b) where a FWHM of 1.1 µm was predicted.

3.2.2.4 Characterization results of an array of micro-lenses for a 37-core fiber

A top view of fiber 37.1, with 37 cores having each a 4 µm diameter and separated by 28.5 µm, is shown in figure 3.16 (a), while its lens equipped version is shown in

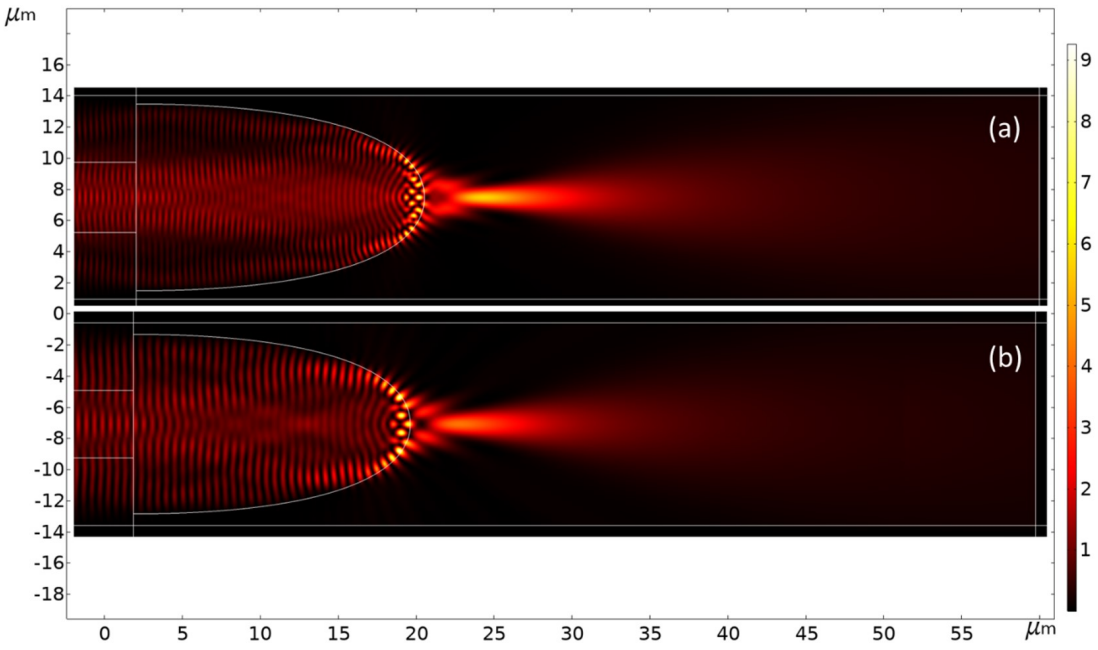

Figure 3.14: Simulated intensity of the fundamental mode of a 4 µm core with a micro-lens. Micro-lens base, height and Bézier weight W are 12 µm, 18.5 µm and 0.914 respectively. (a) For $\lambda = 1070$ nm: FWHM = 0.97 µm and WD = 3.7 µm. (b) For $\lambda = 1550$ nm FWHM = 1.1 µm and WD = 2.8 µm.

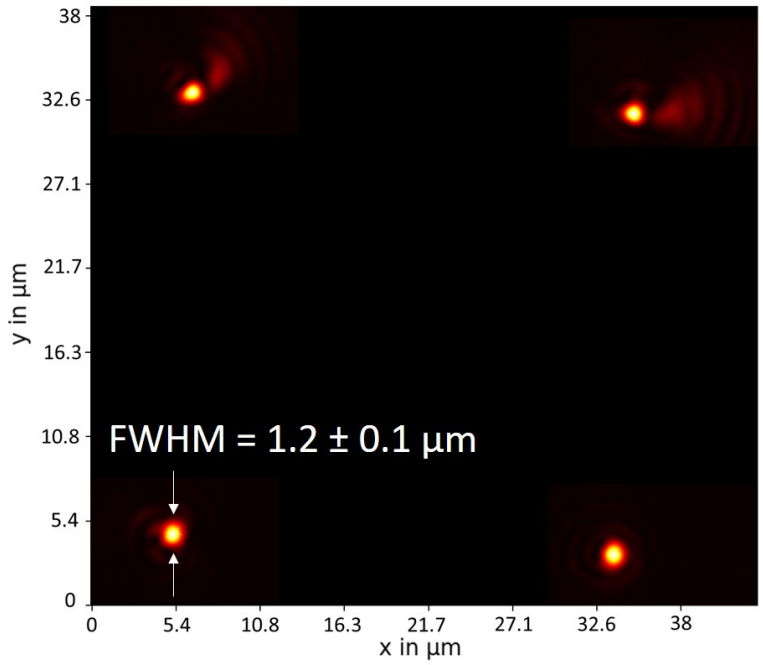

Figure 3.15: 4-core fiber characterization at 1550 nm of lensed fiber from figure 2.21 (b)

figure 2.21 (c).

At 1550 nm:
The characterization of fiber 37.1 at 1550 nm shown in figure 3.16 (b); reveals that

the cores are single-mode and have a MFD of 7.5 ± 0.1 µm.

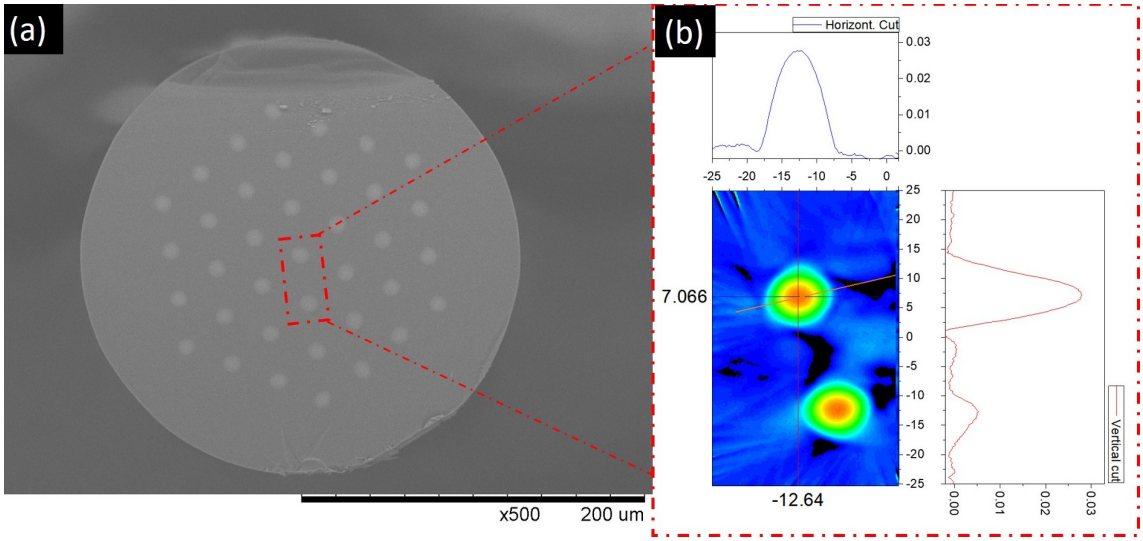

Figure 3.16: (a) Top view of the 37 core fiber facet. (b) Output beam without lens at 1550nm. MFD = 7.5 ± 0.1 µm.

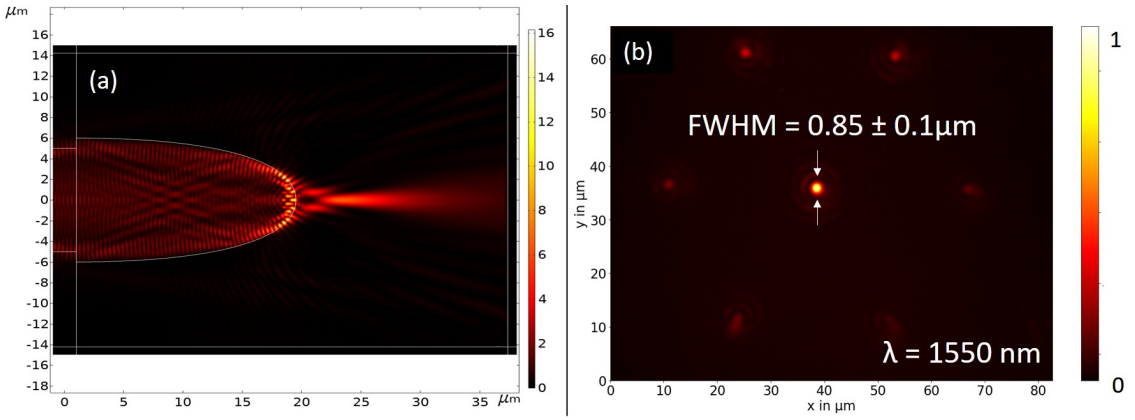

Figure 3.17: (a) Simulated intensity distribution for the fundamental mode of a 10 µm core at 1550 nm with a micro-lens. The lens base, height and Bézier weight W are 12 µm, 18.5 µm and 0.914, respectively. . FWHM = 0.84 µm. (b) Experimental characterization of the focused spot from one core with a micro-lens: FWHM = 0.85 ± 0.1 µm.

The simulation of a 10 µm core excited by its fundamental mode at 1550 nm with a PDMS micro-lens similar to the one achieved on the fiber 37.1 is shown in figure 3.17 (a). The micro- lens has a base and height of 12 and 18.5 µm respectively and a Bézier weight W of 0.914. The focused beam has a FWHM of 0.84 µm. This is in good agreement with what has been experimentally measured, as illustrated in figure 3.17 (b). A small portion of the light seems to travel along the surrounding cores, which may be due to the cross talk between the cores.

At 1070 nm:
Similarly, we see at 1070 nm, as represented in figure 3.18 (a) and (b), a good

agreement between the numerical and experimental assessment of the generated focus spots FWHM at the output of one of the 37 lensed cores.

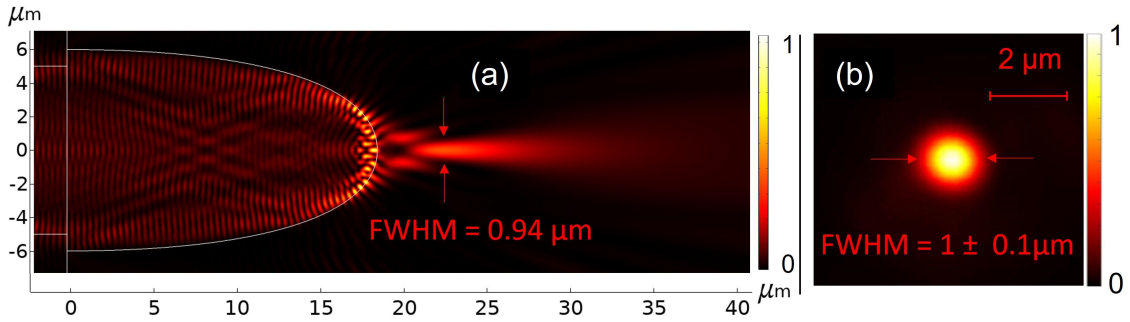

Figure 3.18: (a) Simulated intensity distribution for the fundamental mode of a 4 µm core at 1070 nm with a micro-lens. The lens is as in figure 3.17. FWHM = 0.94 µm. (b) Experimental characterization of the focused spot from one core with a micro-lens: FWHM = 1 ± 0.1 µm.

At 633 nm:
The non-lensed and lensed 37.1 fiber characterization at 633 nm show a proper alignment between the micro-lens array and the 37 fiber cores. That can be seen in figure 3.19 (b) where a clear focusing of the outgoing beam is observed when compared to figure 3.19 (a).

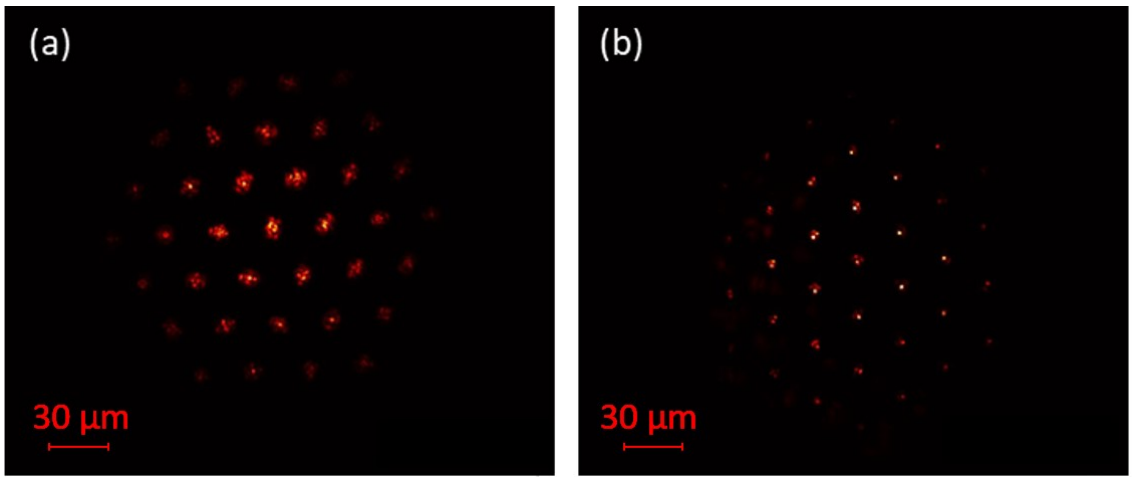

Figure 3.19: Output intensity measurement from the 37 core fiber by global injection at 633 nm: (a) with, versus (b) without micro-lens array. Fiber 37.1.

3.3 Conclusion

In this chapter, we have studied the numerical design and the experimental characterization of the newly fabricated micro-lenses introduced in the previous chapter. The objective was to evaluate the focusing and collimating capabilities of these micro-lenses when light emerges from the lensed fiber.

To study the micro-lens design, I have utilized the COMSOL Multiphysics software. For comparison experimental measurements have been conducted. We have also investigated theoretically the impact of micro-lens misalignment and the potential of using a coating material to reduce reflections.

The micro-lens design depends on the application. Different applications impose specific constraints, such as beam diameter, WD, or depth of field requirements. The choice of optical fiber also influences the micro-lens design, as different fibers have different core sizes, MFDs, and cut-off wavelengths. To simplify the study without compromising accuracy, we have considered few selected fibers and wavelengths. The shapes of our aspherical micro-lenses have been described using Bézier curves.

The effect of each parameter on the outgoing beam has been investigate. The Bézier weight of the micro-lens, showed a linear dependency with the beam's WD and full width at half maximum (FWHM). A higher Bézier weight resulted in an extended depth of field but compromised the strong focusing capabilities, while a smaller Bézier weight (sharper tip) led to intense focusing at smaller WD.

Furthermore, we investigated the influence of the polymer spacer that we can fabricate with our technique. The spacer introduces flexibility in the design, enabling a combination of long WD and small beam FWHM, which was not possible with the micro-lens alone.

Reflection losses, especially at small Bézier weights, have been studied numerically. They can cause high intensity local maxima inside the micro-lens. To mitigate these reflections and protect the micro-lens, an AR coating has been proposed. The coating's refractive index was calculated based on the micro-lens and surrounding medium indexes as for a flat interface. Applying theoretically the AR coating, reduces the losses by 5% on average. This will have to be validated experimentally in the future.

Considering the practical limitations of micro-lenses alignment, slight deviations may occur. For this reason, we studied the effect of micro-lens misalignment that in turn deviates the emerging beam. The relation between the micro-lens shift and the beam deflection angle has been studied. This allow the determination of the tolerance for misalignment to ensure acceptable performances. Deflection angles of 1.4 degrees, considered acceptable based on literature, corresponds to a $\pm$ 0.8 µm misalignment tolerance during the fabrication's alignment procedure on a SMF28.

Then the fabricated micro-lenses for both single and multi-core fibers have been characterized experimentally. The experimental results, compared with the numerical simulations, are in good agreement. The measured beam widths and depth of field match the simulated values, confirming the accuracy of the simulation model and of the fabrication method. With different lenses, focus spot with a FWHM of around 1 µm in near infrared has been demonstrated as well as a 30 µm collimation of a 3.3 µm FWHM beam. For multi-core fiber characterization, two injection techniques have been discussed: injecting light into each core individually and using an SLM for multi-core parallel excitation. The first technique has been implemented for the measurements, wheras the SLM-based method still have to be optimized. The experimental measurements of a 4-core fiber at 1070 and 1550 nm demonstrate the successful focusing of each core using the micro-lens array. However, some imperfections are observed, which may be due to mode of the lens, which was probably too long. However, the experimental measurements of the MCF with 37-core fiber with

the array of 37 micro-lenses are in good agreement with the COMSOL simulation results with sub-wavelength focusing.

We think that this chapter provides valuable insights into the numerical design and experimental characterization of the micro-lenses fabricated by the proposed method. This will contribute to implementations in various optical applications and lay the groundwork for further optimizations and customization. Some are presented in the next chapter.

Chapter 4

Applications

In the preceding chapters, we have extensively explored the novel micro-lens fabrication technique, which we developed in collaboration with the University of Sétif 1. The discussions covered the micro-lens design and the experimental evaluation of their optical properties, with a focus on both single core and multi-core fibers. Notably, we demonstrated the successful achievement of sub-wavelength focusing and efficient beam collimation using these micro-lenses.

In this chapter, I delve into two specific applications that were the subject of experimentation during my PhD research. The integration of our newly devised micro-lenses into these applications holds significant potential for impactful results. The two applications under consideration are:

1. Mid-IR light coupling from ICLs laser diode into fluoride fibers
2. Silicon laser micro-etching

4.1 Mid-IR laser diode coupling in fluoride fibers

Mid-IR (MIR) laser sources, such as ICL and Quantum cascade Laser (QCL), have recently garnered significant interest due to their high coherence, tunability, efficiency [176], compact size, and wide range of applications [177]. These sources are particularly advantageous for fields like molecular spectroscopy, medical breath analysis, industrial process control and combustion diagnostics, as most gases and liquids exhibit strong absorption bands in the MIR region [178–180]. However, these benefits come with the inconveniences of elliptical beam profiles and uneven divergences, as illustrated in figure 4.1.

This is a result of the asymmetric cavity design required to control the mode structure and promote SM operation, in addition to reducing losses and lasing threshold [181, 182]. Consequently, coupling the light emitted from ICLs and QCLs into optical fibers leads to significant losses, especially in direct coupling configurations where the fiber is placed directly in front of the source emitting area. This configuration is important because it lead to the smallest and most stable packaging of the fibered laser system, as discussed and seen in figure 1.10. Various techniques can enhance the coupling efficiency, such as employing a hollow-core waveguide [183] to correct the beam profile into a single $TEM_{0,0}$ mode. However, even in this case losses stemming from the coupling between the source and the hollow-core waveguide can reach up to 30% [184]. Another proposed solution involves lens-on cap laser

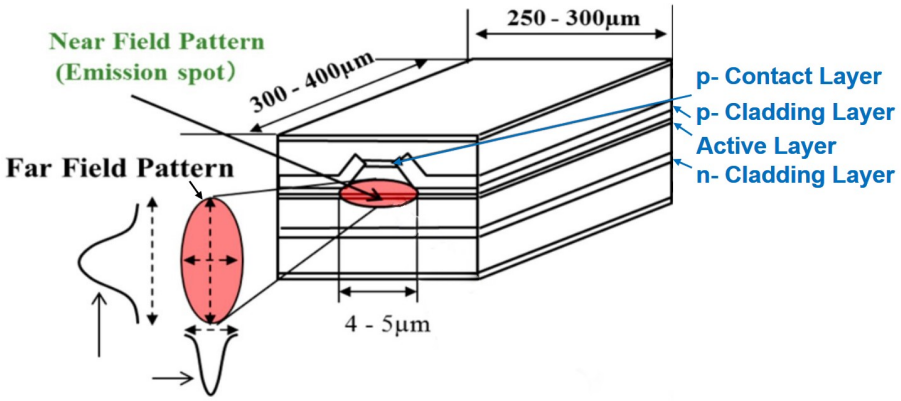

Figure 4.1: Quantum well laser diode. The active layer thickness is usually around 1 µm, hence the emission surface is about $1\mu m\times$ (4 to 5) µm. The beam divergence along the vertical axis is superior to that of the horizontal one, which explains why, the ellipse's major axis switches from being along the horizontal axis in the near field to the vertical axis in the far field. [4]

diodes. The source is focused with a lens into the fiber. However, this approach lacks compactness [185].

4.1.1 Non-silica based fibers - fluoride fibers

The most suitable fibers for guiding MIR wavelengths, to date, are fluoride fibers (2 µm to 7 µm) and chalcogenide fibers (7 µm to 20 µm) [186]. Silica fibers are unsuitable for these wavelength ranges due to their opaqueness after 2.7 µm, rendering them unfit for ICL/QCL sources. Moreover, conventional fiber tip shaping techniques used with silica fibers to improve laser diode coupling, such as electric arc, laser heating, or polishing [187], cannot be employed for fluoride or chalcogenide fibers. Namely, silica fibers possess higher softening temperatures [188] and greater robustness [189] compared to fluoride and chalcogenide fibers.

To overcome these challenges, we propose employing the polymer micro-lenses presented in the previous two chapters. The laser diodes used for this study are ICL sources emitting at wavelengths of 4.53 µm and 5.26 µm, and two fluoride fibers have been considered: a SM 9.5/125 fiber with a 9.5 µm core diameter, and a MM 30/125 fiber with a 30 µm core diameter (125 represents the cladding diameter in µm). The core and cladding indexes and NA of the fiber at the two ICL wavelengths are presented in table 4.1. This study has been done in collaboration with the company LeVerreFluoré, near Renne in France, which is the world leader in fluoride fibers.

Zemax has been used to find the optimal lens shape. As we will see, the coupling efficiency and compactness of this solution surpass those of other currently available techniques in the market [183–185].

Table 4.1: **Indexes and NA at $\lambda = 4.53$ and 5.26 µm of the fluoride SM and MM fibers. The SM 9.5/125 fiber has a 9.5 µm core diameter, while the MM 30/125 fiber has a 30 µm core diameter (125 represents the cladding diameter in µm).**

ICL wavelength	core index	Cladding index	NA
4.53 µm	1.4844	1.4773	0.3
5.26 µm	1.4535	1.4458	0.3

4.1.2 PDMS and NOA61 transmittance

The MIR transmittance of the two polymers (PDMS and NOA61) used in our process have been measured by FT-IR spectroscopy. The results are shown in figure 4.2 for a layer thickness of 20 μm between two CaF_2 substrates.

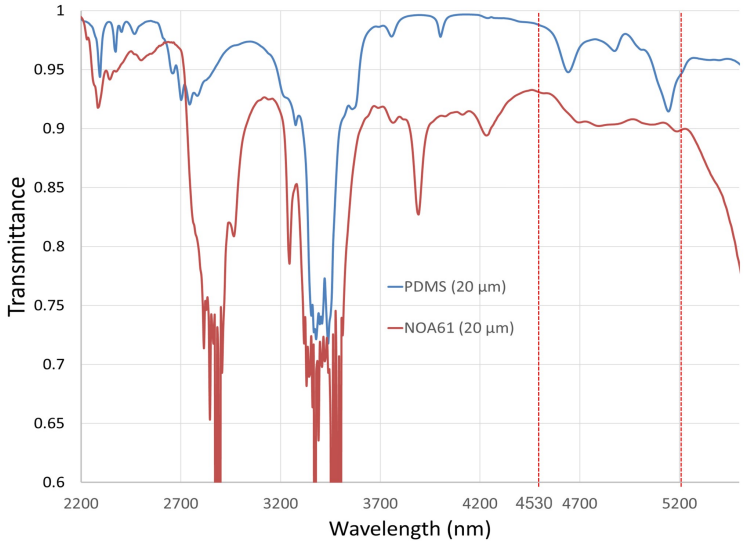

Figure 4.2: FT-IR spectral transmittance of 20 µm PDMS and NOA61 layers sandwiched between two CaF_2 substrates.

Both PDMS and NOA61 have very high transmittance of $\geq 90\%$ over the majority of the spectrum from 2.2 to 5.5 µm, except at around 3.3-3.4 μm where there is a clear absorption peak (due to C-H bonding). NOA61 has an additional absorption peak at around 2.8 μm.

4.1.3 Diode-fiber coupling system description and simulation

To design the micro-lens, a Zemax study has been carried out. Zhiwei HE a master student from Telecom Physique Strasbourg has helped me in this design during his internship at ICube in 2022. Based on the providers information, we know that the ICL laser source has an emitting area of 1 µm $\times 1.3\lambda$ (µm) with 65° and 45° divergence angles respectively [190]. The source was described accordingly in the ray-traced Zemax model. As for the configuration, direct source-fiber coupling was chosen (figure 4.3). This would make for a very compact system and reduces to a

minimum the number of optical components.

It has been found numerically that, the maximum coupling efficiency is only about 57%, for both SM and MM fibers, when the fiber is not equipped with a micro-lens. Experimentally, these values, measured by LeVerreFluoré are 41.5% and 38% for the 9.5/125 and 30/125 fiber, respectively. The difference was expected since, the Fresnel reflections (which amount to around 4% for flat surfaces) are not taken into account in our Zemax model.

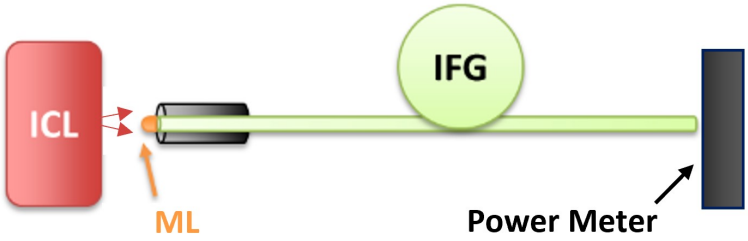

Figure 4.3: ICL direct coupling into fluoride fiber (IFG) configuration. Measurements have been performed with and without the molded micro-lenses. The positioning adjustment of the fiber was performed using a 3D mechanical transation stage.

For the micro-lens design with Zemax, first a hemispherical lens shape and size has been considered to maximize the light coupling into the fibers. The result was then used as a starting point to search for the optimal aspherical lens. This was done to reduce the calculation time since aspherical lenses are described by multiple parameters as seen in equation 3.1.

The index of the micro-lens is 1.43 for PDMS at 4.53 µm [166]. The same calculations have been carried out for NOA61 (index of 1.54 at 4.53 µm). With the hemispherical PDMS micro-lens, a significant increase in the coupling efficiency has been found for a radius of 6.8 µm and 16 µm for the 9.5/125 and 30/125 fiber, respectively, as shown in figure 4.4.

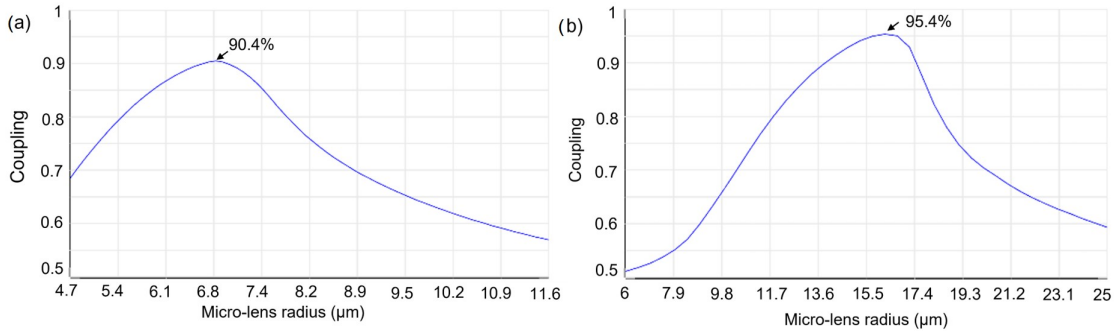

Figure 4.4: Simulated ICL-fiber coupling efficiency vs PDMS hemispherical micro-lens radius using Zemax. The plotted values are those registered at ICL-fiber distances that lead to maximum coupling for each micro-lens radius. (a) 9.5/125 fluoride fiber. (b) 30/125 fluoride fiber . Fresnel reflections are not taken into account.

The calculations of the optimal aspherical lens that followed did not lead to any significant gain compared to the hemispherical shape ($\leq 1\%$), but it showed us that

we have some flexibility over the micro-lens dimensions during the fabrication. For instance, the maximal coupling in a 30/125 fiber is 96.7%. That is achieved using a parabolic lens ($\kappa = -1$) with a 45 µm base, 16 µm height, and a curvature of 16 µm. However, a 96.4% coupling can also be achieved with a hyperbolic micro-lens ($\kappa = -1.5$) that has the same curvature and height but with a base of 50 μm. This information show that we have a tolerance range in the micro-lens fabrication.
More information about the numerical study conducted on Zemax can be found in annex B.

4.1.4 Fabricated micro-lenses and experimental results

We have used both NOA61 and PDMS polymers in the fabrication of the micro-lenses. The Zemax simulations show that there is no significant difference in the coupling efficiencies between the two for the same micro-lens design. For this reason, the material of the micro-lens will not be specified further in the discussion.

The fabricated micro-lenses are shown in figure 4.5. The mold fibers used to create the micro-lenses for the SM fibers in figure 4.5 (a) and (b) is a 50/125 graded index fiber that has been first drawn to a diameter of 30 and 22.5 µm, respectively. Both drawn mold fibers havebeen etched in a 24% HF solution at room temperature for 7.5 minutes. For the micro-lenses in figure 4.5 (c) and (d), their molds have been etched also in a 24% HF solution at room temperature for 25 and 22 minutes, respectively, but the mold fiber used for the micro-lens in (c) was drawn beforehand to a diameter of 78 µm.

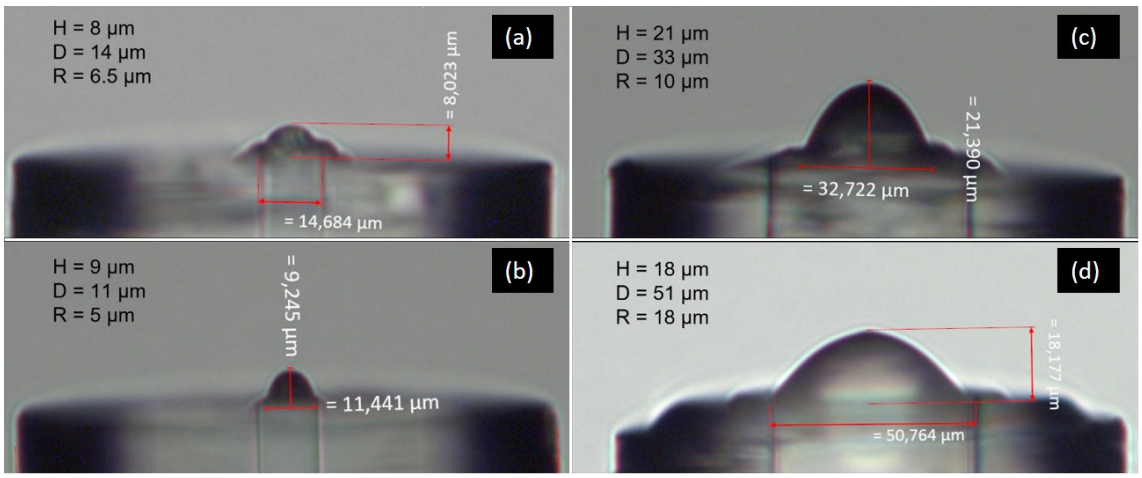

Figure 4.5: Molded micro-lenses on fluoride fiber core with dimensions and curvature close to the optimal values obtained numerically. Fibers are SM (9.5/125) in (a) and (b), and MM (30/125) in (c) and (d).

The experimental evaluation of the coupling efficiency was performed using the same setup described in figure 4.3. The ICL wavelength is 4.53 µm:
- For the 9.5/125 case: two fibers (denoted a and a') with the same micro-lens as the one shown in figure 4.5 (a), and one fiber shown in figure 4.5 (b) (denoted b).
- For the 30/125 case: a fiber (denoted 1) shown in figure 4.5 (c), 4 fibers (denoted 2-5) with the same micro-lens as the one shown in figure 4.5 (d).
The fiber length is 40 cm for all.

Due to the driver current influence on the ICL emission diagram, the optimal coupling values are measured and plotted as a function of the ICL current in figure 4.6.

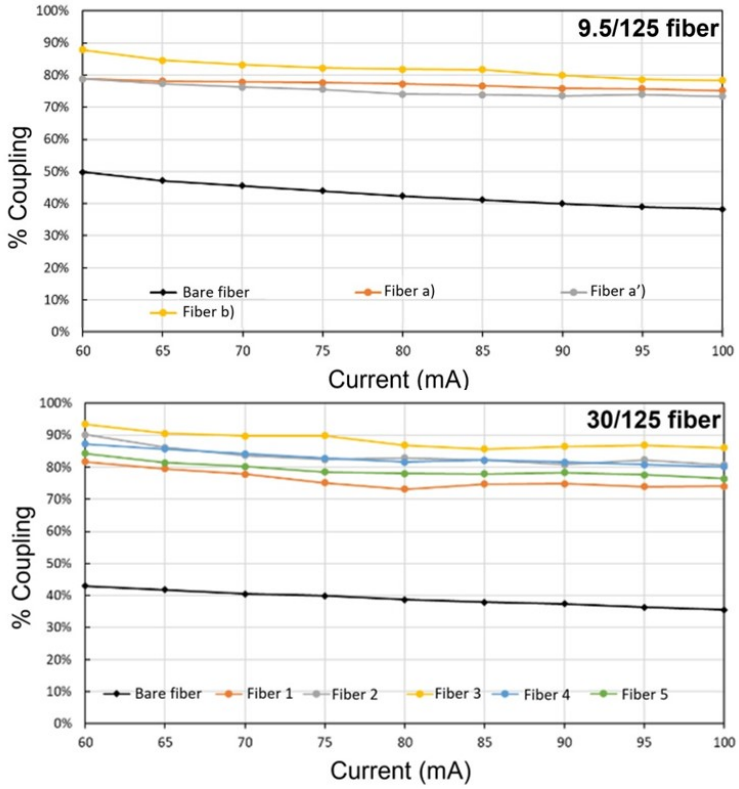

Figure 4.6: Experimental evaluation of the ICL-fiber couplings. The black line represents the coupling without micro-lens (bare fiber). The colored lines represent coupling in several lensed fibers. Top: 9.5/125 fibers with micro-lens shown in figure 4.5 (a-b). Bottom: 30/125 fibers all with the micro-lens shown in figure 4.5 (c-d).

The results show a clear increase in the coupling efficiency for both fibers. The maximum average coupling (yellow line) for a lensed SM fiber is around 82% versus only 41.5% without micro-lens. For lensed MM fibers, the gain is even more pronounced with a maximal coupling efficiency on average (yellow line) of 90%, compared to the 38% without micro-lens.
The highest coupling efficiencies in the case of the SM and MM correspond to micro-lenses with the designs shown in figure 4.5 (b) and (d), respectively.

A summary of the numerical and measured coupling efficiencies for each lens design is presented in table 4.2.

The tests have also been performed with an ICL that emits a wavelength of 5.26 µm. The results showed a 7% and 10% drop in efficiency, for the SM and MM fibers, respectively. These losses do not stem from the micro-lenses, but rather from the increase of the fluoride fiber attenuation from 0.13 dB/m at 4.53 µm to 1.29 dB/m at 5.26 µm. Thus, the attenuation increases from 1.2% at 4.53 µm to 11.2% at 5.26 µm for the considered 40 cm fiber length.

Fiber	Average experimental coupling
9.5/125 bare fiber	41.5%
Fiber (a)	76.5%
Fiber (b)	82.1%
30/125 bare fiber	38%
Fiber (c)	76%
Fiber (d)	83.9%

Table 4.2: Summary of measured average coupling efficiencies for the lensed-fibers shown in figure 4.5.

4.2 Micro-lens power tolerance and laser micro-processing

Laser micro-processing generally requires the use of microscope objectives for high focusing and/or femtosecond lasers to benefit from non-linear absorptions to reduce the etching size [191]. However, more recently, with the introduction of PJs, that are propagative beams concentrated beyond the diffraction limit at the meso-scale from dielectric objects [25, 26], have shown their ability in sub-wavelength surface etching using micro-spheres [192–195]. The primary objective of laser processing with micro-spheres was to achieve sub-diffraction etching resolutions, which are made possible by the generated photonic jets. In laser etching applications, the smaller the beam's cross-sectional area, the higher the optical power density at the material's surface. This increased power density (intensity) enables more precise and controlled material removal, resulting in higher resolution and finer etching patterns. By using micro-spheres to focus the laser beam into a smaller cross section, the optical intensity can be enhanced, allowing for lower power requirements while achieving the desired etching results.

However, as seen in this thesis and in recent research, photonic jets can also be obtained through high curvature shaped fiber tips or micro-lens tips [44, 45, 196]. This suggests that micro-spheres can be substituted by shaped optical fiber tips. They offer advantages such as longer WDs and greater manipulability. Consequently, this substitution can lead to higher or faster etching rates over much larger areas.
To compensate for the lack of manipulability of micro-spheres, array are often used to achieve multi-point etching [39, 193, 197], but the same may be done using lensed MCFs.
The first laser micro-etchings using a fiber tip have been achieved by our team [44, 45] few years ago. Despite the photonic jet being only due to the fundamental mode, it was performed with a MM silica fibers. MMs fibers have been used because it was easier to shape their tip without modifying significantly the fiber core. However, most of the inject power couples to higher modes creating significant losses for the etching process. The first laser etching with a SM has also been performed by our team. It was with a large mode area (LMA) fiber making the fiber tip fabrication easier than a classical SM fiber. However, the low NA of these fibers makes light injection very difficult [11].
The fiber micro-lens fabrication technique proposed in this work, make possible PJ

generation with classical SM fiber. However, since the micro-lenses are made using polymers, it is clearly not obvious if they can be employed in high power laser applications such as laser micro-etching. In this section, we look at the laser damage threshold of the two used polymers (PDMS and NOA61). For that, I have carried out thermal simulations (with COMSOL) followed by experimental tests .

4.2.1 Thermal simulation study

The damages induced to the micro-lens by a high-power laser source is caused by the energy deposition in the material, and this energy when using a continuous or a nano-second laser is primarily related to the absorption, heat conduction and thermal diffusion processes [198]. The relatively long pulse duration (in comparison to a femtosecond laser) allows the heat to be spread and dissipated into the surrounding material, leading to a larger heat-affected zone. This can result in thermal damage to the material, such as melting, vaporization, or unwanted structural changes.
To model these thermal effects on the fiber polymer micro-lenses, I have used the COMSOL heat transfer module. Since the fibers and the micro-lenses are axisymmetric, a 2D axisymmetric model can be used, thus significantly reducing the computing times. The dimensions and absorption coefficient of each of the materials constituting the system must be introduced. These values are summarized in table 4.3. The absorption coefficient denoted α can be derived from the imaginary index denoted κ (otherwise known as extinction coefficient) using the relationship: $\alpha = \frac{4\pi\kappa}{\lambda}$, where λ is the free space wavelength (1.07 µm in our case). NOA61's extinction coefficient has not been found in the literature, this is why the numerical study was only be carried out on PDMS.

Parameter	**Value**
Fiber diameter	125 µm
Fiber length	30 µm
Fiber core diameter	9.5 µm for SM fiber and 50 µm for MM fiber
κ_{PDMS}	2.52×10^{-6} [166]
Index of refraction n_{PDMS}	1.3882
Micro-lens base, height and W	Variables
Specific heat capacity of PDMS	$1670 J/kgK$ [199]
Specific heat capacity of silica	$703 J/kgK$ [200]

Table 4.3: Parameters used in the COMSOL heat transfer model. A silica fiber is considered.

In our model, seen in figure 4.7, the micro-lens is set on a silica fiber core, and the surrounding medium is air. Air is known to have a poor thermal conductivity between 2.623 and $6.763 \times 10^{-2} W m^{-1} K^{-1}$ [201].

The heat source in the model is only inside the micro-lens at the interface with the fiber. We only take into account the fundamental mode in case of a multi-mode fiber, the reason why the source will be described by a Gaussian profile (equation

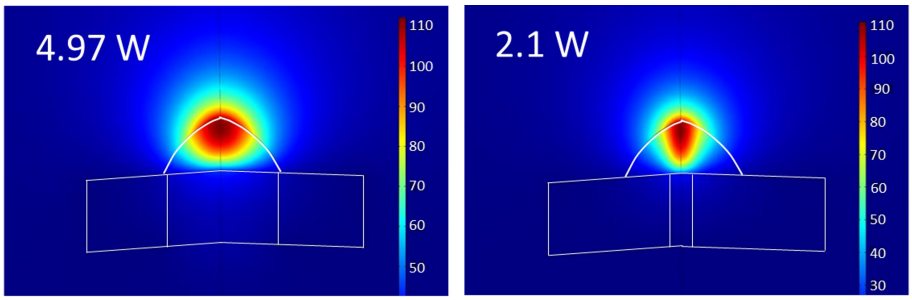

Figure 4.7: Temperature distribution simulation in the fiber/micro-lens/air system for the fundamental mode (CW) at 1070 nm. Left: 50/125 MM fiber. Right; 9.5/125 SM fiber. Incident power has been adapted to reach 110°C. Micro-lens has a 51.5 µm base diameter, 22 µm height and an W = 0.35.

4.2) as the fundamental mode of the optical fiber. The beam intensity absorption respects the Beer-Lambert law (equation 4.1) along the propagation axis [202]. The waist of the Gaussian (denoted ω_0) and its evolution in space is given by: $w(z) = \omega_0\sqrt{1 + (\frac{z}{z_0})^2}$ with z_0 the Rayleigh length. ω_0 of the beam emerging from the fiber into the micro-lens is approximately equivalent to half of the MFD seen in equation 1.9, since the MFD and ω_0 are about 4σ and 2σ, respectively. σ being the standard deviation of the Gaussian intensity profile.

$$I_s = e^{-\alpha z} I_i \tag{4.1}$$

where I_s is the beam intensity at a position z inside the micro-lens, I_i the intensity at the interface fiber/micro-lens and α the polymer absorption coefficient. The power density absorbed by the micro-lens is $\alpha.I_s$.

$$I_i = I_0.exp(\frac{-2r^2}{\omega^2}) \tag{4.2}$$

I_0 being the initial maximum intensity of the beam taken at the interface between the fiber and the micro-lens.

The incident laser power P is expressed in equation 4.3.

$$P = \iint_S I_i ds \tag{4.3}$$

where S is the cross-sectional surface of the beam.

By replacing I_i in 4.3 by its expression in 4.2, we get:

$$P = \iint_S I_0.exp(-\frac{2r^2}{\omega^2}) ds$$

Therefore, $I_0 = \frac{2P}{\pi\omega^2}$.

Figure 4.8 (a) and (b), depict the effects of the height and the base diameter of the micro-lens, respectively, on the maximum reached temperature due to a 2.5 W mean power continuous wave source. When lens height is varied, the base diameter is

kept constant to 10.5 µm, and vice versa (height = 15 µm). The results in figure 4.8 (a) show a clear dependency on the height of the micro-lens. Higher temperatures are reached with longer lenses. In contrast, the base diameter was expected to limit the maximum temperature of the micro-lens as it increases, since it allow the heat to spread and to be dissipate more easily, but this effect turned out to be almost negligible as seen in figure 4.8 (b).
Another information deduced from figure 4.7, is that larger fiber cores, require much higher mean laser powers to get the micro-lens to the same temperature . This is because larger fiber cores, lead to larger beams and thus lower power densities. We also see that the temperature is maximum at the micro-lens tip (apex). It is probably due to the thermal conductivity of the air that is much lower than that of the silica fiber.

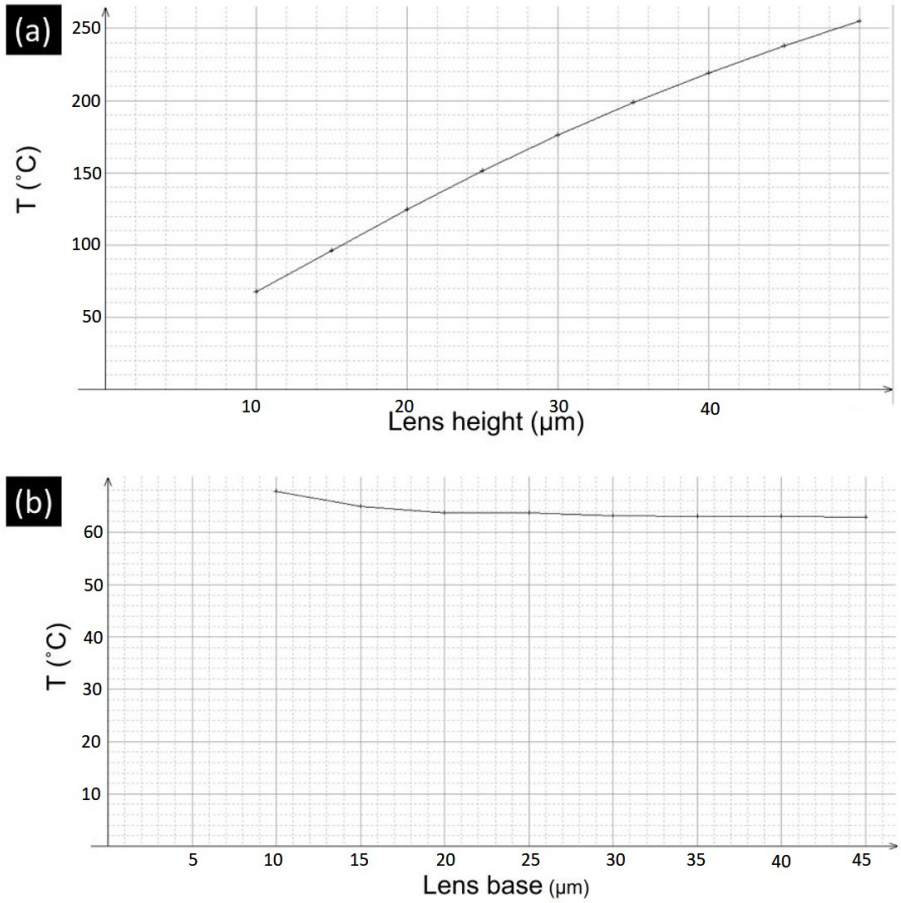

Figure 4.8: Maximum temperature variation as function of the PDMS micro-lens's: (a) height, with base fixed at 10.5 µm; (b) base diameter, with height fixed at 15 µm. The W is 0.5 and the mean power is 2.5 W in both cases. The fiber is a SM fiber with a 9.5 µm core diameter.

To determine the damage threshold from the numerical simulations, we need to know the temperature at which the PDMS properties start to change or when it gets damaged. M. Liu et al. demonstrate that the PDMS thermal decomposition start at 200°C and reaches a peak at 310°C[203]. However, we also know from H. Huang et al. that in pulse regime the ablation threshold of PDMS decreases when the number of laser pulses increases [204]. Beyond a given fluence value, the PDMS,

although does not get instantly damaged, its absorption starts to increase and even visually, the PDMS turns darker, until the absorption becomes sufficient to ablate the PDMS. So a lowest temperature limit of (200°C) may be considered for maximum longevity of the PDMS micro-lens.

The evolution of the maximum temperature as a function of the laser power for two different PDMS micro-lens heights has been simulated, and the results are shown on the graph in figure 4.9. The micro-lenses have a similar base diameter of 50 µm, however the height is 22 for one and 31 for the other. As a result W varies a little but as discussed earlier this has little impact on the maximum temperature values.

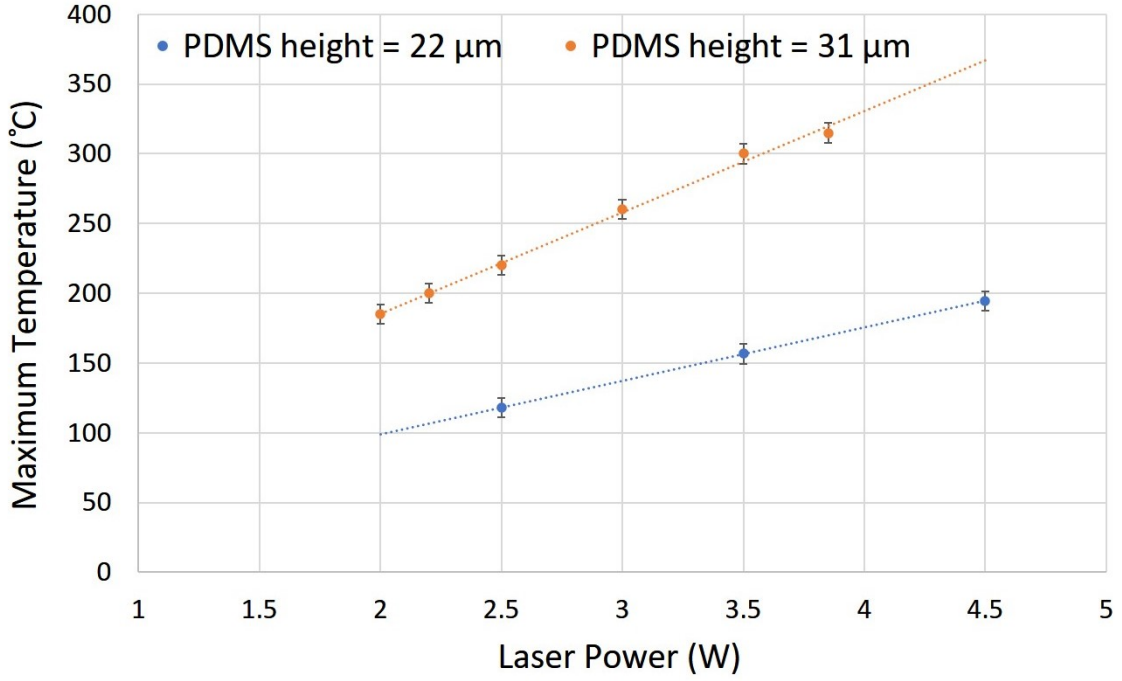

Figure 4.9: Simulation of the evolution of the maximum temperature as a function of the laser power for two PDMS micro-lens heights 22 µm and 31 µm. Base diameter = 50 µm. Fiber SMF28.

From the simulations and considering a temperature limit of (200°C), we can estimate the power threshold of 4.5 and 2.2 W for the micro-lenses with a height of 22 and 31 µm, respectively.

4.2.2 Experimental threshold determination

The tolerance study of the polymer micro-lenses was experimentally conducted using the setup depicted in figure 4.10 (a). This setup consists of three main parts. Firstly, a 4f configuration allows a precise control of the incident laser beam diameter. Secondly, a x50 microscope objective serves both as a focusing lens for the incident beam (red beam in the figure) and as an imaging system for the beam reflected from the surface of the micro-lensed fiber. The back reflected light then travels back through the x50 objective (purple arrows in the figure) and is directed

towards the tube lens and CCD camera using a beam splitter. This constitutes the third part of the system.

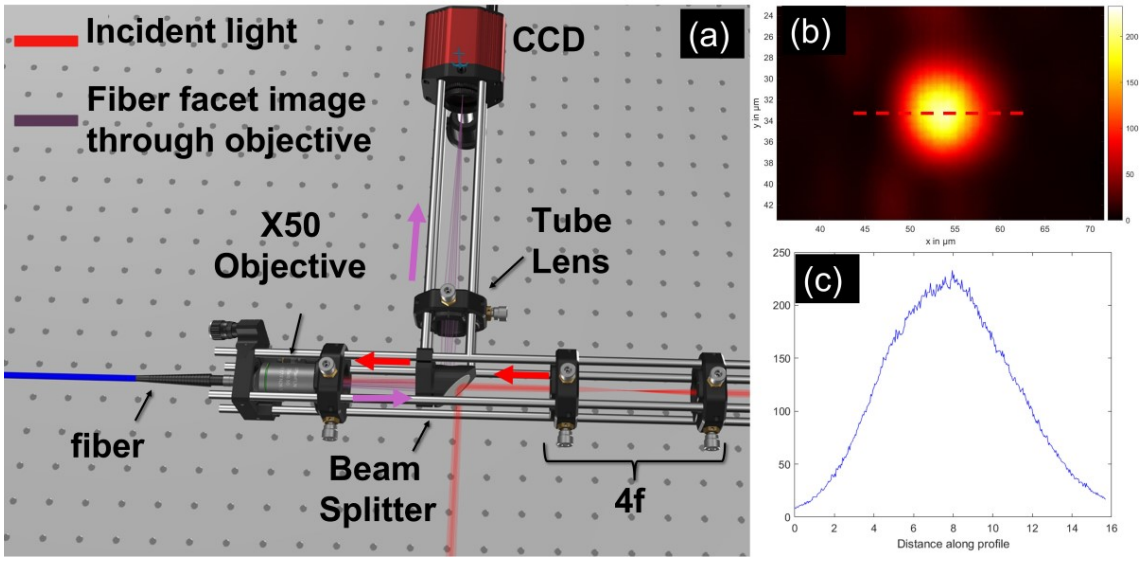

Figure 4.10: (a) Schematic representation of the optical setup used to monitor the micro-lens submitted to a high power laser. (b) Experimental characterization of the beam arriving at the micro-lens tip (focal plane of the microscope objective). (c) Cross section of the beam in (b) showing a FWHM of 7.8 µm.

Note that in this setup, the laser beam is directly focused onto the micro-lens without being injected into the fiber first. This approach has been chosen due to difficulties encountered during the injection process at high laser powers, which led to fluctuations in coupling efficiencies. These fluctuations made it challenging to accurately determine the laser power reaching the micro-lens. Therefore, to ensure precise study and assessment of the incident power, the optical setup has been configured to expose the micro-lens's outer layer directly to a laser beam diameter similar to that generated from an SMF28 fiber, as shown in Figures 4.10 (b) and (c). The beam FWHM is 7.8 µm, and the 1070 nm laser is set to emit 100 ns pulses at a repetition rate of 100 KHz.

Focusing the beam at the micro-lens tip is achieved by moving the fiber to the objective focus plane using the z-stage. When in position, the obtained image is shown in figure 4.11 (c). Moreover, the micro-lens was monitored laterally using a camera and a long WD magnifying objective (not shown in the setup figure). The obtained images are shown in figures 4.11 (a, b) and 4.12 ((a) - (c)).

Once all adjustments are made, the laser power is increased by a small increment (of about 15 mW) after every minute of exposure. The one minute exposure time was chosen because the micro-lens may not be damaged instantly, and needs a few seconds to reach the maximum temperature.

When the power reaches the damage threshold:
- On the lateral camera we see that, in the case of a NOA61, the micro-lens is com-

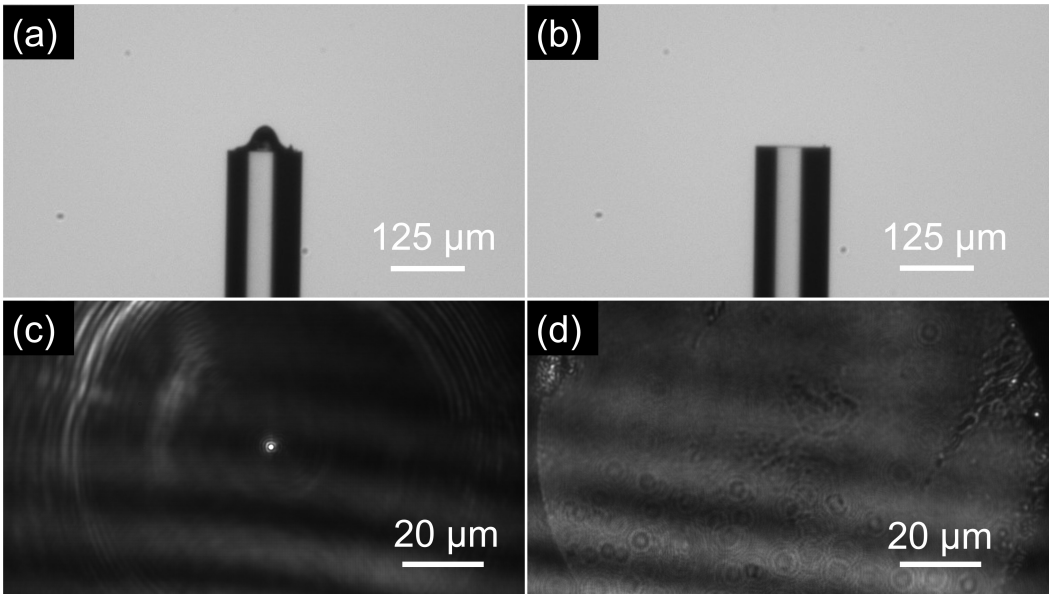

Figure 4.11: Lateral images of the NOA61 micro-lens' state (a) pre and (b) post laser power threshold crossing (5.95W). Top view of the micro-lens tip (a) before and (b) after destroying the micro-lens. 1070 nm, 100 ns, 100 kHz pulse laser focused on the lens with a FWHM of 7.8 µm.

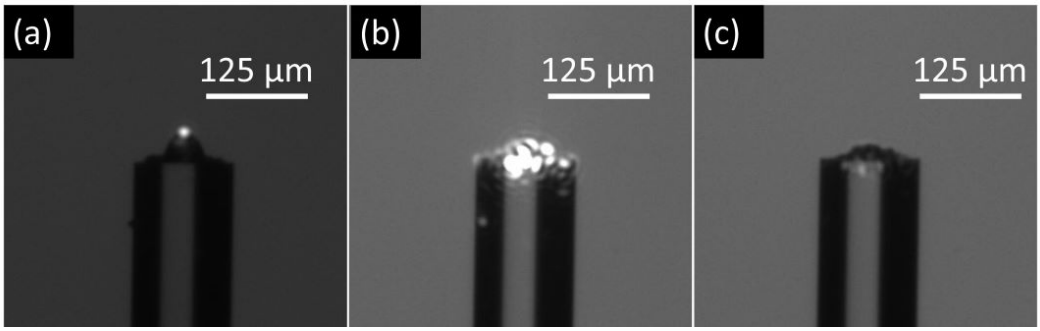

Figure 4.12: Lateral view of the PDMS micro-lens' at: (a) low laser power (200 mW), (b) after destruction at high laser power (3.85 W), (c) after destruction with laser off. 1070 nm, 100 ns, 100 kHz pulse laser focused on the lens with a FWHM of 7.8 µm.

pletely ablated, as shown in figure 4.11 (b), and in the case of PDMS, the micro-lens is totally deformed, as shown in figure 4.12 (c).
- Through the x50 objective and on the CCD camera shown in the experimental setup scheme (figure 4.10 (a)), the bright spot back reflected from the micro-lens tip, seen in figure 4.11 (c), vanishes, and the fiber end appears faintly at an out of focus position as shown in figure 4.11 (d).
- In addition to the above mentioned two observations, we can also monitor the light coupling at the other end of the fiber using a power meter. Figure 4.13 depicts how the coupling efficiency hovers around the 54% value, but at the threshold, which in this case is 3.85 W (for the PDMS micro-lens), the coupling efficiency drastically decreases, reflecting the destruction of the micro-lens.

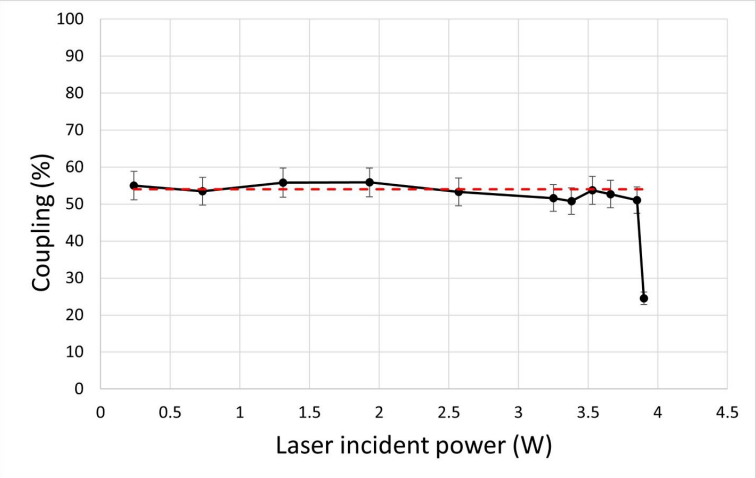

Figure 4.13: Fiber coupling equipped with a PDMS micro-lens at the entrance as a function of incident laser power. The coupling drops dramatically at 3.85 W due to the micro-lens damage. 1070 nm, 100 ns, 100 kHz pulse laser focused on the lens with a FWHM of 7.8 µm.

The micro-lenses chosen for this study have a base diameter and height of 50 and 31 µm, respectively, and a W= 0.49, (the same design as the lens presented in figure 3.5). Three NOA61 and three PDMS lenses were tested to ensure repeatability. The PDMS micro-lenses consistently maintained a power threshold of approximately 3.85 W. By comparing this value to what was obtained numerically, despite the different laser illumination, we see that it leads to a PDMS temperature of 310°C, which corresponds to the upper limit of PDMS degradation. Even-though the micro-lens held up to 3.85 W during the one minute tests, as discussed earlier, it is better to stay below $200°C$, that is 2.2W for maximum longevity of the micro-lens having a 31 µm height.

On the other hand, the NOA61 lenses demonstrated a larger power threshold up to 5.95W. It is not easy to definitively conclude why NOA61 can withstand more power than PDMS since both materials exhibit very low absorption in the near IR region [154, 166]. Additionally, PDMS is known to tolerate higher temperatures, as discussed in Table 2.1. However, it is possible that NOA61 possesses a higher thermal conductivity (although there is no evidence in the literature regarding the thermal conductivity of NOA61, whereas PDMS is known to have very poor thermal conductivity [199]), limiting it to effectively dissipate and distribute heat throughout the entire micro-lens. This may also explain why the NOA61 micro-lens is completely ablated after crossing the damage threshold (Figure 4.11 (b)), whereas a significant portion of the PDMS micro-lens remains (Figure 4.12 (c)). The SEM image of a damaged PDMS micro-lens show in figure 4.14 provides an additional validation to this hypothesis.

We also noticed that NOA61 micro-lenses that are not fully cured (curing time $\leq$ 5 minutes), have a much lower damage thresholds (4.6 W when cured for 4 minutes). Thus it is advisable to cure for 10 minutes for maximum tolerance.

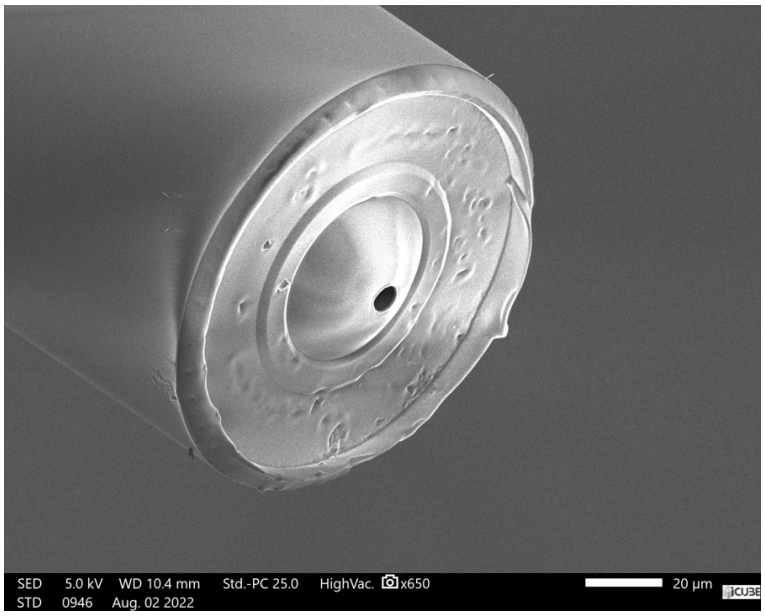

Figure 4.14: SEM image of the punctured PDMS lens at 4 W laser power at 1070 nm (100 ns, 100 kHz pulse laser focused on the lens with a FWHM of 7.8 µm).

4.2.3 Silicon etching

The results of the polymer micro-lens tolerance have given us confidence in their suitability for silicon etching. The relatively high damage threshold of the two polymer micro-lenses is due to both their low absorption coefficients and the small length of the micro-lenses. Previous work conducted by R. Pierron in our group on silicon wafer etching using MM and LMA fibers with shaped tips by electric arcing has determined an ablation threshold of approximately 42 mW with a beam FWHM = 0.8 µm. However, we have demonstrated that the 31 µm polymer micro-lenses can withstand at least 2.2 W for PDMS and even higher for NOA61, for a beam with a diameter close to that of a SMF28 fiber. Therefore, these polymer micro-lenses can be used for silicon micro-etching with minimal risk to the lens.

To demonstrate this, I have considered an SMF28 fiber with three different lens designs denoted as L1, L2, and L3. The first design (L1) is shown in figure 3.9 (a), the second design (L2) is depicted in figure 4.15 (a) and is also the same as that shown in figure 3.10 (a), and the third design (L3) is illustrated in figure 4.16 (a) with its corresponding simulation displayed in figure 3.5 (b).

Micro-lens (L1) made from PDMS, has a very short working distance of 6 µm and focuses on 1 µm FWHM spot (figure 3.4). It is not possible to etch silicon with this lens as it has been damaged during the etching by the plume sputtering from the surface. Micro-lenses with longer working distances are required.

Micro-lens (L2) also made from PDMS has a working distance of 45 µm, and the beam maintained an almost constant diameter over a length of 30 µm, as shown in the simulation in figure 3.10 (b). The fiber position with respect to the silicon surface during etching is depicted in figure 4.15 (a).

The full width at half maximum FWHM of the focused spot is 3.3 µm, as demon-

strated in figure 3.10 (b) and (c). At a measured laser power of 59.5 mW, equivalent to 1.7 µJ per pulse energy for a 100 ns pulse duration and 35 KHz repetition rate, I have achieved the etched line on the left in figure 4.15 (c) as well as the smallest dots at the bottom of figure 4.15 (b). We observed that when the laser power was nearly equal to the ablation threshold, the etched diameters were similar to the FWHM. Higher power results in larger etched diameter.

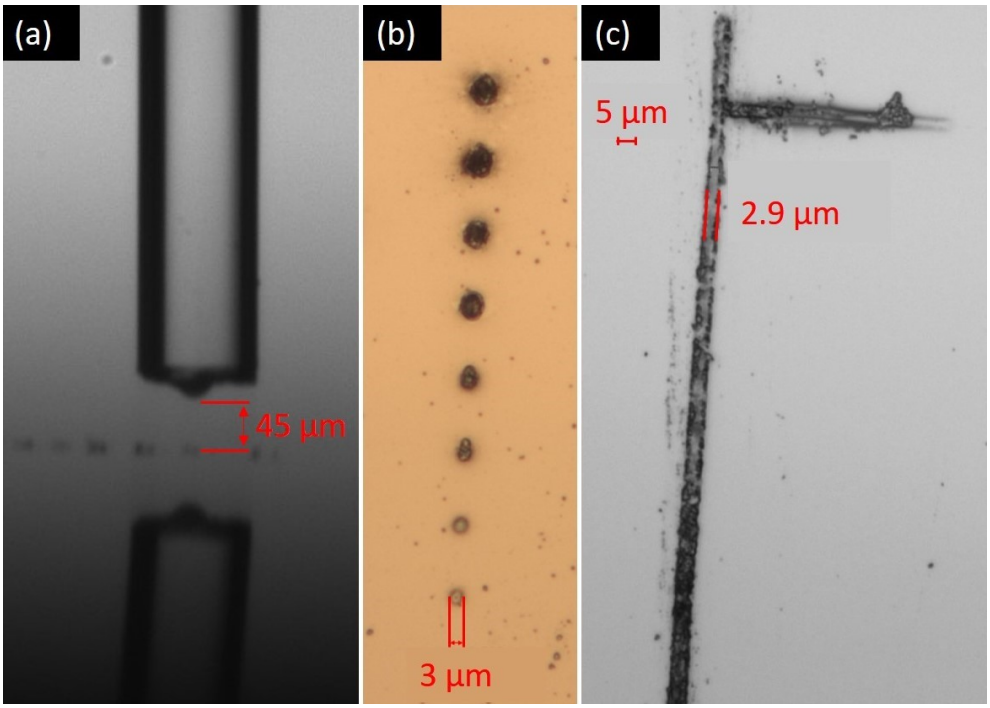

Figure 4.15: (a) SMF28 with micro-lens L2 in front to the silicon surface (a mirror image of the fiber is visible). (b) and (c) are etched dots and lines on silicon using 100 ns, 35 kHz, laser pulses at 1070 nm.

Micro-lens (L3) consists of a micro-lens with the same dimensions as shown in 2.11 (b) deposited on a 200 µm spacer. Both the micro-lens and the spacer are made of NOA61. The image of the fiber tip, and the experimental evaluation of the FWHM of the focus spot are represented in figure 4.16 (a)(b) and (c). The beam's FWHM is 1.5 µm for a wavelength of 1070 nm. The importance of this case is to demonstrate that even with an extended polymer length, which results in higher laser power absorption, the lens is not damaged during the silicon etching procedure. Moreover, another advantage is that due to the higher focusing capability compared to (L2), even weaker laser power is required for etching. Figure 4.16 (d) shows the fiber's in front of the silicon wafer. Figures 4.16 (e) and (f) depict etched lines and dots. For the line in (e), the translation stage's speed has been set at 400 µm per second ($400\mu m/s$). For the dots, the pulse duration was set to 1 ms, which means that for a 35 KHz repetition rate, the number of pulses is around 35 (we cannot get a smaller number due to the pulse duration being limited to 1 ms). The laser power has been increased from 7.7 to 15.2 mW in increments of 2.5 mW. At 7.7 mW, the power is not sufficient to etch the surface, but at 10.2 mW, a dot with a 2.1 µm width is obtained. This indicates that the etching threshold lies between 7.7 and 10.2 mW.

With this, we have demonstrated that the damage threshold of our polymer micro-lenses exceeds the requirements for silicon wafer surface micro-etching, even when the polymer length exceeds 200 µm. Therefore, this procedure is valid for laser processing of silicon surface, as well as many metals such as aluminum, copper, gold, and silver since silicon has a relatively high ablation threshold in the near Infra-red (IR) region compared to many other metals [205, 206].

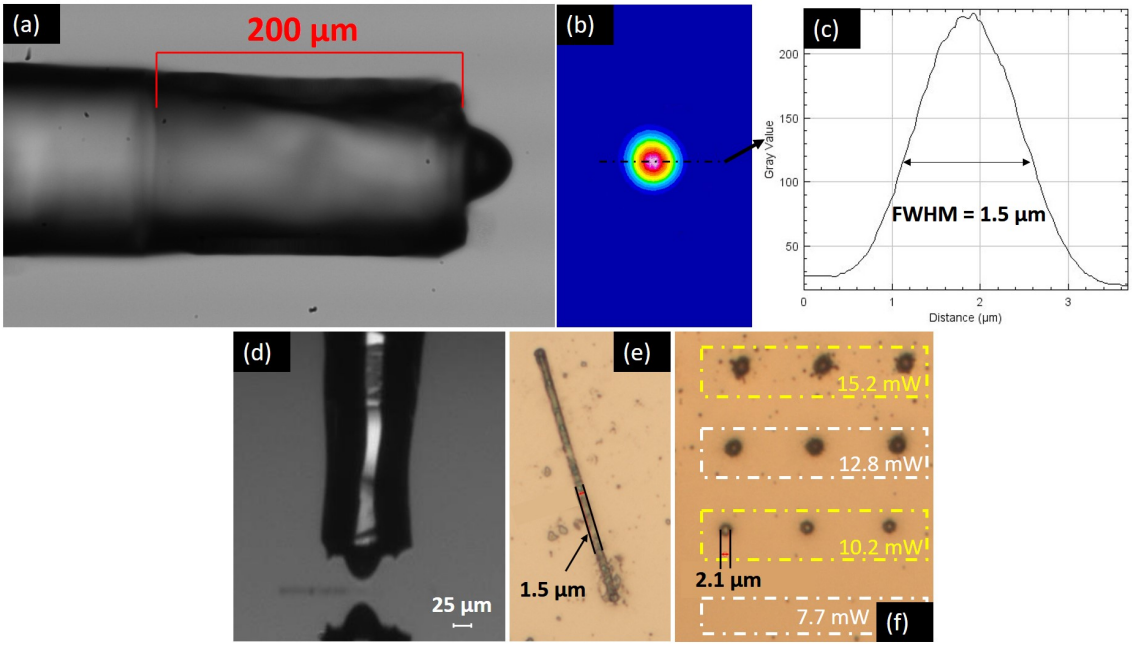

Figure 4.16: (a) Micro-lens (L3) with 200 µm spacer in NOA61. The focus spot profile and cross-sectional plot are represented in (b) and (c). (d) Micro-lens in front to the silicon surface (a mirror image of the fiber is visible). (e) Etched line at 10.2 mW and $400\mu m/s$. (f) Etched dots (1 ms) with laser power from 7.7 to 15.2 mW. 100 ns, 35 kHz, laser pulses at 1070 nm.

4.3 Conclusion

In this chapter the problem of coupling Mid-IR light generated from ICL sources into fluoride fiber which are non-silica fibers has been addressed. The molded high curvature core-aligned micro-lenses fabrication method, proposed in the previous chapters, can be used to deposit micro-lenses on these fibers. This is an important achievement since there was no suitable micro-lens fabrication techniques for this kind of fibers. The design of the micro-lens has been performed using Zemax. PDMS and NOA61 polymers transmittance measurements showed high transparency ($\geq$ 90% for thickness of 20 µm) over the mid-IR spectrum (with the exception of a few absorption peaks). Various micro-lens with dimensions close to what has been obtained numerically, have been fabricated for SM and MM fluoride fibers then tested using two divergent ICL emitting at wavelengths of 4.53 and 5.26 µm. The coupling due to the micro-lenses, increases by around a factor of 2, with residual loss less than 1.1 dB for the SM fiber, and less than 0.5 dB for the MM fiber.

Furthermore, we explored the power tolerance of our micro-lens. One potential application is laser processing, specifically laser micro-etching. To assess the laser power tolerance of the micro-lenses, both numerical simulations using COMSOL and experimental studies have been conducted. The COMSOL simulations have been used to investigate the thermal effects on the micro-lenses by modeling heat transfer and laser absorption. The results show that the maximum temperature reached by the micro-lenses depended on their dimensions. Height has a significant impact. The simulations provid insights into the power threshold of the micro-lenses. A maximum laser mean power of 2.2 W for a 31 µm high PDMS micro-lens and 4.5 W for a 22 µm high PDMS micro-lens should be respected to keep the temperature below the 200°C for maximum longevity.

Experimental studies have been performed to verify the power tolerance of the micro-lenses. The results demonstrate that a 31 µm high PDMS micro-lens could tolerate power levels up to 3.85 W, but it is better not to go above 2.2 W to avoid any thermal decomposition. NOA61 micro-lenses endure higher power levels up to 5.95 W for the same height. These relative high damage thresholds are due to both the small absorption coefficient of the two polymers and the small length of the micro-lenses.

The feasibility of using the polymer micro-lenses for silicon wafer micro-etching has been investigated. The experiments show that the polymer micro-lenses could withstand power levels orders of magnitude higher than the ablation threshold of silicon. Different micro-lens designs have been tested, demonstrating successful micro-etching of silicon surfaces. This established the viability and effectiveness of micro-lens equipped optical fibers for laser processing applications for various materials since the polymer micro-lenses offer greater manipulability and longer working distances compared to traditional micro-sphere assisted laser processing techniques.

General Conclusion and perspectives

The objective of my PhD research project has been to further develop and investigate new possibilities of implementation of a molded polymer-based micro-lens fabrication technique for optical fibers. The technique has been introduced and patented by our group at ICube in collaboration with Sétif University just before my PhD. I have first rebuilt an improved fabrication setup. Then, and due to the promising results obtained for classical single core silica fibers, the project's goal has later shifted to the adaptation of the fabrication technique for non-traditional optical fibers. This includes fluoride-based fibers, which belong to the category of non-silica-based fibers, as well as multi-core and micro-structured fibers.

The motivation behind this project comes from the increasing demand for improved light focusing and light coupling tools in guided-wave optics. The application may concern light coupling in photonics integrated circuits, efficient laser microprocessing and non-invasive endoscopic medical imaging techniques, etc. that offer high resolution and greater manipulability. Micro-lenses can also hold great potential to enhance the performance and integration of non-conventional fibers in various fields. For example, in the case of multi-core fibers, enabling multi-point sensing or processing capabilities and facilitating higher telecommunication data loads. Furthermore, non-silica-based fibers have shown great promises in mid-infrared (MIR) sensing applications. Recently, MIR sensing has gained significant attention due to its effectiveness to detect harmful gases and its potential for enabling communication at wavelengths beyond those already saturated in the telecommunication spectrum. Micro-lenses are difficult to fabricate on most of these micro-structured and/or non-silica fibers.

This PhD thesis report was decomposed in four main parts. The first chapter has been dedicated to the state of the art. Our micro-lenses fabrication technique has been described in the second chapter. The third chapter deals with the numerical study of the micro-lenses' performance using COMSOL Multiphysics and the experimental characterization of the generated beams. Finally two applications have been detailed in chapter four: the fabrication of micro-lenses onto fluoride fibers for MIR ICL laser diode coupling and silicon surface laser micro-etching using photonic nano-jet

The state-of-the-art deals with the origin and evolution of the main fiber micro-lens fabrication techniques, their limitations, and the applications they were tailored

for. In general, classical techniques like electric arcing, chemical etching, thermal melting and drawing provide limited control over the curvature of the fiber tip and are incompatible with non-silica fibers. High curvature micro-lenses are also not possible. On the other hand, more recent techniques like photolithography or two-photon photo-polymerization offer excellent performance and even enable the fabrication of diffractive micro-lenses or meta-lenses. However, these methods are time-consuming, not applicable for large-scale production, and often require expensive and sophisticated equipment. These limitations highlight the need for more advanced and precise fabrication methods to overcome these challenges. The development of innovative techniques that offer better control over the curvature of the fiber tip while remaining compatible with non-silica fibers is a significant focus of current research. Additionally, there is a growing demand of fabrication techniques that strike a balance between performance and scalability, allowing efficient and cost-effective production on industrial scale.

In the first part of my PhD project, I have constructed a new improved setup to fabricate the proposed micro-lenses. This is described in chapter two. The micro-lenses are fabricated using polymer by molding. NOA and PDMS have been tested during this work. The mold is etched by Hydrofluoric acid in the core of an optical fiber. The shape depends on the fiber doping profile. Three fiber holders are used, the first which is the one to hold the fiber that is equipped with the micro-lens, is mounted on a fixed support; this has been later replaced by a rotation mount to add the degree of freedom allowing the alignment of the multi-core fibers. The second holder is mounted on a 5D motion stage to allow a perfect optical alignment between the mold and the first fiber. In other words, this allows for the micro-lens to be aligned on the fiber core. The third fiber holder purpose is to bring forward the polymer droplets set on a third fiber, and this holder is mounted on a one directional translation stage. In addition to the fiber holders and mounts, two cameras with magnifying objectives are installed for the visualization from two orthogonal directions. For polymer curing, a $200°C$ heat source and a UV source are also integrated, and we found that the optimal pre-curing time for PDMS to be proportional to the cube of the mold volume, and that of NOA61 to be 10 seconds. This setup has been used to fabricate a wide range of micro-lenses with different dimensions. We demonstrate that to obtain small, high curvature parabolic shaped molds suitable for the generation of highly focused beams through single mode fibers, the graded index fibers core diameter must be first reduced. To do that, we have built a home-made melting and drawing device.

We assess the optical quality of the micro-lenses using optical interferometry and scanning electron microscopy, both of which revealed minimal surface roughness. Additionally, thermal cycling tests were performed, and the micro-lenses exhibited excellent durability, showing no signs of deformation or debonding.

Furthermore, we show that our micro-lenses are compatible with non-silica optical fibers, specifically fluoride fibers. I also succeeded in fabricating for the first-time fiber spacers made from the same polymers as that of the micro-lenses with high precision over its length. This is very valuable for non-silica fibers since splicing a

conventional spacer is not an easy task in this case.

By increasing the viscosity of the polymer when inside the fiber mold by pre-curing to approximately 70% of the full pre-curing time, I show that this makes possible to put the mold in contact with micro-structured fibers. Particularly, micro-lenses have been deposited on hollow-core micro-structured fiber and anti-resonant fibers with core diameter of 15 and 30 µm, respectively, without losing the polymer from the mold, and with minimal polymer penetration inside the hollow structure. The pre-curing is then completed, and the mold is released. With this, I prove the compatibility of our fabrication technique with hollow core and micro-structured optical fibers.

Lastly, I succeed to fabricate micro-lens arrays for multi-core fibers. For that, I encountered and resolved several challenges, specifically those related to mold filling and core alignment. I find that it is very hard to prevent the formation of trapped air bubbles inside the mold underneath the polymer. Solving this require the use of a polymer with high gas permeability such as PDMS. The core alignment has been carried out using the coupling efficiency between the mold and target fiber. It is still not very reliable due to various effects such as cross talk, and the different core size between the two fibers. This led to misalignment issues on some fibers, but I managed to get acceptable results on others. We know how to upgrade our alignment system. This can be done using a small prism in between the two fibers to reflect the fiber facet images onto the camera. This has not been done during the PhD due to time constraints. Nevertheless, I have been able to fabricate micro-lens arrays for a 4-cores and a 37-cores fiber. The beams they generate have been characterized and compared to numerical simulations.

The other part of the project consists of a numerical study using COMSOL Multiphysics to gain a deeper understanding of the functionality and performance of the micro-lenses by studying their behavior as a function of their shape and size. This has been described in the first part of chapter three. The study focus on aspects such as focusing capability, working distance, depth of field, and light losses, particularly in the case of single-mode (SM) fibers. We found that high curvature micro-lenses (curvature radius around 10 µm) can generate photonic jets, that is highly focused beams with full width at half maxima of about 1 µm, at a wavelength of 1070 nm. An issue is their limited working distances, smaller than 10 µm. Using lower curvature micro-lenses increases the working distance, but also increases the focus spot size. I show that a solution to this is to add a spacer. I demonstrate that using a 200 µm spacer allows a working distance of 25 µm with the focus spot having a FWHM of 1 µm. This numerical study also reveals that conic micro-lenses (with very high curvature) with sharp edges, lead to losses due to total internal reflections. My simulations show that this could be reduced using an AR coating (losses lowered by about 5%). This issue does not affect the performance of micro-lens used for light collection.

After having studied theoretically the micro-lens design, I rebuilt the fiber micro-lens output beam characterization setup and improved it by adding a 1070 nm

VGEN-C series Ytterbium fiber laser. Previously, the characterization was only possible with a Helium Neons laser (633 nm). This setup has been used to characterize the beams generated from the micro-lensed fiber, including multi-core fibers. This is described in the second part of chapter three. Characterization of the multi-core fibers at 1550 nm has been performed by our partners at the Phlam laboratory. The experimental characterization consisted of determining the FWHM, the depth of field and the centering quality of the micro-lens on the fiber core. This also allows to verify the numerical results.

The last chapter of the thesis report concerns the applications of our polymer micro-lenses. The first application addresses the coupling efficiency improvement between a mid-infrared interband cascade laser (ICL) and both single-mode and multi-mode fluoride fibers. The optimal micro-lens designs has been determined numerically using the Zemax software. The transmittance of our polymers, (PDMS and NOA61) has been measured in the MIR region to assess their suitability. For this particular application, the wavelengths 4.53 and 5.26 µm have been considered. The transmittance measurements, conducted using a FT-IR spectroscope, show that both the polymers exhibit a transmittance of $\geq 90\%$ across the majority of the MIR region for a layer thickness of 20 µm. A significant absorption peak takes place around 3.3 µm, and an additional peak at 2.8 µm specifically for NOA61.

The fabricated micro-lenses, resulted in an almost doubled average coupling efficiency, with some cases achieving a maximum of 90% at low ICL current values.

The second application that I have considered is silicon surface micro-etching. This application involved studying the tolerance of the micro-lenses to high laser powers. For that we conducted numerical thermic simulations on PDMS micro-lenses, and we found two dominant parameters on the maximum reached temperature inside the micro-lens. These parameters are, the fiber core diameter, and the micro-lens height. The first naturally affects the beam mode field diameter and hence the beam power density. The second impacts the total absorbed power. We mainly consider micro-lenses with heights of 31 and 22 µm. Through experimentation, I determined that PDMS can tolerate up to 3.85 W for a 31 µm high micro-lens. According to thermal simulations, this power corresponds to a maximum reached temperature of 310°C, which is in accordance with the literature. However, to prevent any long term degradation, it is preferable to limit the maximum temperature to ≤ 200°C. Based on the simulations, this corresponds to a power limit of 2.2 W. NOA61 has shown experimentally its ability to tolerate up to 5.95 W, which is higher than PDMS, possibly due to its higher thermal conductivity.

These results demonstrate that the micro-lenses have a power tolerance that is order of magnitude higher than the requirement for silicon micro-etching. We successfully used two micro-lensed fibers (one of them has been deposited on a polymer spacer) to etch dots and lines on a silicon wafer surface. The achieved etching size is approximately 1.5 µm and 3 µm.

Looking ahead, several promising avenues for future exploration and improvements emerge from the findings and insights of this study:

- Investigate the impact of slightly shifting the micro-lens position away from the center of the fiber core on coupling efficiency.
- The fabrication of spacers with tilted end facets, which may allow lateral deflection of the beam, may be particularly relevant for many medical applications [207, 208].
- The fabrication of elliptical molds by applying controlled mechanical pressure on the fabricated molds when heated up to the silica softening point, resulting in elliptical micro-lenses. These elliptical micro-lenses have been proven to be even more efficient than hemispherical lenses for laser diode coupling into optical fibers [78, 79].
- The development of techniques for active control of the micro-lens properties, such as focal length or beam steering, to enable dynamic manipulation of light in optical systems [70].
- Applications of micro-lenses in emerging fields, such as quantum optics or nano-photonics [16], to enable novel functionalities and advances in these areas, can be explored.
- The improvement of the multi-core micro-lens array fabrication setup, especially by implementing a prism that enables imaging of the fiber facets, can significantly enhance the core alignment procedure [162].
- The study of the integration of micro-lenses as well as micro-lens arrays on multi-core fibers with advanced imaging systems, such as confocal microscopy or optical coherence tomography, to enhance imaging resolution and depth penetration [209].
- The optimization of the spatial light modulator (SLM) characterization setup to allow homogeneous light injection into each core of the multi-core fibers is crucial for example to enable multi-beam etching. The SLM also allows dynamic turning on and off of each core individually, which is essential in laser processing applications.
- The optimization and fabrication of a micro-lens for a hollow core fiber specifically designed to be used in high signal to noise ratio spectroscopy. It is an important area of future exploration [210].

Appendix A

Coating effect on intensity inside the micro-lens

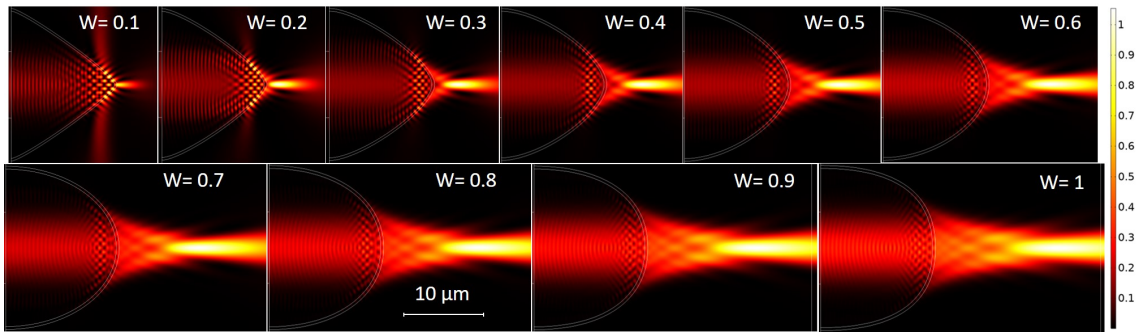

Figure A.1: Beam intensity distribution in space upon interacting with a AR coated PDMS micro-lens with a Bézier weight going from 0.1 to 1.

The AR coating reduces significantly the intensities of local maxima inside the micro-lens. By comparing figure 3.2 to A.1, we can see that at $\omega_0 = 0.5$ and above, the normalized intensity of the local maxima inside the micro-lens drop from around 80% (yellow color) to below 50% (red color). The drop is equally important for W ≤ 0.4, but it is less noticeable since there is no change of color.

Appendix B

Mid-IR diode laser in non-silica fluoride fiber coupling Zemax simulations

With spherical micro-lens

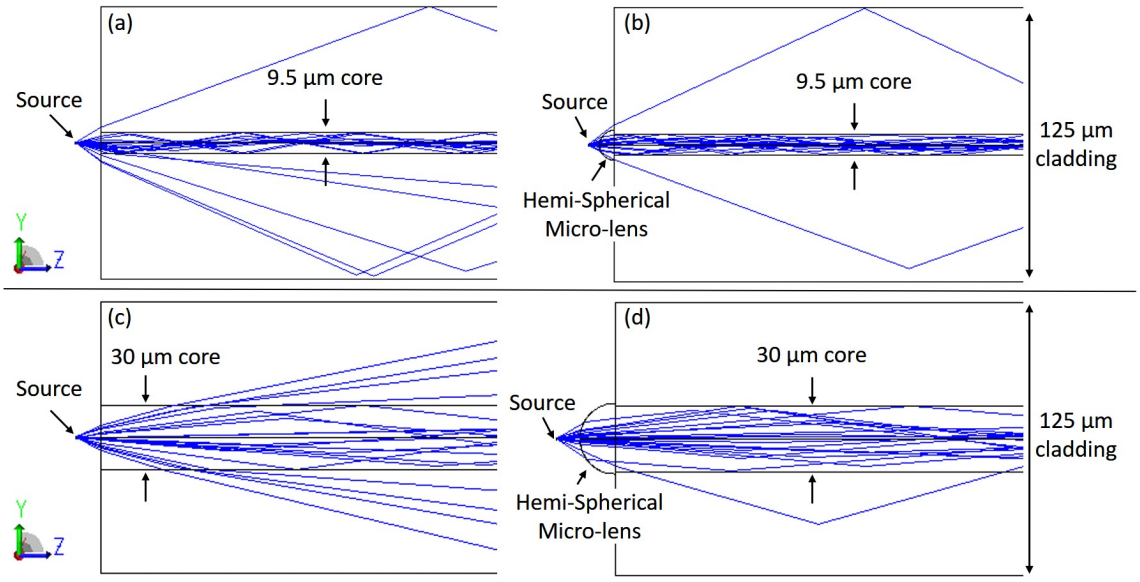

Figure B.1: Ray tracing of light generated by an ICL source, and its trajectory along: (a) plane, (b) lensed SM fiber and (c) plane, (d) lensed MM fiber. Both fibers' NA is 0.3 and the source's wavelength is 4.5 µm.

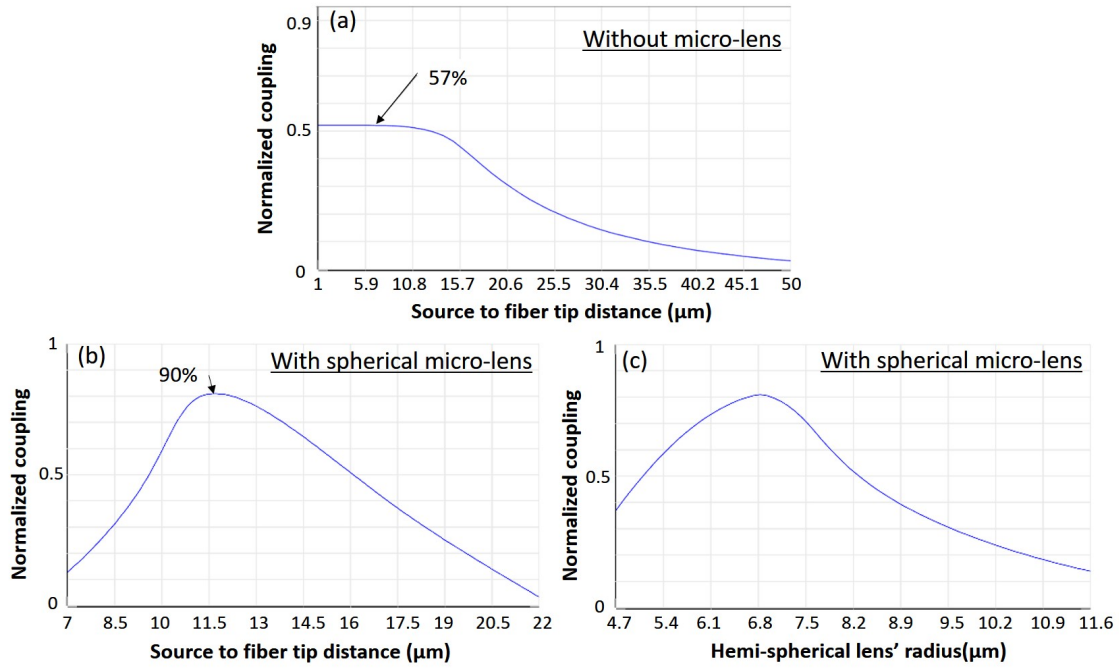

Figure B.2: Normalized coupling efficiency into SM fiber (9.5/125): (a) without lens as function of source to fiber distance, (b) with lens as function of source to fiber distance, (c) with lens as function of hemi-spherical lens' radius.

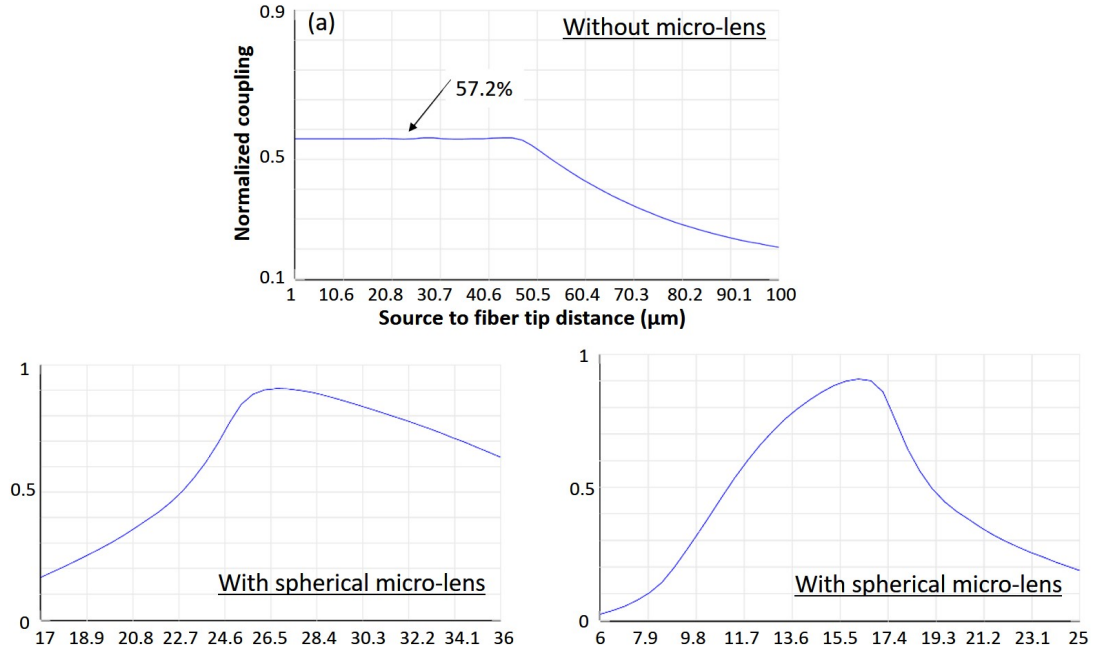

Figure B.3: Normalized coupling efficiency into MM fiber (30/125): (a) without lens as function of source to fiber distance, (b) with lens as function of source to fiber distance, (c) with lens as function of hemi-spherical lens' radius.

With Aspheric micro-lens

Table B.1: **coupling efficiency into SM fiber (9.5/125) equipped with an aspheric micro-lens.**

Base diameter	**Height**	**Curvature**	**Conic**	α_4	α_6	**Coupling (%)**
13.7	6.84	6.84	0	0	0	90.5
15.4	6.8	6.8	-0.3	3.25	73.26	89.9
19.2	6.8	6.8	-1	0.23	39.16	87.8
11.8	6.8	6.8	0.3	66.97	181.13	80.4

Table B.2: **coupling efficiency into MM fiber (30/125) equipped with an aspheric micro-lens.**

Base diameter	**Height**	**Curvature**	**Conic**	α_4	α_6	**Coupling (%)**
45.2	16	16	-1	0.07	3.82	96.7
36.4	16	16	-0.3	0.47	26.75	96
32.44	16.22	16.22	0	0	0	95.4
32	16	16	0	0	0	95.2

References

[1] Mário F S Ferreira and Mukul Chandra Paul, eds. *Optical Fiber Technology and Applications*. 2053-2563. IOP Publishing, 2021. ISBN: 978-0-7503-3243-9. DOI: 10.1088/978-0-7503-3243-9. URL: https://dx.doi.org/10.1088/978-0-7503-3243-9.

[2] Abraham Katzir. *Lasers and optical fibers in medicine*. Elsevier, 2012.

[3] LG Cohen. "Power coupling from GaAs injection lasers into optical fibers". In: *Bell System Technical Journal* 51.3 (1972), pp. 573–594.

[4] Hiroki Hamada. "Characterization of gallium indium phosphide and progress of aluminum gallium indium phosphide system quantum-well laser diode". In: *Materials* 10.8 (2017), p. 875.

[5] Gorgi Kostovski, Paul R Stoddart, and Arnan Mitchell. "The optical fiber tip: an inherently light-coupled microscopic platform for micro-and nanotechnologies". In: *Advanced Materials* 26.23 (2014), pp. 3798–3820.

[6] Mandeep Kaur, Geoffrey Hohert, Pierre M Lane, and Carlo Menon. "Fabrication of a stepped optical fiber tip for miniaturized scanners". In: *Optical Fiber Technology* 61 (2021), p. 102436.

[7] Mian Yao, Xia Ouyang, Jushuai Wu, A Ping Zhang, Hwa-Yaw Tam, and Ping-Kong Alex Wai. "Optical fiber-tip sensors based on in-situ μ-printed polymer suspended-microbeams". In: *Sensors* 18.6 (2018), p. 1825.

[8] Armando Ricciardi, Alessio Crescitelli, Patrizio Vaiano, Giuseppe Quero, Marco Consales, Marco Pisco, Emanuela Esposito, and Andrea Cusano. "Lab-on-fiber technology: a new vision for chemical and biological sensing". In: *Analyst* 140.24 (2015), pp. 8068–8079.

[9] JE Muñoz-Pérez, JL Cruz, Miguel V Andrés, and JG Ortega-Mendoza. "Conic optical fiber probe for generation and characterization of microbubbles in liquids". In: *Sensors and Actuators A: Physical* 317 (2021), p. 112441.

[10] Xiaogang Jiang and Daru Chen. "Low-cost fiber-tip Fabry-Perot interferometer and its application for transverse load sensing". In: *Progress In Electromagnetics Research Letters* 48 (2014), pp. 103–108.

[11] Robin Pierron, Grégoire Chabrol, Stéphane Roques, Pierre Pfeiffer, Jean-Paul Yehouessi, Géraud Bouwmans, and Sylvain Lecler. "Large-mode-area optical fiber for photonic nanojet generation". In: *Optics Letters* 44.10 (2019), pp. 2474–2477.

[12] Rita S Rodrigues Ribeiro, Olivier Soppera, Abel González Oliva, Ariel Guerreiro, and Pedro AS Jorge. "New trends on optical fiber tweezers". In: *Journal of Lightwave Technology* 33.16 (2015), pp. 3394–3405.

[13] Marco Pisco and Andrea Cusano. "Lab-on-fiber technology: a roadmap toward multifunctional plug and play platforms". In: *Sensors* 20.17 (2020), p. 4705.

[14] Jerome Schultz, Milan Mrksich, Sangeeta N Bhatia, David J Brady, Antonio J Ricco, David R Walt, Charles L Wilkins, and Charles L Wilkins. "Mass Spectrometry and Biosensing Research". In: *Biosensing* (2006), pp. 67–78.

[15] Hamed Abbasi, Raphael Guzman, Philippe C Cattin, and Azhar Zam. "All-fiber-optic LIBS system for tissue differentiation: A prospect for endoscopic smart laser osteotomy". In: *Optics and Lasers in Engineering* 148 (2022), p. 106765.

[16] Thierry Grosjean, Mathieu Mivelle, Geoffrey W Burr, and Fadi Issam Baida. "Optical horn antennas for efficiently transferring photons from a quantum emitter to a single-mode optical fiber". In: *Optics express* 21.2 (2013), pp. 1762–1772.

[17] Jaël Pauwels, Guy Van der Sande, and Guy Verschaffelt. "Space division multiplexing in standard multi-mode optical fibers based on speckle pattern classification". In: *Scientific reports* 9.1 (2019), p. 17597.

[18] Allan W Snyder and John D Love. *Optical waveguide theory*. Vol. 175. Chapman and hall London, 1983.

[19] Daisuke Kato. "Light coupling from a stripe-geometry GaAs diode laser into an optical fiber with spherical end". In: *Journal of Applied Physics* 44.6 (1973), pp. 2756–2758.

[20] Manfredo P Do Carmo. *Differential geometry of curves and surfaces: revised and updated second edition*. Courier Dover Publications, 2016.

[21] L Beijersbergen Allen and MW Spreeuw. "RJC and Woerdman, JP Phys". In: *Rev. A* 45 (1992), p. 8185.

[22] LA Wang and CD Su. "Tolerance analysis of aligning an astigmatic laser diode with a single-mode optical fiber". In: *Journal of lightwave technology* 14.12 (1996), pp. 2757–2762.

[23] Zaied Bouhafs, Assia Guessoum, Abdelhak Guermat, Djamila Bouaziz, Sylvain Lecler, and Nacer-Eddine Demagh. "Parabolic microlensed optical fiber for coupling efficiency improvement in single mode fiber". In: *Optics Continuum* 1.5 (2022), pp. 1218–1231.

[24] SN Vlasov, VA Petrishchev, and VI Talanov. "Averaged description of wave beams in linear and nonlinear media (the method of moments)". In: *Radiophysics and Quantum Electronics* 14.9 (1971), pp. 1062–1070.

[25] Zhigang Chen, Allen Taflove, and Vadim Backman. "Photonic nanojet enhancement of backscattering of light by nanoparticles: a potential novel visible-light ultramicroscopy technique". In: *Optics express* 12.7 (2004), pp. 1214–1220.

[26] Sylvain Lecler, Yoshitate Takakura, and Patrick Meyrueis. "Properties of a three-dimensional photonic jet". In: *Optics letters* 30.19 (2005), pp. 2641–2643.

[27] H-J Münzer, Mario Mosbacher, Micha Bertsch, Jörg Zimmermann, Paul Leiderer, and Johannes Boneberg. "Local field enhancement effects for nanostructuring of surfaces". In: *Journal of microscopy* 202.1 (2001), pp. 129–135.

[28] Naoaki Fukuda, Kazuyoshi Kunishio, and Shigeaki Nakayama. "'Dry-etching system'with Q-switched DPSS laser for flat panel displays". In: *J. Laser Micro Nanoeng.* 2 (2007), pp. 241–246.

[29] YF Lu, L Zhang, WD Song, YW Zheng, and BS Luk'Yanchuk. "Laser writing of a subwavelength structure on silicon (100) surfaces with particle-enhanced optical irradiation". In: *Journal of Experimental and Theoretical Physics Letters* 72 (2000), pp. 457–459.

[30] SM Huang, MH Hong, BS Luk'Yanchuk, YW Zheng, WD Song, YF Lu, and TC Chong. "Pulsed laser-assisted surface structuring with optical near-field enhanced effects". In: *Journal of Applied Physics* 92.5 (2002), pp. 2495–2500.

[31] Senthil Theppakuttai and Shaochen Chen. "Nanoscale surface modification of glass using a 1064 nm pulsed laser". In: *Applied physics letters* 83.4 (2003), pp. 758–760.

[32] Wei Wu, Alex Katsnelson, Omer G Memis, and Hooman Mohseni. "A deep sub-wavelength process for the formation of highly uniform arrays of nanoholes and nanopillars". In: *Nanotechnology* 18.48 (2007), p. 485302.

[33] Jianming Yang, Patrice Twardowski, Philippe Gérard, Yi Duo, Joël Fontaine, and Sylvain Lecler. "Ultra-narrow photonic nanojets through a glass cuboid embedded in a dielectric cylinder". In: *Optics Express* 26.4 (2018), pp. 3723–3731.

[34] Patrick Ferrand, Jérôme Wenger, Alexis Devilez, Martina Pianta, Brian Stout, Nicolas Bonod, Evgueni Popov, and Hervé Rigneault. "Direct imaging of photonic nanojets". In: *Optics express* 16.10 (2008), pp. 6930–6940.

[35] Myun-Sik Kim, Toralf Scharf, Stefan Mühlig, Carsten Rockstuhl, and Hans Peter Herzig. "Engineering photonic nanojets". In: *Optics express* 19.11 (2011), pp. 10206–10220.

[36] Guoqiang Gu, Rui Zhou, Zaichun Chen, Huiying Xu, Guoxiong Cai, Zhiping Cai, and Minghui Hong. "Super-long photonic nanojet generated from liquid-filled hollow microcylinder". In: *Optics Letters* 40.4 (2015), pp. 625–628.

[37] MX Wu, BJ Huang, R Chen, Y Yang, JF Wu, R Ji, XD Chen, and MH Hong. "Modulation of photonic nanojets generated by microspheres decorated with concentric rings". In: *Optics express* 23.15 (2015), pp. 20096–20103.

[38] Victor Pacheco-Peña, Igor V Minin, Oleg V Minin, and Miguel Beruete. "Comprehensive analysis of photonic nanojets in 3D dielectric cuboids excited by surface plasmons". In: *Annalen der Physik* 528.9-10 (2016), pp. 684–692.

[39] Arash Darafsheh. "Photonic nanojets and their applications". In: *Journal of Physics: Photonics* 3.2 (2021), p. 022001.

[40] Igor V Minin, Oleg V Minin, and Yuri E Geints. "Localized EM and photonic jets from non-spherical and non-symmetrical dielectric mesoscale objects: brief review". In: *Annalen der Physik* 527.7-8 (2015), pp. 491–497.

[41] Euan Mcleod and Craig B Arnold. “Subwavelength direct-write nanopatterning using optically trapped microspheres”. In: *Nature nanotechnology* 3.7 (2008), pp. 413–417.

[42] Yoshitate Takakura, Hanan Halaq, Sylvain Lecler, Stéphane Robert, and Bruno Sauviac. “Single and dual photonic jets with tipped waveguides: An integral approach”. In: *IEEE Photonics Technology Letters* 24.17 (2012), pp. 1516–1518.

[43] Petru Ghenuche, Hervé Rigneault, and Jérôme Wenger. “Photonic nanojet focusing for hollow-core photonic crystal fiber probes”. In: *Applied optics* 51.36 (2012), pp. 8637–8640.

[44] Julien Zelgowski, Andri Abdurrochman, Frederic Mermet, Pierre Pfeiffer, Joël Fontaine, and Sylvain Lecler. “Photonic jet subwavelength etching using a shaped optical fiber tip”. In: *Optics Letters* 41.9 (2016), pp. 2073–2076.

[45] Robin Pierron, Pierre Pfeiffer, Grégoire Chabrol, and Sylvain Lecler. “Photonic jet: Direct micro-peak machining”. In: *Applied Physics A* 123.11 (2017), p. 686.

[46] Djamila Bouaziz, Stephane Perrin, Tony Hajj, Grégoire Chabrol, Assia Guessoum, Nacer-Eddine Demagh, and Sylvain Lecler. “Direct imaging of a photonic jet at shaped fiber tips”. In: *Optics Letters* 46.20 (2021), pp. 5125–5128.

[47] Svetlana Nikolaevna Khonina, Nikolay Lvovich Kazanskiy, Sergey Vladimirovich Karpeev, and Muhammad Ali Butt. “Bessel beam: Significance and applications—A progressive review”. In: *Micromachines* 11.11 (2020), p. 997.

[48] Thierry Grosjean, Said Sadat Saleh, Miguel Angel Suarez, Idriss Abdoulkader Ibrahim, Vincent Piquerey, Daniel Charraut, and Patrick Sandoz. “Fiber microaxicons fabricated by a polishing technique for the generation of Bessel-like beams”. In: *Applied optics* 46.33 (2007), pp. 8061–8067.

[49] Zhenwei Xie, Shecheng Gao, Ting Lei, Shengfei Feng, Yan Zhang, Fan Li, Jianbo Zhang, Zhaohui Li, and Xiaocong Yuan. “Integrated (de) multiplexer for orbital angular momentum fiber communication”. In: *Photonics Research* 6.7 (2018), pp. 743–749.

[50] Gustav Mie. “Beiträge zur Optik trüber Medien, speziell kolloidaler Metallösungen”. In: *Annalen der physik* 330.3 (1908), pp. 377–445.

[51] Yu-lin Xu and Bo ÅS Gustafson. “A generalized multiparticle Mie-solution: further experimental verification”. In: *Journal of Quantitative Spectroscopy and Radiative Transfer* 70.4-6 (2001), pp. 395–419.

[52] K_ Knop. “Rigorous diffraction theory for transmission phase gratings with deep rectangular grooves”. In: *JOSA* 68.9 (1978), pp. 1206–1210.

[53] Lifeng Li. *Fourier modal method*. 2014.

[54] Kofi Sényo Edee. “Méthodes modales pour la modélisation de nanostructures photoniques périodiques et non périodiques”. PhD thesis. Université BLAISE PASCAL, 2012.

[55] Kane Yee. “Numerical solution of initial boundary value problems involving Maxwell’s equations in isotropic media”. In: *IEEE Transactions on antennas and propagation* 14.3 (1966), pp. 302–307.

[56] Karl S Kunz and Raymond J Luebbers. *The finite difference time domain method for electromagnetics*. CRC press, 1993.

[57] John L Volakis and Leo C Kempel. “Electromagnetics: computational methods and considerations”. In: *IEEE computational science and engineering* 2.1 (1995), pp. 42–57.

[58] Badreddine Ounnas. “Étude et optimisations de jets photoniques pour des applications non conventionnelles dans les domaines optique et hyperfréquences”. PhD thesis. Université Jean Monnet-Saint-Etienne, 2015.

[59] LG Cohen and MV Schneider. “Microlenses for coupling junction lasers to optical fibers”. In: *Applied Optics* 13.1 (1974), pp. 89–94.

[60] Jingyi Yang, Indra Ghimire, Pin Chieh Wu, Sudip Gurung, Catherine Arndt, Din Ping Tsai, and Ho Wai Howard Lee. “Photonic crystal fiber metalens”. In: *Nanophotonics* 8.3 (2019), pp. 443–449.

[61] Rita S Rodrigues Ribeiro, Pabitra Dahal, Ariel Guerreiro, Pedro AS Jorge, and Jaime Viegas. “Fabrication of Fresnel plates on optical fibres by FIB milling for optical trapping, manipulation and detection of single cells”. In: *Scientific reports* 7.1 (2017), pp. 1–14.

[62] Jean-Baptiste Decombe, Serge Huant, and Jochen Fick. “Single and dual fiber nano-tip optical tweezers: trapping and analysis”. In: *Optics express* 21.25 (2013), pp. 30521–30531.

[63] Jean-Baptiste Decombe, Francisco J Valdivia-Valero, Gérard Colas Des Francs, and Jochen Fick. “Plasmonic coupling between metallized fiber tips with subwavelength open apertures”. In: *Nanophotonics VI*. Vol. 9884. SPIE. 2016, pp. 428–433.

[64] RA Minz, U Tiwari, A Kumar, S Nic Chormaic, K Lahlil, T Gacoin, SK Mondal, and J Fick. “Trapping of rare earth-doped nanorods using quasi Bessel beam optical fiber tweezers”. In: *OSA Continuum* 4.2 (2021), pp. 364–373.

[65] Federica Piccirillo, Martino Giaquinto, Armando Ricciardi, and Andrea Cusano. “Miniaturized lenses integrated on optical fibers: Towards a new milestone along the lab-on-fiber technology roadmap”. In: *Results in Optics* 6 (2022), p. 100203.

[66] RS Evenblij and JAP Leijtens. “Space Gator: a giant leap for fiber optic sensing”. In: *International Conference on Space Optics—ICSO 2014*. Vol. 10563. SPIE. 2017, pp. 373–380.

[67] Renaud Bachelot, Carole Ecoffet, Denis Deloeil, Pascal Royer, and Daniel-Joseph Lougnot. “Integration of micrometer-sized polymer elements at the end of optical fibers by free-radical photopolymerization”. In: *Applied optics* 40.32 (2001), pp. 5860–5871.

[68] Atsushi Okamoto, Kohei Aoki, Yuta Wakayama, Daiki Soma, and Takuya Oda. "Multi-excitation of spatial modes using single spatial light modulator for mode division multiplexing". In: *Optical Fiber Communication Conference*. Optica Publishing Group. 2012, JW2A–38.

[69] Rita S Rodrigues Ribeiro, Raquel Queirós, Olivier Soppera, Ariel Guerreiro, and Pedro AS Jorge. "Optical fiber tweezers fabricated by guided wave photopolymerization". In: *Photonics*. Vol. 2. MDPI. 2015, pp. 634–645.

[70] Cong Xiong, Changrui Liao, Zhengyong Li, Kaiming Yang, Meng Zhu, Yuanyuan Zhao, and Yiping Wang. "Optical Fiber Integrated Functional Micro-/Nanostructure Induced by Two-Photon Polymerization". In: *Frontiers in Materials* 7 (2020), p. 586496.

[71] Hongmei Zou, He Huang, Shijie Chen, Qing Li, Jian Fu, Feng Lin, and X Wu. "Laser printed fiber microlens for fiber-diode coupling by direct laser writing". In: *Applied Optics* 53.36 (2014), pp. 8444–8448.

[72] A Kuchmizhak, S Gurbatov, A Nepomniaschii, O Vitrik, and Yu Kulchin. "High-quality fiber microaxicons fabricated by a modified chemical etching method for laser focusing and generation of Bessel-like beams". In: *Applied optics* 53.5 (2014), pp. 937–943.

[73] P-I Dietrich, M Blaicher, I Reuter, M Billah, T Hoose, A Hofmann, C Caer, Roger Dangel, B Offrein, U Troppenz, M. Moehrle, W. Freude, and C. Koos. "In situ 3D nanoprinting of free-form coupling elements for hybrid photonic integration". In: *Nature Photonics* 12.4 (2018), pp. 241–247.

[74] Henry E Williams, Daniel J Freppon, Stephen M Kuebler, Raymond C Rumpf, and Marco A Melino. "Fabrication of three-dimensional micro-photonic structures on the tip of optical fibers using SU-8". In: *Optics express* 19.23 (2011), pp. 22910–22922.

[75] N Anscombe. "Direct laser writing Nat". In: Photon. 2010.

[76] V Harinarayana and YC Shin. "Two-photon lithography for three-dimensional fabrication in micro/nanoscale regime: A comprehensive review". In: *Optics & Laser Technology* 142 (2021), p. 107180.

[77] Israel Weiss and Dan M Marom. "Direct 3D nano-printing on optical fiber tip". In: *2015 International Conference on Optical MEMS and Nanophotonics (OMN)*. IEEE. 2015, pp. 1–2.

[78] Christopher A Edwards, Herman M Presby, and Corrado Dragone. "Ideal microlenses for laser to fiber coupling". In: *Journal of Lightwave Technology* 11.2 (1993), pp. 252–257.

[79] NM Presby and CR Giles. "Asymmetric fiber microlenses for efficient coupling to elliptical laser beams". In: *IEEE Photonics Technology Letters* 5.2 (1993), pp. 184–186.

[80] Monique Thual, Gautier Moreau, Julien Ribette, Philippe Rochard, Michel Gadonna, and Jean-Claude Simon. "Micro-lens on polarization maintaining fibre for coupling with 1.55 μm quantum dot devices". In: *Optics communications* 255.4-6 (2005), pp. 278–285.

[81] Chung-Hao Tien, Yin-Chieh Lai, Tom D Milster, and Han-Ping D Shieh. "Design and fabrication of fiberlenses for optical recording applications". In: *Japanese journal of applied physics* 41.3S (2002), p. 1834.

[82] M Thual, J Lostec, P Auvray, and B Clavel. *Procédé de fabrication d'un dispositif de couplage optique collectif*.

[83] Philippe Chanclou, Monique Thual, Jean Lostec, Patrick Auvray, J Caulet, G Joulie, A Poudoulec, and Benedicte Clavel. "Highly efficient collective coupling between laser diode array and lensed fibre ribbon". In: *Electronics Letters* 34.3 (1998), p. 273.

[84] Rafal Kasztelanic, Adam Filipkowski, Alicja Anuszkiewicz, Paulina Stafiej, Grzegorz Stepniewski, Dariusz Pysz, Konrad Krzyzak, Ryszard Stepien, Mariusz Klimczak, and Ryszard Buczynski. "Integrating free-form nanostructured GRIN microlenses with single-mode fibers for optofluidic systems". In: *Scientific Reports* 8.1 (2018), pp. 1–12.

[85] Herman M Presby, AF Benner, and CA Edwards. "Laser micromachining of efficient fiber microlenses". In: *Applied optics* 29.18 (1990), pp. 2692–2695.

[86] C Buerhop, B Blumenthal, R_ Weissmann, N Lutz, and S Biermann. "Glass surface treatment with excimer and CO2 lasers". In: *Applied surface science* 46.1-4 (1990), pp. 430–434.

[87] G Eisenstein and D Vitello. "Chemically etched conical microlenses for coupling single-mode lasers into single-mode fibers". In: *Applied Optics* 21.19 (1982), pp. 3470–3474.

[88] Assia Guessoum. "Optimisation du couplage optique par modification des bouts des fibres optiques". PhD thesis. Setif University, 2018.

[89] Stephen T Tso and JOSEPH A PASK. "Reaction of glasses with hydrofluoric acid solution". In: *Journal of the American Ceramic Society* 65.7 (1982), pp. 360–362.

[90] Kurt R Mikeska, Stephen J Bennison, and Steven L Grise. "Corrosion of ceramics in aqueous hydrofluoric acid". In: *Journal of the American Ceramic Society* 83.5 (2000), pp. 1160–1164.

[91] Huei-Min Yang, Sun-Yuan Huang, Chao-Wei Lee, Tsong-Sheng Lay, and Wood-Hi Cheng. "High-coupling tapered hyperbolic fiber microlens and taper asymmetry effect". In: *Journal of lightwave technology* 22.5 (2004), pp. 1395–1401.

[92] Xin Huo, Shi Pan, and Shifa Wu. "Fabrication of optical fiber probe nano-tips by heated micro-pulling combined with static chemical etching". In: *2006 1st IEEE International Conference on Nano/Micro Engineered and Molecular Systems*. IEEE. 2006, pp. 254–257.

[93] Yu-Kuan Lu, Ying-Chien Tsai, Yu-Da Liu, Szu-Ming Yeh, Chi-Chung Lin, and Wood-Hi Cheng. "Asymmetric elliptic-cone-shaped microlens for efficient coupling to high-power laser diodes". In: *Optics express* 15.4 (2007), pp. 1434–1442.

[94] Nadjiba Boulaiche, Philippe Rochard, Assia Guessoum, Nacer-Eddine Demagh, and Monique Thual. "Hemi-ellipsoidal microlensed fiber based on polishing and polymer technology". In: *Engineering Research Express* 3.4 (2021), p. 045051.

[95] Chun-Ching Wu, Yi-Dun Tseng, Su-Ming Kuo, and Che-Hsin Lin. "Fabrication of asperical lensed optical fibers with an electro-static pulling of SU-8 photoresist". In: *Optics express* 19.23 (2011), pp. 22993–22998.

[96] Nacer-Eddine Demagh, Assia Guessoum, Rabah Zegari, and Tijani Gharbi. "Self-centring technique for fibre optic microlens mounting using a concave cone-etched fibre". In: *Measurement Science and Technology* 22.11 (2011), p. 115302.

[97] Chutian Wen, Jinyuan Hu, Wenshuai Xu, Jinhui Shi, Shenglai Zhen, Zhigang Cao, Benli Yu, and Feng Xu. "A simple and low-cost fabrication method of microlens on optical fiber end facet". In: *Optik* 214 (2020), p. 164829.

[98] Ricardo Janeiro, Raquel Flores, Pabitra Dahal, and Jaime Viegas. "Fabrication of a phase photon sieve on an optical fiber tip by focused ion beam nanomachining for improved fiber to silicon photonics waveguide light coupling". In: *Optics Express* 24.11 (2016), pp. 11611–11625.

[99] Alexander Koshelev, Giuseppe Calafiore, Carlos Piña-Hernandez, Frances I Allen, Scott Dhuey, Simone Sassolini, Edward Wong, Paul Lum, Keiko Munechika, and Stefano Cabrini. "High refractive index Fresnel lens on a fiber fabricated by nanoimprint lithography for immersion applications". In: *Optics Letters* 41.15 (2016), pp. 3423–3426.

[100] Oleh Yermakov, Henrik Schneidewind, Uwe Hübner, Torsten Wieduwilt, Matthias Zeisberger, Andrey Bogdanov, Yuri Kivshar, and Markus A Schmidt. "Nanostructure-empowered efficient coupling of light into optical fibers at extraordinarily large angles". In: *Acs Photonics* 7.10 (2020), pp. 2834–2841.

[101] Timo Gissibl, Michael Schmid, and Harald Giessen. "Spatial beam intensity shaping using phase masks on single-mode optical fibers fabricated by femtosecond direct laser writing". In: *Optica* 3.4 (2016), pp. 448–451.

[102] Asa Asadollahbaik, Simon Thiele, Ksenia Weber, Aashutosh Kumar, Johannes Drozella, Florian Sterl, Alois M Herkommer, Harald Giessen, and Jochen Fick. "Highly efficient dual-fiber optical trapping with 3D printed diffractive fresnel lenses". In: *ACS photonics* 7.1 (2019), pp. 88–97.

[103] Hyuntai Kim, Jinseob Kim, Haechan An, Yohan Lee, Gun-yeal Lee, Jeongkyun Na, Kyoungyoon Park, Seungjong Lee, Seung-Yeol Lee, Byoungho Lee, and Yoonchan Jeong. "Metallic Fresnel zone plate implemented on an optical fiber facet for super-variable focusing of light". In: *Optics express* 25.24 (2017), pp. 30290–30303.

[104] Vitor R Manfrinato, Lihua Zhang, Dong Su, Huigao Duan, Richard G Hobbs, Eric A Stach, and Karl K Berggren. "Resolution limits of electron-beam lithography toward the atomic scale". In: *Nano letters* 13.4 (2013), pp. 1555–1558.

[105] C Vieu, F Carcenac, A Pepin, Y Chen, M Mejias, and A Lebib. "L. Manin-Ferlazzo, Couraud L. & H. Launois". In: *Appl Surf Sci* 164 (2000), pp. 111–117.

[106] Stephen Y Chou, Peter R Krauss, and Preston J Renstrom. "Imprint of sub-25 nm vias and trenches in polymers". In: *Applied physics letters* 67.21 (1995), pp. 3114–3116.

[107] Jiho Han, Martin Sparkes, and William O'Neill. "Controlling the optical fiber output beam profile by focused ion beam machining of a phase hologram on fiber tip". In: *Applied Optics* 54.4 (2015), pp. 890–894.

[108] Changyi Zhou, Woo-Bin Lee, Song Gao, Hongliang Li, Chul-Soon Park, Duk-Yong Choi, and Sang-Shin Lee. "All-Dielectric Fiber Meta-Tip Enabling Vortex Generation and Beam Collimation for Optical Interconnect". In: *Laser & Photonics Reviews* 15.5 (2021), p. 2000581.

[109] Ning Wang, Matthias Zeisberger, Uwe Hübner, and Markus A Schmidt. "Boosting light collection efficiency of optical fibers using metallic nanostructures". In: *Acs Photonics* 6.3 (2019), pp. 691–698.

[110] Haoran Ren, Jaehyuck Jang, Chenhao Li, Andreas Aigner, Malte Plidschun, Jisoo Kim, Junsuk Rho, Markus A Schmidt, and Stefan A Maier. "An achromatic metafiber for focusing and imaging across the entire telecommunication range". In: *nature communications* 13.1 (2022), p. 4183.

[111] Maria Principe, M Consales, A Micco, A Crescitelli, G Castaldi, Emanuela Esposito, Vera La Ferrara, A Cutolo, V Galdi, and A Cusano. "Optical fiber meta-tips". In: *Asia-Pacific Optical Sensors Conference*. Optica Publishing Group. 2016, F1A–3.

[112] Alan She, Shuyan Zhang, Samuel Shian, David R Clarke, and Federico Capasso. "Large area metalenses: design, characterization, and mass manufacturing". In: *Optics express* 26.2 (2018), pp. 1573–1585.

[113] Joon-Suh Park, Shuyan Zhang, Alan She, Wei Ting Chen, Peng Lin, Kerolos MA Yousef, Ji-Xin Cheng, and Federico Capasso. "All-glass, large metalens at visible wavelength using deep-ultraviolet projection lithography". In: *Nano letters* 19.12 (2019), pp. 8673–8682.

[114] Alberto Lombardini, Vasyl Mytskaniuk, Siddharth Sivankutty, Esben Ravn Andresen, Xueqin Chen, Jérôme Wenger, Marc Fabert, Nicolas Joly, Frédéric Louradour, Alexandre Kudlinski, and Hervé Rigneault. "High-resolution multimodal flexible coherent Raman endoscope". In: *Light: Science & Applications* 7.1 (2018), p. 10.

[115] Karolina Milenko, Stephanos Yerolatsitis, Astrid Aksnes, Dag Roar Hjelme, and James M Stone. "Micro-lensed negative-curvature fibre probe for raman spectroscopy". In: *Sensors* 21.24 (2021), p. 8434.

[116] RF Cregan, BJ Mangan, JC Knight, TA Birks, P St J Russell, PJ Roberts, and DC Allan. "Single-mode photonic band gap guidance of light in air". In: *science* 285.5433 (1999), pp. 1537–1539.

[117] F Benabid and PJ Roberts. "Linear and nonlinear optical properties of hollow core photonic crystal fiber". In: *Journal of Modern Optics* 58.2 (2011), pp. 87–124.

[118] Ivan P Christov. "Enhanced generation of attosecond pulses in dispersion-controlled hollow-core fiber". In: *Physical Review A* 60.4 (1999), p. 3244.

[119] Wei Ding, Ying-Ying Wang, Shou-Fei Gao, Meng-Ling Wang, and Pu Wang. "Recent progress in low-loss hollow-core anti-resonant fibers and their applications". In: *IEEE Journal of Selected Topics in Quantum Electronics* 26.4 (2019), pp. 1–12.

[120] YY Wang, Francois Couny, PJ Roberts, and F Benabid. "Low loss broadband transmission in optimized core-shape Kagome hollow-core PCF". In: *Conference on Lasers and Electro-Optics*. Optica Publishing Group. 2010, CPDB4.

[121] SO Konorov, AM Zheltikov, Ping Zhou, AP Tarasevitch, and D von der Linde. "Self-channeling of subgigawatt femtosecond laser pulses in a ground-state waveguide induced in the hollow core of a photonic crystal fiber". In: *Optics letters* 29.13 (2004), pp. 1521–1523.

[122] Anne Sieburg, Sebastian Schneider, Di Yan, Jürgen Popp, and Torsten Frosch. "Monitoring of gas composition in a laboratory biogas plant using cavity enhanced Raman spectroscopy". In: *Analyst* 143.6 (2018), pp. 1358–1366.

[123] Andreas Knebl, Di Yan, Jürgen Popp, and Torsten Frosch. "Fiber enhanced Raman gas spectroscopy". In: *TrAC Trends in Analytical Chemistry* 103 (2018), pp. 230–238.

[124] Md Selim Habib, Christos Markos, Ole Bang, and Morten Bache. "Soliton-plasma nonlinear dynamics in mid-IR gas-filled hollow-core fibers". In: *Optics letters* 42.11 (2017), pp. 2232–2235.

[125] Yazhou Wang, Yuyang Feng, Abubakar I Adamu, Manoj K Dasa, JE Antonio-Lopez, Rodrigo Amezcua-Correa, and Christos Markos. "Mid-infrared photoacoustic gas monitoring driven by a gas-filled hollow-core fiber laser". In: *Scientific reports* 11.1 (2021), p. 3512.

[126] Huaping Gong, Chi Chiu Chan, Yi Fan Zhang, Wei Chang Wong, and Xinyong Dong. "Miniature refractometer based on modal interference in a hollow-core photonic crystal fiber with collapsed splicing". In: *Journal of Biomedical Optics* 16.1 (2011), pp. 017004–017004.

[127] Dora Juan Juan Hu, Yixin Wang, Jun Long Lim, Taishi Zhang, Karolina Barbara Milenko, Zhihao Chen, Meng Jiang, Guanghui Wang, Feng Luan, Ping P Shum, Qizhen Sun, Huifeng Wei, Weijun Tong, and Tomasz R. Wolunski. "Novel miniaturized Fabry–Perot refractometer based on a simplified hollow-core fiber with a hollow silica sphere tip". In: *IEEE Sensors Journal* 12.5 (2011), pp. 1239–1245.

[128] Hanna Izabela Stawska, Maciej Andrzej Popenda, and Elżbieta Bereś-Pawlik. "Combining hollow core photonic crystal fibers with multimode, solid core fiber couplers through arc fusion splicing for the miniaturization of nonlinear spectroscopy sensing devices". In: *Fibers* 6.4 (2018), p. 77.

[129] R Thapa, K Knabe, KL Corwin, and BR Washburn. "Arc fusion splicing of hollow-core photonic bandgap fibers for gas-filled fiber cells". In: *Optics Express* 14.21 (2006), pp. 9576–9583.

[130] Alexandre Kudlinski, A Cassez, O Vanvincq, D Septier, A Pastre, R Habert, K Baudelle, M Douay, V Mytskaniuk, V Tsvirkun, H Rigneault, and G Bouwmans. "Double clad tubular anti-resonant hollow core fiber for nonlinear microendoscopy". In: *Optics Express* 28.10 (2020), pp. 15062–15070.

[131] Ashleigh Louise Barron. "Integrated Multicore Fibre Devices for Optical Trapping". PhD thesis. Heriot-Watt University, 2014.

[132] Georgia Anastasiadi, Mark Leonard, Lynn Paterson, and William N Macpherson. "Fabrication and characterization of machined multi-core fiber tweezers for single cell manipulation". In: *Optics Express* 26.3 (2018), pp. 3557–3567.

[133] Carlo Liberale, G Cojoc, F Bragheri, P Minzioni, G Perozziello, R La Rocca, L Ferrara, V Rajamanickam, E Di Fabrizio, and I Cristiani. "Integrated microfluidic device for single-cell trapping and spectroscopy". In: *Scientific reports* 3.1 (2013), pp. 1–7.

[134] AL Barron, AK Kar, G Brown, TJ Aspray, AJ Waddie, MR Taghizadeh, and HT Bookey. "Optical Trapping using a Lensed Multicore Fiber". In: *Workshop on Specialty Optical Fibers and their Applications*. Optica Publishing Group. 2013, T1–3.

[135] Xiaoting Zhao, Nan Zhao, Yang Shi, Hongbao Xin, and Baojun Li. "Optical fiber tweezers: a versatile tool for optical trapping and manipulation". In: *Micromachines* 11.2 (2020), p. 114.

[136] Siddharth Sivankutty, Andrea Bertoncini, Victor Tsvirkun, Naveen Gajendra Kumar, Gaelle Brévalle, Géraud Bouwmans, Esben Ravn Andresen, Carlo Liberale, and Hervé Rigneault. "Miniature 120-beam coherent combiner with 3D-printed optics for multicore fiber-based endoscopy". In: *Optics Letters* 46.19 (2021), pp. 4968–4971.

[137] Yoshiki Kamiura, Taiga Kurisawa, Chiemi Fujikawa, and Osamu Mikami. "High optical coupling efficiency of polymer microlens and pillar on single mode fiber for silicon photonics". In: *Japanese Journal of Applied Physics* 61.SK (2022), SK1009.

[138] Philipp-Immanuel Dietrich, Robert J Harris, Matthias Blaicher, Mark K Corrigan, Tim J Morris, Wolfgang Freude, Andreas Quirrenbach, and Christian Koos. "Printed freeform lens arrays on multi-core fibers for highly efficient coupling in astrophotonic systems". In: *Optics express* 25.15 (2017), pp. 18288–18295.

[139] Nicolino Stasio, Donald B Conkey, Christophe Moser, and Demetri Psaltis. "Light control in a multicore fiber using the memory effect". In: *Optics express* 23.23 (2015), pp. 30532–30544.

[140] Solenn Cozic, Simon Boivinet, Christophe Pierre, Johan Boulet, Samuel Poulain, and Marcel Poulain. "Splicing fluoride glass and silica optical fibers". In: *EPJ Web of Conferences*. Vol. 215. EDP Sciences. 2019, p. 04003.

[141] Assia Guessoum, Tony Hajj, Djamila Bouaziz, Gregoire Chabrol, Pierre Pfeiffer, Nacer-E Demagh, and Sylvain Lecler. "Molded high curvature core-aligned micro-lenses for single-mode fibers". In: *Applied Optics* 61.26 (2022), pp. 7741–7747.

[142] AS Tenney and M Ghezzo. "Etch rates of doped oxides in solutions of buffered HF". In: *Journal of the Electrochemical Society* 120.8 (1973), p. 1091.

[143] Paula AR Tafulo, PAS Jorge, JL Santos, and O Frazão. "Fabry–Pérot cavities based on chemical etching for high temperature and strain measurement". In: *Optics Communications* 285.6 (2012), pp. 1159–1162.

[144] S Neffe and M Szustakowski. "Characterization of the microstructure of optical fibres". In: *Optical Fibres and Their Applications IV*. Vol. 670. SPIE. 1986, pp. 100–103.

[145] Brian G Risch. "Specialty fiber optic applications for harsh and high radiation environments". In: *Fiber Optic Sensors and Applications XII*. Vol. 9480. SPIE. 2015, pp. 95–108.

[146] Kanglin Li, Jiangbing Du, Weihong Shen, Jiacheng Liu, and Zuyuan He. "Improved optical coupling based on a concave cavity lens fabricated by optical fiber facet etching". In: *Chinese Optics Letters* 19.5 (2021), p. 050602.

[147] P Pace, Shane T Huntington, K Lyytikäinen, Ann Roberts, and JD Love. "Refractive index profiles of Ge-doped optical fibers with nanometer spatial resolution using atomic force microscopy". In: *Optics Express* 12.7 (2004), pp. 1452–1457.

[148] Geo M Philip and Nirmal K Viswanathan. "Fabrication of negative micro axicons in optical fibers via chemical etching". In: *Oral presentation in ICOP* (2009).

[149] Monsef Zaboub, Assia Guessoum, Nacer-Eddine Demagh, and Abdelhak Guermat. "Fabrication of polymer microlenses on single mode optical fibers for light coupling". In: *Optics Communications* 366 (2016), pp. 122–126.

[150] Mona Mayeh and Faramarz Farahi. "Laser beam shaping and mode conversion in optical fibers". In: *Photonic Sensors* 1.2 (2011), pp. 187–198.

[151] *Vytran Optical Fiber Glass Processors*. `https://www.thorlabs.com/images/Brochures/Vytran_GPX_Glass_Processors_Brochure.pdf`.

[152] Wilfried Blanc, M Vermillac, F Peters, C Kucera, M Tuggle, T Hawkins, and J Ballato. "Drawing optical fibers: elongating bubbles, breaking nanoparticles". In: *OPAL*. 2018.

[153] *Sylgardtm 184 silicone elastomer features benefits, 2017. www.consumer.dow.com.*

[154] *Norland Optical Adhesive 61. https://www.norlandprod.com/adhesives/NOA%2061.html.*

[155] Ali K Kamrani and Emad Abouel Nasr. *Rapid prototyping: theory and practice*. Vol. 6. Springer Science & Business Media, 2006.

[156] Zakaria Razak, Abu Bakar Sulong, Norhamidi Muhamad, Che Hassan Che Haron, Mohd Khairul Fadzly Md Radzi, Nur Farhani Ismail, Dulina Tholibon, and Izdihar Tharazi. "Effects of thermal cycling on physical and tensile properties of injection moulded kenaf/carbon nanotubes/polypropylene hybrid composites". In: *Composites Part B: Engineering* 168 (2019), pp. 159–165.

[157] Hao-Bing Liu, Hai-Qing Gong, Naveen Ramalingam, Yu Jiang, Chang-Chun Dai, and Kam M Hui. "Micro air bubble formation and its control during polymerase chain reaction (PCR) in polydimethylsiloxane (PDMS) microreactors". In: *Journal of Micromechanics and Microengineering* 17.10 (2007), p. 2055.

[158] TC Merkel, VI Bondar, K Nagai, BD Freeman, and I Pinnau. "Gas sorption, diffusion, and permeation in poly (dimethylsiloxane)". In: *Journal of Polymer Science Part B: Polymer Physics* 38.3 (2000), pp. 415–434.

[159] Karol Zalewski, Zbigniew Chyłek, and Waldemar A Trzciński. "A review of polysiloxanes in terms of their application in explosives". In: *Polymers* 13.7 (2021), p. 1080.

[160] Michael Johnson, Greg Liddiard, Mark Eddings, and Bruce Gale. "Bubble inclusion and removal using PDMS membrane-based gas permeation for applications in pumping, valving and mixing in microfluidic devices". In: *Journal of micromechanics and microengineering* 19.9 (2009), p. 095011.

[161] *Vitran Fiber Preparation and Splicing: SM, MM, and PM*. https://www.thorlabs.com/newgrouppage9.cfm?objectgroup_id=9512.

[162] *S22 Multi-Core Fiber Fusion Splicer*. https://shinhoamerica.com/product/s22-multi-core-fiber-fusion-splicer/.

[163] Feifan Lv, Yinqiang Zheng, Bohan Zhang, and Feng Lu. "Turn a silicon camera into an ingaas camera". In: *Proceedings of the IEEE/CVF Conference on Computer Vision and Pattern Recognition*. 2019, pp. 5987–5995.

[164] Gerald Farin. *Curves and surfaces for CAGD: a practical guide*. Morgan Kaufmann, 2002.

[165] Max Born and Emil Wolf. *Principles of optics: electromagnetic theory of propagation, interference and diffraction of light*. Elsevier, 2013, pp. 61–64.

[166] Xiaoning Zhang, Jun Qiu, Junming Zhao, Xingcan Li, and Linhua Liu. "Complex refractive indices measurements of polymers in infrared bands". In: *Journal of Quantitative Spectroscopy and Radiative Transfer* 252 (2020), p. 107063.

[167] Martin H. Weik. "Fresnel reflection loss". In: *Computer Science and Communications Dictionary*. Boston, MA: Springer US, 2001, pp. 657–657. ISBN: 978-1-4020-0613-5. DOI: 10.1007/1-4020-0613-6_7725. URL: https://doi.org/10.1007/1-4020-0613-6_7725.

[168] Wang-Yuhl Oh, BE Bouma, N Iftimia, SH Yun, R Yelin, and GJ Tearney. "Ultrahigh-resolution full-field optical coherence microscopy using InGaAs camera". In: *Optics express* 14.2 (2006), pp. 726–735.

[169] Di Lin, Joel Carpenter, Yutong Feng, Saurabh Jain, Yongmin Jung, Yujun Feng, Michalis N Zervas, and David J Richardson. "Reconfigurable structured light generation in a multicore fibre amplifier". In: *Nature communications* 11.1 (2020), p. 3986.

[170] F Prevost, L Lombard, J Primot, LP Ramirez, Laurent Bigot, G Bouwmans, and Marc Hanna. "Coherent beam combining of a narrow-linewidth long-pulse Er 3+-doped multicore fiber amplifier". In: *Optics Express* 25.9 (2017), pp. 9528–9534.

[171] John A Neff, Ravinda A Athale, and Sing H Lee. "Two-dimensional spatial light modulators: a tutorial". In: *Proceedings of the IEEE* 78.5 (1990), pp. 826–855.

[172] Long Zhu and Jian Wang. "Arbitrary manipulation of spatial amplitude and phase using phase-only spatial light modulators". In: *Scientific reports* 4.1 (2014), p. 7441.

[173] Ralph W Gerchberg. "A practical algorithm for the determination of plane from image and diffraction pictures". In: *Optik* 35.2 (1972), pp. 237–246.

[174] Lourdes Patricia Ramirez, Marc Hanna, Géraud Bouwmans, Hicham El Hamzaoui, Mohamed Bouazaoui, Damien Labat, Karen Delplace, Julien Pouysegur, Florent Guichard, Philippe Rigaud, Vincent Kermène, Agnès Desfarges-Berthelemot, Alain Barthélémy, Florian Prévost, Laurent Lombard, Yoann Zaouter, Frédéric Druon, and Patrick Georges. "Coherent beam combining with an ultrafast multicore Yb-doped fiber amplifier". In: *Optics Express* 23.5 (2015), pp. 5406–5416.

[175] Małgorzata Kujawińska, Rosario Porras-Aguilar, and Weronika Zaperty. "LCoS spatial light modulators as active phase elements of full-field measurement systems and sensors". In: *Metrology and Measurement Systems* (2012), pp. 445–458.

[176] Benjamin S Williams, Sushil Kumar, Qing Hu, and John L Reno. "High-power terahertz quantum cascade lasers". In: *2006 Conference on Lasers and Electro-Optics and 2006 Quantum Electronics and Laser Science Conference*. IEEE. 2006, pp. 1–2.

[177] Jerry R Meyer, William W Bewley, Chadwick L Canedy, Chul Soo Kim, Mijin Kim, Charles D Merritt, and Igor Vurgaftman. "The interband cascade laser". In: *Photonics*. Vol. 7. MDPI. 2020, p. 75.

[178] Lizhu Zhang, Guang Tian, Jingsong Li, and Benli Yu. "Applications of absorption spectroscopy using quantum cascade lasers". In: *Applied spectroscopy* 68.10 (2014), pp. 1095–1107.

[179] Frank K Tittel, Yury Bakhirkin, Anatoliy A Kosterev, and Gerard WYSOCKI. "Recent advances in trace gas detection using quantum and interband cascade lasers". In: *The Review of Laser Engineering* 34.4 (2006), pp. 275–282.

[180] A Maekawa, Y Shiomi, M Uchida, and T Kakuno. "QCL-based trace gas analyzer for industrial and healthcare applications". In: *Quantum Sensing and Nano Electronics and Photonics XIV*. Vol. 10111. SPIE. 2017, pp. 18–23.

[181] Igor Vurgaftman, R Weih, M Kamp, JR Meyer, CL Canedy, CS Kim, M Kim, WW Bewley, CD Merritt, J Abell, and S Höfling. "Interband cascade lasers". In: *Journal of Physics D: Applied Physics* 48.12 (2015), p. 123001.

[182] Yongquan Zeng, Bo Qiang, and Qi Jie Wang. "Photonic engineering technology for the development of terahertz quantum cascade lasers". In: *Advanced Optical Materials* 8.3 (2020), p. 1900573.

[183] Marilena Giglio, Pietro Patimisco, Angelo Sampaolo, Jason M Kriesel, Frank K Tittel, and Vincenzo Spagnolo. "Low-loss and single-mode tapered hollow-core waveguides optically coupled with interband and quantum cascade lasers". In: *Optical Engineering* 57.1 (2017), p. 011004.

[184] M Siciliani de Cumis, S Viciani, S Borri, P Patimisco, A Sampaolo, G Scamarcio, P De Natale, F D'Amato, and V Spagnolo. "Widely-tunable mid-infrared fiber-coupled quartz-enhanced photoacoustic sensor for environmental monitoring". In: *Optics Express* 22.23 (2014), pp. 28222–28231.

[185] Justin Cook, Felix A Tan, Ahmed Al Halawany, Alex Sincore, Lawrence Shah, Ayman F Abouraddy, Martin Richardson, and Kenneth L Schepler. "Efficient coupling of a quantum cascade laser to a few-mode chalcogenide fiber". In: *Optics Express* 27.20 (2019), pp. 27682–27690.

[186] Jean-Luc Adam. "Optical properties and applications of non-oxide glasses". In: *Metals and Materials Processing in a Clean Environment* 19 (2019).

[187] Shengqiang Lu, Fan Zhang, Cong Xu, and Ji'an Duan. "Coupling efficiency of a laser diode to a single-mode fiber via a microlens on the fiber tip". In: *Optical Fiber Technology* 68 (2022), p. 102766.

[188] Rawaa Al-Mahrous, Reinhard Caspary, and Wolfgang Kowalsky. "A thermal splicing method to join silica and fluoride fibers". In: *Journal of lightwave technology* 32.2 (2013), pp. 303–308.

[189] Rochdi El Abdi, A Rujinski, and M Poulain. "Mechanical characterization of fluoride optical fibers". In: *Journal of Basic and Applied Research International* 15.2 (2016), p. 106.

[190] *Nanoplus Interband Cascade Laser*. `https://nanoplus.com/products/interband-cascade-laser`.

[191] Koji Sugioka. "Progress in ultrafast laser processing and future prospects". In: *Nanophotonics* 6.2 (2017), pp. 393–413.

[192] Andri Abdurrochman, Sylvain Lecler, Frédéric Mermet, Bernard Y Tumbelaka, Bruno Serio, and Joël Fontaine. "Photonic jet breakthrough for direct laser microetching using nanosecond near-infrared laser". In: *Applied optics* 53.31 (2014), pp. 7202–7207.

[193] D Grojo, L Charmasson, A Pereira, M Sentis, and Ph Delaporte. "Monitoring photonic nanojets from microsphere arrays by femtosecond laser ablation of thin films". In: *Journal of Nanoscience and Nanotechnology* 11.10 (2011), pp. 9129–9135.

[194] C Constantinescu, LND Kallepalli, P Delaporte, O Utéza, and D Grojo. "Laser processing of metal thin films using transparent microsphere arrays". In: *Applied Surface Science* 336 (2015), pp. 112–117.

[195] Yangdong Wen, Feifei Wang, Haibo Yu, Pan Li, Lianqing Liu, and Wen Jung Li. "Laser-nanomachining by microsphere induced photonic nanojet". In: *Sensors and Actuators A: Physical* 258 (2017), pp. 115–122.

[196] Djamila Bouaziz, Grégoire Chabrol, Assia Guessoum, Nacer-Eddine Demagh, and Sylvain Lecler. "Photonic Jet-Shaped Optical Fiber Tips versus Lensed Fibers". In: *Photonics*. Vol. 8. 9. Multidisciplinary Digital Publishing Institute. 2021, p. 373.

[197] Maha M Khayyat. "Silica Microspheres for Economical Advanced Solar Applications". In: *Crystals* 11.11 (2021), p. 1409.

[198] Ronan Le Harzic, Nicolas Huot, Eric Audouard, Christian Jonin, Pierre Laporte, Stéphane Valette, A Fraczkiewicz, and Roland Fortunier. "Comparison of heat-affected zones due to nanosecond and femtosecond laser pulses using transmission electronic microscopy". In: *Applied Physics Letters* 80.21 (2002), pp. 3886–3888.

[199] Alex CM Kuo. "Poly (dimethylsiloxane)". In: *Polymer data handbook* 2 (1999).

[200] WM Goubau and RA Tait. "Short-time-scale measurement of the low-temperature specific heat of polymethyl methacrylate and fused silica". In: *Physical Review Letters* 34.19 (1975), p. 1220.

[201] Bartlomiej Graczykowski, A El Sachat, Juan Sebastián Reparaz, Marianna Sledzinska, Markus R Wagner, Emigdio Chavez-Angel, Y Wu, Sebastian Volz, Y Wu, F Alzina, and Torres C.M. Sotomayor. "Thermal conductivity and air-mediated losses in periodic porous silicon membranes at high temperatures". In: *Nature communications* 8.1 (2017), p. 415.

[202] Donald F Swinehart. "The beer-lambert law". In: *Journal of chemical education* 39.7 (1962), p. 333.

[203] Miao Liu, Jianren Sun, and Quanfang Chen. "Influences of heating temperature on mechanical properties of polydimethylsiloxane". In: *Sensors and Actuators A: Physical* 151.1 (2009), pp. 42–45.

[204] Huan Huang and Zhixiong Guo. "Ultra-short pulsed laser PDMS thin-layer separation and micro-fabrication". In: *Journal of Micromechanics and Microengineering* 19.5 (2009), p. 055007.

[205] Salvatore Amoruso, Giovanni Ausanio, Riccardo Bruzzese, M Vitiello, and X Wang. "Femtosecond laser pulse irradiation of solid targets as a general route to nanoparticle formation in a vacuum". In: *Physical Review B* 71.3 (2005), p. 033406.

[206] Robin Pierron, Sylvain Lecler, Julien Zelgowski, Pierre Pfeiffer, Frédéric Mermet, and Joël Fontaine. "Etching of semiconductors and metals by the photonic jet with shaped optical fiber tips". In: *Applied Surface Science* 418 (2017), pp. 452–455.

[207] Wu Yuan, Robert Brown, Wayne Mitzner, Lonny Yarmus, and Xingde Li. "Super-achromatic monolithic microprobe for ultrahigh-resolution endoscopic optical coherence tomography at 800 nm". In: *Nature communications* 8.1 (2017), p. 1531.

[208] Shuo Han, Marinko V Sarunic, Jigang Wu, Mark Humayun, and Changhuei Yang. "Handheld forward-imaging needle endoscope for ophthalmic optical coherence tomography inspection". In: *Journal of biomedical optics* 13.2 (2008), pp. 020505–020505.

[209] Jaewook Shin, Dung N Tran, Jasper R Stroud, Sang Chin, Trac D Tran, and Mark A Foster. "A minimally invasive lens-free computational microendoscope". In: *Science advances* 5.12 (2019), eaaw5595.

[210] Ermanno Miele, Wesley M Dose, Ilya Manyakin, Michael H Frosz, Zachary Ruff, Michael FL De Volder, Clare P Grey, Jeremy J Baumberg, and Tijmen G Euser. "Hollow-core optical fibre sensors for operando Raman spectroscopy investigation of Li-ion battery liquid electrolytes". In: *Nature Communications* 13.1 (2022), p. 1651.

Publications and Communication

- Hajj T., Marbach S., Pfeiffer P., Montgomery P., Lecler S, et Flury M "High-quality manipulable fiber-microsphere for super-resolution microscopy" Opt. Lett. 48, 2222-2225 (2023)
- Bouaziz D, Perrin S, Hajj T, Chabrol G, Guessoum A, Demagh NE, Lecler S. "Direct imaging of a photonic jet at shaped fiber tips" Optics Letters. 2021 Oct 15;46(20):5125-8.
- Assia Guessoum, Tony Hajj, Djamila Bouaziz, Gregoire Chabrol, Pierre Pfiffer, Nacer-E. Demagh et Sylvain Lecler "Molded high curvature core-aligned micro-lenses for single-mode fibers" Applied optics 61.26 (2022): 7741-7747.

Three articles are in the works and are expected to be published in the near future:

- Micro-lens for ICL-fiber coupling enhancement
- MCF polymer micro-lens array
- Polymer micro-lens fluence toleracne and their implementation in laser processing applications

National and international conferences:

- "Highly focused photonic nanojet by molded high curvature fiber micro-lenses" Hajj T, Guessoum A, Chabrol G, Demagh NE, Lecler S, 2023 Conference on Lasers and Electro-Optics/Europe - European Quantum Electronics Virtual Conferences (CLEO®/Europe-EQEC 2023), 26 - 30 juin 2023, Munich, Allemagne.
- "High curvature fiber micro-lens" Hajj T, Bouaziz D, Chabrol G, Guessoum A, Demagh NE, Lecler S, Conférence internationale SPIE Photonics Europe, 3-7 avril 2022 (Strasbourg) + Village de l'innovation (2ème place).
- "High power polymer micro-lens tolerance for surface sub-micron marking" T. Hajj, D. Bouaziz, A. Guessoum, G. Chabrol, N. Demagh, L. Sylvain, EMRS 2022 - Recherche fondamentale et applicative sur les interactions laser-matière : 1er juin (conférence numérique).
- "Fibre à lentille polymère pour la gravure sub-micron de surface par laser haute puissance" T. Hajj, D. Bouaziz, G. Chabrol, N-E. Demagh, S. Lecler, Procédés Laser pour l'Industrie, Saint-Étienne, 28-29 juin 2022.

- "Tailored optical fiber tips photonic nano-jet characterization" D. Bouaziz, S. Perrin, T. Hajj, G. Chabrol, A. Guessoum, N-E. Demagh, S. Lecler, Photonics Europe 3-7 avril 2022 – Strasbourg.
- "Shape-controlled microlenses for light emerging from optical fibers" T. Hajj, D. Bouaziz, A. Guessoum, G. Chabrol, N-E. Demagh, S.Lecler, PIERS 21, Photonet Sino-French optoelectronic forum, novembre 2021 (Hangzhou, conférence numérique)

UNIVERSITE DE STRASBOURG

ECOLE DOCTORALE MATHEMATIQUES SCIENCES DE L'INFORMATION ET DE L'INGENIEUR

RESUME DE LA THESE DE DOCTORAT

Discipline : Optique et Photonique

Spécialité (facultative) : Fibre Optique

Présentée par :
Tony HAJJ

Titre :
High curvature micro-lenses for advance optical fibers
Micro-lentilles à forte courbure pour fibres optiques avancées

Unité de Recherche :
ICube

Directeur de Thèse :
Lecler Sylvain - Professeur

Co-encadrant de Thèse:
Charbrol Grégoire – Docteur (HDR)

Localisation :
Télécom Physique Strasbourg, Pôle API
300, Boulevard Sébastien Brant, 67412 Illkirch

Thèse confidentielle : ☒ NON ☐ OUI

De nombreuses techniques existent déjà pour lentiller des fibres. Ces techniques permettent cependant un éventail limité de formes de lentilles. La plupart échouent à obtenir des interfaces à courbure élevée pourtant nécessaire générer des faisceaux hautement focalisés avec une largeur à mi-hauteur proche de λ. Ces techniques ne sont souvent utilisables que sur les fibres silice pleine. Cette thèse de doctorat porte sur la fabrication de microlentilles à forte courbure pour cœur de fibres optiques monomodes afin d'obtenir une focalisation à l'échelle du micron ou de faciliter la collection de la lumière.

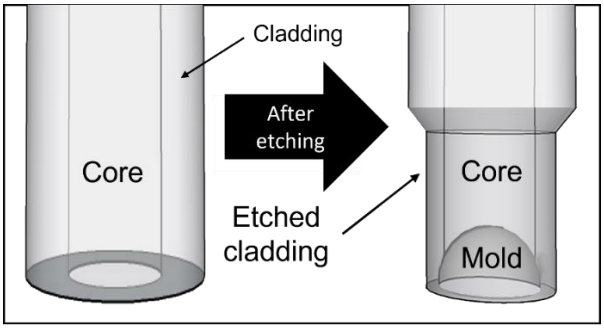

Fig.1 Schéma de principe de la formation du moule par gravure chimique.

Notre groupe, en collaboration avec l'Université de Sétif, a développé une nouvelle technique de fabrication de microlentilles qui permet de contrôler leur forme, leur taille et d'obtenir des courbures élevées. De plus, comme cela sera présenté, la technique de fabrication est compatible avec une large gamme de fibres optiques.

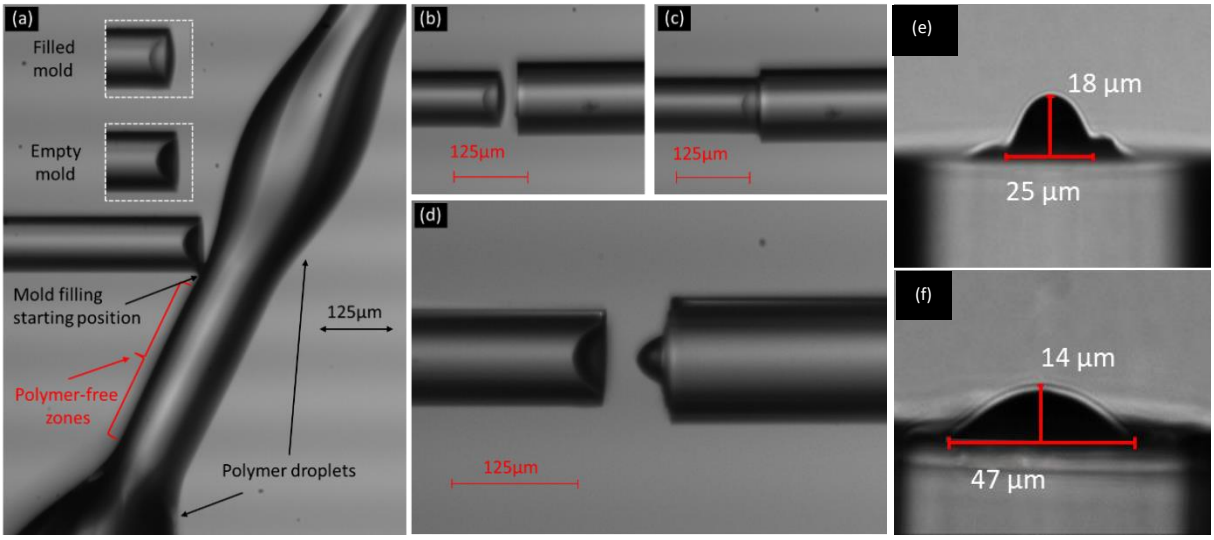

Fig.2 (a) Remplissage du moule avec du polymère, (b) et (c) alignement de la fibre et du moule, (d) libération du moule après précuisson. (e) Microlentille à courbure élevée sur une fibre monomode (SMF28). (f) Microlentille à courbure faible sur SMF28.

Pour cette technique que nous avons brevetée, il est est nécesaire de d'abord créer un moule de la lentille à l'intérieur d'une fibre optique à indice à gradient d'indice. Pour cela, la fibre est plongée dans une solution d'acide fluorhydrique (HF), pendant un temps fonction de la hauteur de lentille souhaitée. La fibre est ensuite retirée et rincée. Une représentation du principe de gravure et la formation du moule est montrée figure 1. La forme de la lentille peut être contrôlée en variant les temps de gravure, le diamètre du cœur de fibre et le gradient de dopage au germanium. Ensuite, le moule est rempli d'un polymère (PDMS, NOA...), suivi d'un alignement optique avec la fibre sur laquelle la lentille doit être déposée. Enfin, le polymère est pré-polymérisé soit par montée en température, soit par lumière UV, fonction du polymère utilisé, puis le moule est retiré. La procédure de fabrication est représentée figure 2.

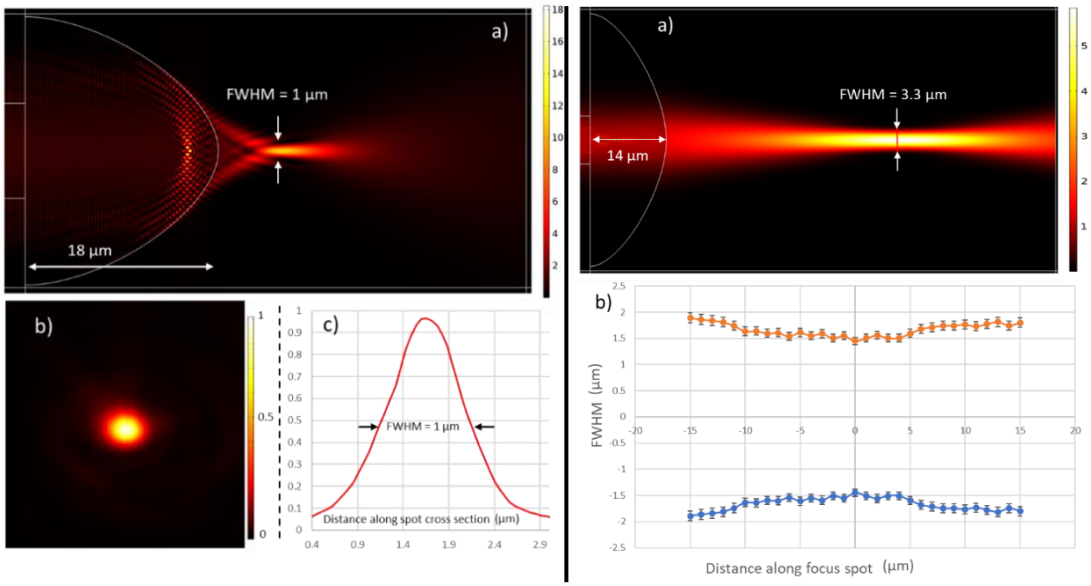

Fig.3 Caractérisation numérique (figures du haut) et expérimentale (figures du bas) des deux fibres lentillées de la figure 2 (e) et (f). Les figures de gauche montrent un faisceau fortement focalisé en raison du rayon de courbure élevé de la microlentille montrée dans la figure 2 (e), et les figures de droite montrent une collimation du faisceau sur une distance de 30 µm en raison du rayon de courbure inférieur de la microlentille montrée dans la figure 2 (f).

Pour mettre en perspective l'effet de la courbure de la microlentille sur le faisceau généré, les faisceaux issus des deux fibres microlentillées de la figure 2 (e et f) ont été caractérisées et leurs résultats représentés à la figure 3 (figures du bas). Cela montre que les microlentilles à courbure plus élevée conduisent à des faisceaux fortement focalisés, tandis que les courbures faibles conduisent à une collimation du faisceau et à une profondeur de champ plus grande au détriment d'un diamètre de faisceau plus grand.

Les simulations numériques ont également été réalisées par méthode éléments finis à l'aide du module optique du logiciel COMSOL Multiphysics, et les résultats sont représentés à la figure 3 (deux premières figures du haut).

Nous avons démontré expérimentalement que notre technique est compatible avec les fibres optiques fluorées à ondes moyennes infrarouges (MIR) comme indiqué à la figure 4 (a) et (b). Les fibres optiques MIR sont fabriquées à partir de verres à base de fluorure, d'halogénure ou de chalcogénure, car la transmittance des fibres à base de silice devient extrêmement faible dans cette plage de longueurs d'onde. Cependant, ces fibres MIR sont très fragiles et ont des propriétés très différentes de celles à base de silice, rendant presque impossible le processus de fabrication de microlentilles pour elles avec les techniques actuellement disponibles sur le marché. C'est pourquoi notre technique est très prometteuse pour de nombreuses applications MIR impliquant des fibres optiques. Par exemple, nous avons pu doubler l'efficacité de couplage de la lumière générée par des lasers à diode MIR dans des fibres monomodes et multimodes MIR.

De plus, au cours de cette thèse, la technique de fabrication développée a été adaptée aux fibres multicœurs (MCF). Pour cela, de nombreux défis ont dû être surmontés, tels que l'alignement parfait des cœurs, la résolution du problème de formation de bulles d'air lors de l'étape de remplissage du moule et le contrôle des courbures des microlentilles. Les réseaux de microlentilles fabriquées sont présentés à la figure 4 (c - e).

De plus, nous avons également démontré que notre technique est compatible avec les fibres à cristaux photoniques à cœur creux, comme le montre la figure 4 (f). La fibre a un diamètre de cœur de 15 µm, et sa structure interne est montrée à la figure 4 (g).

Enfin, le seuil de tolérance de puissance pour les microlentilles créées (4 watts de puissance moyenne provenant d'un laser pulsé de 100 ns à 35 kHz émettant à 1070 nm) a été déterminé

expérimentalement et étudié numériquement et s'est révélé être plusieurs ordres de grandeur plus élevé que ce qui est nécessaire pour réaliser de la microgravure du silicium (quelques dizaines de microwatts suffisant en raiosn de la forte foclaisation), prouvant que les microlentilles peuvent effectivement être utilisées pour des applications de traitement en surface au laser des matériaux.

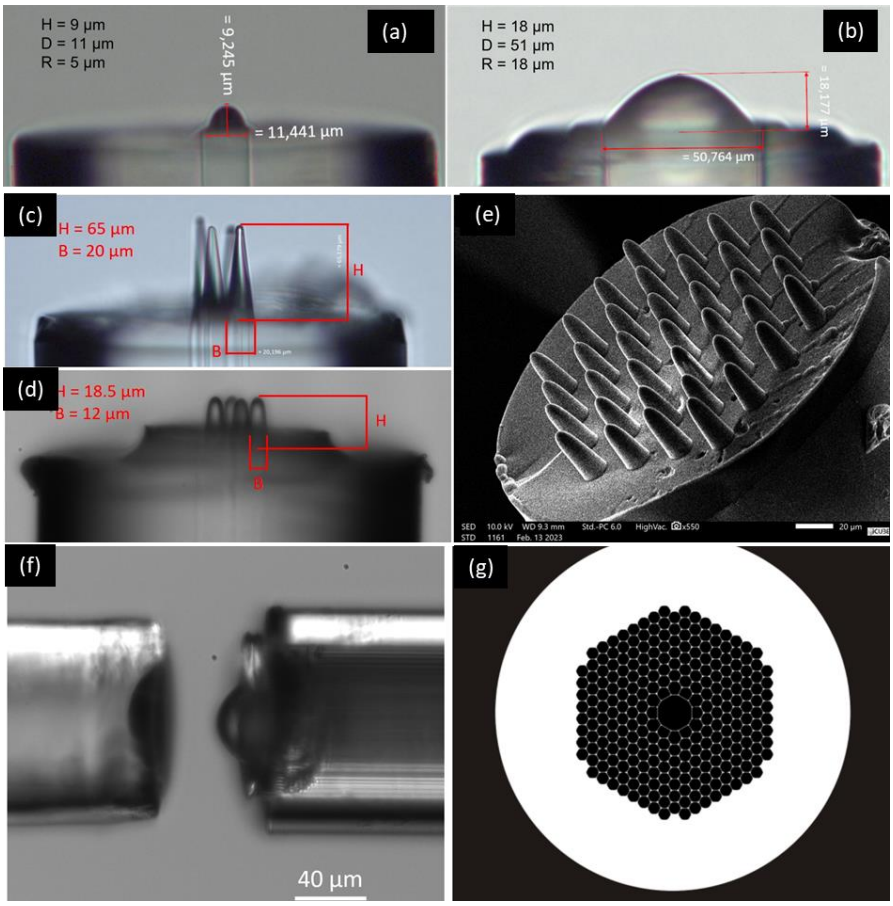

Fig.4 Configuration améliorée de fabrication de micrlentilles adaptée aux fibres (a,b) fluorées, multicœurs avec (c,d) 4 cœurs, (e) 37 cœurs et (f,g) à cœur creux.

En résumé la thèse a permis de montrer que la technique de fabrication par moulage développée en coopération avec l'Université de Sétif permet de réaliser relativement simplement, à faible coût une large variété de microlentilles plano-convexes dont la forme peut être contrôlée, jusqu'à de très faibles rayons de courbe (5-10 µm) et ce sur une large gamme de fibres optiques, silice, fluorée, multicœurs, micro-structurées, à cœur creux, etc. Cela en fait une technique prometteuse pour de nombreuses applications.

Contributions scientifiques :

Article en revues internationales

- **Hajj T**., Marbach S., Pfeiffer P., Montgomery P., Lecler S, et Flury M "High-quality manipulable fiber-microsphere for super-resolution microscopy," Opt. Lett. 48, 2222-2225 (2023)
- Guessoum A, **Hajj T**, Bouaziz D, Chabrol G, Pfeiffer P, Demagh NE, Lecler S, "Molded high curvature core-aligned micro-lenses for single-mode fibers" Appl. Opt. 61(26), pp. 7741-7747, (2022).
- https://doi.org/10.1364/AO.462961 Bouaziz D, Perrin S, **Hajj T**, Chabrol G, Guessoum A, Demagh NE, Lecler S. "Direct imaging of a photonic jet at shaped fiber tips". Optics Letters. 46(20):5125-8 (2021).

Trois autres articles sont prévus sur : (1) les micro-lentilles pour fibres MIR (2) les réseaux de micro-lentilles pour les fibres multicœurs et (3) la tolérance de puissance des micro-lentilles en polymère et leur mise en œuvre dans des applications de traitement au laser.

Conférences nationales et internationales :

- "Highly focused photonic nanojet by molded high curvature fiber micro-lenses" **Hajj T**, Guessoum A, Chabrol G, Demagh NE, Lecler S, 2023 Conference on Lasers and Electro-Optics/Europe - European Quantum Electronics Virtual Conferences (CLEO®/Europe-EQEC 2023), 26 - 30 juin 2023, Munich, Allemagne.
- "High curvature fiber micro-lens" **Hajj T**, Bouaziz D, Chabrol G, Guessoum A, Demagh NE, Lecler S, Conférence internationale SPIE Photonics Europe, 3-7 avril 2022 (Strasbourg) + Village de l'innovation (2ème place).
- "High power polymer micro-lens tolerance for surface submicron marking" **T. Hajj**, D. Bouaziz, A. Guessoum, G. Chabrol, N. Demagh, L. Sylvain, EMRS 2022 - Recherche fondamentale et applicative sur les interactions laser-matière : 1er juin (conférence numérique).
- "Fibre à lentille polymère pour la gravure sub-micron de surface par laser haute puissance" **T. Hajj**, D. Bouaziz, G. Chabrol, N-E. Demagh, S. Lecler, Procédés Laser pour l'Industrie, Saint-Étienne, 28-29 juin 2022.
- "Tailored optical fiber tips photonic nano-jet characterization" D. Bouaziz, S. Perrin, **T. Hajj**, G. Chabrol, A. Guessoum, N-E. Demagh, S. Lecler, Photonics Europe 3-7 avril 2022 – Strasbourg.
- "Shape-controlled microlenses for light emerging from optical fibers" **T. Hajj**, D. Bouaziz, A. Guessoum, G. Chabrol, N-E. Demagh, S.Lecler, PIERS 21, Photonet Sino-French optoelectronic forum, novembre 2021 (Hangzhou, conférence numérique).

Tony HAJJ

High curvature micro-lenses for advanced optical fiber applications

Résumé

Notre technique de fabrication de microlentilles en embout de fibres à base de polymères moulés, récemment introduite, a fait l'objet de recherches plus approfondies et a été développée dans le cadre de cette thèse. Les microlentilles présentent une haute qualité, une durabilité et une flexibilité de conception avancée, avec des courbures allant jusqu'à 10 µm. En utilisant des simulations COMSOL et des validations expérimentales, nous analysons les performances des lentilles et les pertes de lumière en fonction de leurs conceptions. Nous démontrons que les microlentilles à haute courbure génèrent des faisceaux hautement focalisés avec une FWHM ≤ λ. En outre, nous démontrons la compatibilité de cette technique avec des fibres optiques non traditionnelles, telles que les fibres fluorurée, les fibres multicœurs et les fibres à cœur creux. Nous avons réussi à réaliser des réseaux de microlentilles pour des fibres à 4 et 37 cœurs. Les applications de ce projet comprennent l'amélioration du couplage lumineux des lasers à cascade interbandes avec des fluorurée, que nous avons réussi à doubler, et la possibilité de graver le silicium à haute résolution. Pour cette dernière application, nous avons étudié la tolérance en puissance des microlentilles et avons constaté qu'elles supportaient ≥ 2 W (57 µJ), ce qui est significativement plus élevé que ce qui est nécessaire pour la gravure du silicium avec des faisceaux hautement focalisé (FWHM ≤ 5 µm).

Mots-clés : Micro lentilles en embout de fibres, Haute courbure, Fibres fluorurée, Fibres creuses, Fibres multi-cœurs, COMSOL multiphysics, Tolérance à la puissance, Gravure de silicium, lasers à cascade interbandes.

Abstract

Our recently introduced molded polymer-based fiber micro-lens fabrication technique was further researched and developed in this thesis. The micro-lenses exhibit high-quality, durability, and advanced design flexibility, with curvatures as high as 10 µm. Using COMSOL multiphysics simulations and experimental validation, we analyze lens performance and light losses with respect to the lens design. We demonstrate that high-curvature micro-lenses generate highly focused beams with a FWHM of ≤ λ. Moreover, we show the compatibility of this technique with non-traditional optical fibers, such as fluoride-based, multi-core, and hollow-core fibers. We successfully achieved micro-lens arrays for 4-core and 37-core fibers. The applications of this project consist of improving the light coupling efficiency of interband cascade lasers with fluoride fibers, which we were able to double, and enabling high-resolution silicon etching. For the latter, we investigated the power tolerance of micro-lenses and found it to be ≥ 2 W (57 µJ), significantly higher than what is required for silicon etching with highly focused beams (FWHM ≤ 5 µm).

Keywords: Fiber micro-lenses, High-curvature, Fluoride-based fibers, Hollow-core fibers, Multi-core fibers, COMSOL multiphysics, Power tolerance, Silicon etching, interband cascade laser.